

1 **Crustal and uppermost mantle structure beneath the United States**

2 Weisen Shen and Michael H. Ritzwoller

3 Department of Physics, University of Colorado at Boulder, Boulder, CO 80309 USA

4 (weisen.shen@colorado.edu)

5 **Abstract**

6 This paper presents a new model of the shear velocity structure of the crust and uppermost
7 mantle beneath the contiguous US. The model is based on more than a decade of USArray
8 Transportable Array (TA) data across the US and derives from a joint Bayesian Monte Carlo
9 inversion of Rayleigh wave group and phase speeds determined from ambient noise and
10 earthquakes, receiver functions, and Rayleigh wave ellipticity (H/V) measurements. Within the
11 Bayesian inverse theoretic framework, a prior distribution of models is posited and a posterior
12 distribution is inferred beneath all of the more than 1800 TA stations across the US. The
13 resulting mean and standard deviation of the mean of the posterior distribution at each station
14 summarize the inversion results, which are then interpolated onto a regular $0.25^\circ \times 0.25^\circ$ grid
15 across the US to define the final 3D model. We present arguments to show that the mean of the
16 posterior distribution overestimates the effect of random error in the final model by a factor of 4-
17 5, and identify uncertainties in density and mantle Q as primary potential sources of remaining
18 systematic error in the final model. The model presents a great many newly resolved structural
19 features across the US that require further analysis and dedicated explication. We highlight here
20 low velocity anomalies in the upper mantle that underlie the Appalachians with centers of
21 anomalies in northern Georgia, western Virginia, and, most prominently, New England.

22 1. Introduction

23 The USArray/Transportable Array (TA), one of the principal components of EarthScope, has
24 been evolving for more than the past 10 years. Since 2004, the TA has repeatedly deployed
25 approximately 400 three-component broadband seismometers at temporary sites with an inter-
26 station spacing of about 70 km. The array has crept continuously across the US to occupy sites
27 that have eventually spanned the continent, completing its earthward migration in the fall of
28 2013. Nearly 2000 independent locations were occupied during the migration of the array. This
29 seismic observatory has stimulated many innovations in seismology designed to improve the
30 understanding of earth structure and processes beneath the contiguous United States. In
31 particular, crustal imaging at continental scales has been revolutionized in response to the
32 existence of data from this array.

33 The current paper is based on TA data. Methodologically, this paper is part of a series of
34 research efforts that have attempted to model crustal and uppermost mantle structure beneath the
35 contiguous US using newly developed methods of data analysis, inversion, and inference
36 designed for application to current generation continental array data, of which the TA is a prime
37 example. There have been two principal themes that have guided these efforts: (1) the tracking of
38 uncertainty from measured quantities to resulting 3D models and (2) assimilating new data types
39 and resources into the inversion as they become available. With the completion of the TA in
40 2013, models of the crust and uppermost mantle can now be constructed across the entire US.

41 These research efforts have been composed of five principal components on which the current
42 paper builds and of which it is a natural continuation. First, in order to constrain crustal structure,
43 ambient noise surface wave tomography was developed and has been applied to data beginning
44 from the earliest days of operation of the TA (e.g., [Sabra et al., 2005](#); [Shapiro et al., 2005](#);
45 [Bensen et al., 2007](#); [Lin et al., 2008](#)). Ambient noise tomography has become a standard method
46 in crustal imaging, and has provided unprecedented information about crustal structure across the
47 US (e.g., [Moschetti et al. 2007, 2010a,b](#); [Yang et al., 2008, 2011](#); [Bensen et al., 2009](#); [Lin et al.,](#)
48 [2011](#); [Tian et al., 2013](#); [Xie et al., 2015](#)). The eikonal tomography method was developed to
49 optimize information derived from ambient noise tomography ([Lin et al., 2009](#)). Second, to
50 generate higher resolution information from surface waves about upper mantle structure, the
51 Helmholtz tomography method was developed for application to data from earthquakes ([Lin and](#)

52 Ritzwoller, 2011; Ritzwoller et al., 2011; Mordret et al, 2013; Jin and Gaherty, 2015) similar to
53 the method of Pollitz and Snoko (2010). Eikonal tomography is a geometrical ray theoretic
54 method and Helmholtz tomography is a finite frequency method; finite frequency corrections are
55 needed at the longer periods at which earthquake generated surface waves are observed. Third,
56 both eikonal and Helmholtz tomography provide information about azimuthal anisotropy and
57 (importantly) local uncertainty estimates of the resulting tomographic maps. Fourth, surface
58 wave data alone typically do not unambiguously constrain vertically discontinuous variations in
59 model variables such as may occur at the base of sedimentary basins or at the Moho. Lebedev et
60 al. (2013) present a recent assessment of the problem. It has long been known that the
61 assimilation of other types of data in addition to surface wave dispersion helps to resolve
62 ambiguities that arise in the estimation of crustal and uppermost mantle structure, particularly
63 related to crustal thickness, structure near to the Moho, and near-surface structure (e.g., Last et
64 al., 1997; Ozalaybey et al., 1997; Julia et al., 2000). There are numerous examples of the joint
65 inversion of surface wave data and receiver functions (e.g., Chang et al., 2004; Lawrence and
66 Wiens, 2004; Liu et al., 2010; Tokam et al., 2010; Bodin et al., 2012). We (and others) have
67 developed methods to assimilate other types of data and invert them systematically and jointly
68 along with surface wave dispersion using uncertainty information, including receiver functions
69 (Shen et al., 2013a,b,c), local amplification measurements (Taylor et al., 2009; Lin et al., 2012a;
70 Eddy and Ekstrom, 2014), Rayleigh wave ellipticity (or H/V) measurements (Lin et al., 2012b;
71 Lin and Schmandt, 2014; Lin et al., 2014), and body waves (Obrebski et al., 2011; Porritt et al.,
72 2014). Fifth, Bayesian Monte Carlo inversion methods have been developed (e.g., Shen et al.,
73 2013a,b,c) to invert jointly new high-resolution surface wave dispersion information together
74 with other data types in order to produce distributions of models that fit all data acceptably. The
75 resulting posterior distributions of models are then summarized to produce the 3D model
76 together with uncertainties.

77 The TA has stimulated a variety of approaches to inferring information about crustal and mantle
78 structure beneath the US. For example, the current paper is one of many based at least in part on
79 ambient noise observations across the US: e.g., Liang and Langston (2008, 2009), Prieto and
80 Beroza (2008), Ma et al. (2008), Gao et al. (2011), Calkins et al., (2011) Porritt et al. (2011),
81 Delorey et al. (2011), Gaito et al. (2012), Liu et al. (2012), Tibuleac et al. (2012), Gao and Shen
82 (2012), Hansen et al. (2013), Allison et al., (2013), Kao et al. (2013), Boue et al. (2014), Li and

83 Lin (2014), Porter et al., (2014, 2015), Yang (2014), Ekstrom (2014), Schmandt and Lin (2014),
84 Fu and Li (2015), Zigone et al. (2015), Agrawal et al. (2015), and others. The measurement of
85 Rayleigh wave ellipticity (or H/V measurements) using earthquake data goes back to Boore and
86 Toksoz (1969) and has been recently rejuvenated by Tanimoto and Rivera (2008) and Lin et al.
87 (2012b). Lin et al. (2014) extended the H/V measurements to ambient noise and Lin and
88 Schmant (2014) also extended them to azimuthal anisotropy. Lin et al. (2012b) performed a joint
89 inversion of H/V measurements along with surface wave dispersion for crustal and uppermost
90 mantle structure. In addition, there have been many studies of both P-to-S and S-to-P receiver
91 functions across the US based at least in part on USArray data: e.g., Agrawal et al., 2015; Benoit
92 et al., 2014; Calkins et al., 2010; Eagar et al., 2011; Frassetto et al., 2011; Gao, 2015;
93 Gashawbeza et al., 2008; Gilbert, 2012; Hansen and Deuker, 2009; Hansen et al., 2013; Hopper
94 et al., 2014; Levander and Miller, 2012; Levander et al., 2011; Parker et al., 2013; Porter et al.,
95 2014; Stacknik et al., 2008; Thurner et al., 2015; Wagner et al., 2012; Wilson et al., 2010; Yeck
96 et al., 2014.

97 The joint inversion of surface wave dispersion, receiver functions, and Rayleigh wave H/V
98 measurements remains rare. To the best of our knowledge using USArray data the joint inversion
99 of surface wave dispersion together with receiver functions in the US has been carried out
100 regionally only by Bailey et al. (2012) and Shen et al. (2013a,b,c) and the joint inversion of
101 surface wave dispersion together with H/V measurements by Lin et al. (2012b). The joint
102 inversion of all three data sets has not been performed before in the US, but has been
103 accomplished in a regional study in China (Kang et al., 2015). The current paper is a natural
104 continuation of the studies of Shen et al. (2013a,b,c), which developed and applied Bayesian
105 Monte Carlo inversion methods to the joint inversion of Rayleigh wave dispersion from ambient
106 noise and earthquake data and receiver function data across the western half of the US. The
107 current paper modifies and extends this earlier work by introducing a new data set of Rayleigh
108 wave H/V measurements across the entire US and inverting all data simultaneously (Rayleigh
109 wave dispersion from 8-90 sec period, receiver functions, Rayleigh wave H/V measurements
110 from 18-80 sec period) to estimate a unified crustal and uppermost mantle model across the
111 entire contiguous US with attendant uncertainties. More than five years of TA data are added and
112 the region of study extends about 3,000 km farther east compared to the earlier studies of Shen et
113 al. (2013b). In total we obtain observations using ~1,800 TA stations deployed before 2015 June

114 (Fig. 1) and invert all data within a Bayesian Monte Carlo framework. Significantly, consistent
115 with the findings of Shen et al. (2013a,b) the introduction of receiver functions into the inversion
116 significantly improves determination of Moho depth and structures near the crust-mantle
117 transition, and consistent with the findings of Lin et al. (2012b) the introduction of the H/V
118 measurements significantly improves estimates of structures in the top few km of the crust.
119 Overall, combining all three data sets improves the vertical resolution of the crust and uppermost
120 mantle, and the resulting 3-D Vs model reveals high fidelity features of the crust and uppermost
121 mantle across the entire US.

122 The discussion below begins with a description of the data set of Rayleigh wave dispersion
123 measurements, receiver functions and Rayleigh wave H/V measurements in section 2. Although
124 the full data set is new, the methods of measurement have been described elsewhere, and here we
125 only summarize the methods used to estimate the principal quantities and errors in them. The
126 joint Bayesian Monte Carlo inversion method also has been described elsewhere. Only salient
127 aspects of the method are summarized in section 3 where we focus attention on the description of
128 the assumptions and constraints that result in the prior distribution of models at each location.
129 The Bayesian Monte Carlo method jointly inverts all data, producing a posterior distribution of
130 models at each of more than 1750 stations across the US. In section 4 we discuss how we
131 summarize these distributions in terms of a mean and standard deviation at each depth in the
132 crust and uppermost mantle and location across the US and how the mean varies regionally and
133 within regions across the US. We discuss how the posterior distribution can be used to quantify
134 the effects of random errors in the model. In section 5, we present vertical transects of the model
135 and discuss systematic errors that may arise due to constraints and assumptions applied in the
136 inversion.

137 **2. Data: Measurement, Processing, and Uncertainty**

138 This study is based on data from the 1,822 USArray Transportable Array seismic stations that are
139 shown in Figure 1b. These stations are fairly homogeneously distributed across the US, being
140 spaced on average about every 70 km. Based on data from these stations, we produce 1)
141 Rayleigh wave dispersion maps and local dispersion curves from ambient noise and earthquake
142 data, 2) azimuthally-independent receiver functions, and 3) Rayleigh wave ellipticity
143 measurements, also referred to as H/V measurements (e.g., Lin et al., 2012b). We construct

144 Rayleigh wave phase speed curves from 8 to 90 sec period beneath each station from dispersion
145 maps produced by eikonal tomography (Lin et al., 2009) for ambient noise data and Helmholtz
146 tomography (Lin and Ritzwoller et al., 2011) for teleseismic earthquake data. We generate
147 Rayleigh wave group velocity curves by traditional ray theoretic tomography (Barmin et al.,
148 2001; Moschetti et al., 2010a) between periods of 8 sec and 40 sec. In addition, we construct a
149 back-azimuth independent receiver function using the harmonic stripping technique (Shen et al.,
150 2013a) at each station. The details of the data processing and subsequent data quality control and
151 refinement have been documented in a number of previous papers, and we only briefly
152 summarize the data processing here.

153 **2.1. Rayleigh wave phase velocities**

154 We obtained Rayleigh wave phase speed measurements between periods of 8 and 40 sec on
155 ambient noise cross-correlations between data from USArray TA stations available from Jan
156 2005 until the end of June 2015 using automated frequency-time analysis (AFTAN) (e.g.,
157 Levshin and Ritzwoller, 2001; Bensen et al., 2007). The ambient noise data processing follows
158 the procedure described by Bensen et al. (2007) and Lin et al. (2008). More than 650,000 cross-
159 correlations across the study region are produced. At short periods (8 to 40 sec), we apply
160 eikonal tomography (Lin et al., 2009) to ambient noise data to generate Rayleigh wave phase
161 velocity maps with uncertainty estimates (e.g., Fig. 2c-d). At longer periods (28 to 80 sec) using
162 earthquake data, we apply the Helmholtz tomography method (Lin and Ritzwoller, 2011) to
163 obtain Rayleigh wave phase velocity measurements with uncertainties. Both eikonal and
164 Helmholtz tomography estimate local uncertainties in phase speed from the scatter in the local
165 azimuthally dependent phase times (and thus speeds) after smooth variations with azimuth are
166 removed. The standard deviation of the mean of the observed scatter is then identified with the
167 error in the local period dependent phase speed. Rayleigh wave phase travel times are measured
168 using waveform data following 5,898 earthquakes recorded between 2005 and 2015 with $M_s >$
169 5.5 and Helmholtz tomography is applied to produce the phase velocity maps. The Helmholtz
170 tomography method provides a finite frequency correction, which is needed at long periods, but
171 the eikonal tomography method (applied at shorter periods) does not. Sample maps are presented
172 in Figure 2e,f. In the period band in which ambient noise and earthquake measurements overlap
173 (28 to 40 sec), there is significant agreement between the maps. Several earlier studies found

174 that phase speed measurements inferred from earthquakes were somewhat faster than those from
175 ambient noise measurements (Yao et al., 2006, Yang et al., 2008). As we have added increasing
176 numbers of earthquake measurements, however, measurements from earthquakes have
177 converged to those from ambient noise (Lin and Ritzwoller, 2011; Ritzwoller et al, 2011) such
178 that now at 28 sec period, for example, the average difference across the US is about 1 m/s. The
179 standard deviation of the difference is about 12 m/s, which is within the estimated average
180 uncertainty (~15 m/sec). In both eikonal tomography applied to ambient noise data and
181 Helmholtz tomography applied to earthquake data, azimuthal anisotropy with 180° symmetry is
182 estimated simultaneously with azimuthally independent phase speeds. Thus, the effect of
183 azimuthal anisotropy has been removed from the isotropic phase speed measurements presented
184 here.

185 2.2 Rayleigh wave group velocities

186 Both phase and group velocity dispersion curves are measured when automated frequency-time
187 analysis (AFTAN) is applied to ambient noise cross-correlations. Although eikonal tomography
188 is performed on the phase time measurements from ambient noise, the eikonal equation governs
189 the propagation of phase but not group times. Thus, we use the traditional damped least-squares
190 tomographic method of Barmin et al. (2001) for group velocities. The traditional tomographic
191 method and eikonal tomography provide similar results, as shown by Lin et al. (2009) and Zhou
192 et al. (2012). We ignore finite frequency effects on group speeds here, because they are weak in
193 the period band in which ambient noise is considered (8-40 sec; e.g. Lin & Ritzwoller 2011;
194 Ritzwoller et al. 2011). Azimuthal anisotropy with 180° symmetry is estimated simultaneously
195 with azimuthally independent group speeds. Thus, as with phase speeds, the effect of azimuthal
196 anisotropy has been removed from the isotropic group speeds presented here.

197 The 8 and 28 sec period group velocity maps are presented in Figure 2a and 2b. At 8 sec period,
198 group velocity is most sensitive to shear wave speed in the top 10 km of the crust. Similar to the
199 8 sec phase velocity map, major basins exhibit slow group velocities (< 2.4 km/sec). At 28 sec
200 period, the group velocity map presents a slightly different pattern than the phase velocity map
201 because of the relatively shallower sensitivity of group velocities. Because a damped least-
202 squares inversion is used to generate the group velocity maps, meaningful uncertainties are not

203 obtained in the inversion although resolution is estimated. The uncertainty of group velocity is
204 scaled from the uncertainty of phase velocity using the relationship described by Moschetti et al.
205 (2012b). On average, group velocity uncertainty is magnified by a factor of about three
206 compared with phase velocity uncertainty. In this study, we use group velocity measurements
207 only when the horizontal resolution is better than 100 km; thus, group velocity measurements at
208 some periods are discarded near the edges of the study region. Finally, we obtain local dispersion
209 curves for 1,816 out of 1,822 USArray/TA stations and examples of local Rayleigh wave group
210 and phase velocity curves are presented in Figure 6.

211 2.3 Receiver functions

212 Shen et al. (2013b) describe the method that we apply to process receiver functions for each
213 station. For each station, we select earthquakes from Jan 2005 to June 2015 with epicentral
214 distances ranging between 30° and 90° and with magnitudes $m_b > 5.5$. We apply a time domain
215 deconvolution method (Ligorria and Ammon, 1999) to each seismogram windowed between 20
216 sec before and 30 sec after the direct P-wave arrival to compute the radial component receiver
217 function using a low-pass Gaussian filter with a width of 2.5 s (pulse width ~ 1 sec). High-
218 quality receiver functions are selected with an automated procedure. Corrections are made both
219 to the time and amplitude of each receiver function, normalizing to a reference slowness of 0.06
220 sec/km (Jones and Phinney, 1998). Finally, we retain only the first 10 sec after the direct P
221 arrival. We compute the azimuthally independent receiver function, $R_0(t)$, at each station by
222 fitting a truncated Fourier Series at each time over azimuth and then stripping the azimuthally
223 variable terms using a method referred to as “harmonic stripping” by Shen et al. (2013b). After
224 removing the azimuthally variable terms at each time, the RMS residual over azimuth is
225 interpreted as the 1σ uncertainty in $R_0(t)$ at that time. On average, 84 individual receiver
226 functions from different earthquakes are accumulated for each station. If fewer than 10 receiver
227 functions pass quality control at a particular station, we do not use the receiver function in the
228 joint inversion. In total, we obtain azimuthally independent receiver functions for 1822
229 USArray/TA stations. Example receiver functions are presented in Figure 6.

230

231

232 2.4 Rayleigh wave ellipticity (H/V)

233 As discussed in section 2.1, the data following more than 5,800 teleseismic earthquakes are
234 collected to perform teleseismic Helmholtz tomography across the contiguous US. This data set
235 is also used to measure the Rayleigh wave H/V ratio following the processing procedure
236 presented by [Lin et al. \(2012a\)](#), which we summarize briefly here.

237 For each earthquake recorded at each available station, 3-component seismograms are cut
238 according to the Rayleigh wave group travel time predicted by a global model ([Shapiro and
239 Ritzwoller, 2002](#)), and the mean, linear trend and the station response are removed. The
240 horizontal components (E and N) are then rotated into the radial (R) and transverse (T) directions
241 defined by the great-circle path between the earthquake and the station. AFTAN ([Bensen et al.,
242 2007](#)) is applied to determine the Rayleigh wave phase and group travel times, and the
243 amplitudes of both the vertical (V) and radial components are measured between 18 and 80 sec
244 period. The amplitude ratio between the two components (R/V) is used to evaluate the H/V ratio
245 as a function of period at the station location.

246 To insure the quality of the H/V measurements, we impose the following four control criteria.
247 First, the signal-to-noise ratio must be greater than 15 for Rayleigh waves on both the radial and
248 vertical components. Second, Rayleigh waves on the radial and vertical components are expected
249 to be phase shifted by 90° . Thus, we apply a phase difference criterion: measurements with
250 $|\varphi_R(T) - \varphi_V(T) - \pi/2| / (T/2\pi) > 2$ sec are removed, where φ_R and φ_V are the observed phase of the
251 radial (R) and vertical (V) components, respectively, and T is the period of the measurement.
252 Third, large H/V measurements (>10) are removed. These criteria are applied independently to
253 each station at each period. A final, fourth criterion is invoked in which we estimate the standard
254 deviation, σ , of the measurements at each station and at each period that satisfy the first three
255 selection criteria. To stabilize the measurements, we discard measurements outside the 2σ
256 corridor of measurements.

257 After these quality control steps, a set of H/V ratio measurements is obtained for each period at
258 each station. For sets with ≥ 20 measurements, the mean and standard deviation of the mean are
259 computed to represent the H/V ratio measurement and its uncertainty at this period and station.
260 We discard measurements at a station if the number of measurements is less than 20 in order to

261 enhance the reliability of the data set. At each station, the H/V measurements estimated from
262 different events are similar, although small variations ($<2\%$) dependent on back-azimuth are
263 observed. However, for about 15 stations the H/V ratio measurements possess large variations
264 ($>20\%$) over time. Conversations with IRIS/DMC staff members (personal communication with
265 Robert Busby, IRIS) suggest that these variations are probably due to a differential signal output
266 error of the seismometer sensors. **Table 2** lists these 11 stations with the time periods of
267 malfunction. Some of the H/V ratio measurements obtained during the malfunction periods can
268 be corrected whereas others must be discarded.

269 Example H/V maps at periods of 30 and 60 sec are presented in **Figure 3**. They are similar to the
270 maps shown by **Lin et al. (2012a)**, but the H/V ratios presented here are smaller on average and
271 extend over a larger area. At 30 sec period, high H/V ratio is correlated with the sedimentary
272 basin distribution across the continental US (e.g., the Central Valley in California; the Williston
273 Basin near eastern Montana and western North Dakota; the coastal basins near the Mississippi
274 embayment). Low H/V ratio is observed in major mountain ranges (e.g., the Sierra Nevada,
275 Rocky Mountains) in the western US, in the Superior upland province and the Appalachian
276 highlands in the eastern US, all regions devoid of thick unconsolidated sediments. Beneath the
277 Yellowstone hotspot and southern Sierra Nevada, the lowest H/V measurements across the
278 continent (<0.65) are observed. At longer periods, the H/V ratio is still largely sensitive to
279 shallow Vs structure. **Figure 24** later in the paper presents sensitivity kernels that demonstrate
280 this. Thus, the effect from major basins is still observed at long periods: the Green River Basin
281 in southwestern Wyoming and the Mississippi embayment areas possess the highest H/V
282 measurements at this period. The sensitivity kernel of the H/V measurement penetrates into the
283 mantle at long periods and is positively correlated with V_{sv} , so low H/V ratio is also observed
284 beneath the Rocky Mountains and the Snake River Plain where the mantle V_{sv} is low (**Fig. 2f**).

285 We construct H/V ratio curves for 1,779 stations between periods of 20 and 90 sec. Several
286 typical H/V ratio curves with uncertainties are presented in **Figure 6**.

287 **2.5 Measurement uncertainties**

288 We obtain estimates of uncertainties (or errors) for all types of measurements employed here:
289 Rayleigh wave group and phase velocity maps, receiver functions, and local Rayleigh wave H/V

290 ratios. Measurement errors averaged spatially across the US are shown in [Figure 4](#) for Rayleigh
291 wave dispersion and H/V measurements. Rayleigh wave phase speed measurement errors for
292 both ambient noise and earthquake data are typically less than about 10 m/s ([Fig. 4a](#)), which is
293 about 0.25% of the phase speed. For an inter-station path of 1000 km and a travel time of about
294 250 sec, this is about a half-second measurement error, which is largely independent of period.
295 Further improvements in surface wave tomography designed to beat down this error are needed,
296 and would be particularly useful to improve estimates of azimuthal anisotropy. For ambient
297 noise, errors in group velocity maps are scaled from phase velocity errors as discussed in section
298 2.2. They average about three times phase speed errors (Moschetti et al, 2010), but, as [Figure 4a](#)
299 shows, above 25 sec period phase speed errors remain low even as group speed errors grow
300 rapidly. This is because we introduced earthquake-derived measurements of phase speed at
301 longer periods. Spatially averaged estimates of Rayleigh wave H/V errors are presented in [Figure](#)
302 [4b](#). Because H/V measurements typically lie between 0.6-1.2 ([Fig. 3](#)), uncertainties in H/V
303 measurements typically range from about 1%-3% of the H/V value. We do not present a plot of
304 the average error in receiver functions, but several typical receiver functions with uncertainties
305 are shown in [Figure 6](#). Our receiver function error estimates are conservative and, therefore, we
306 do not attempt to fit small errors in the receiver functions.

307 The spatial variability of period-averaged measurement uncertainties is presented in [Figure 5](#) for
308 Rayleigh phase speed, group speed, and H/V ratio. Phase and group speed uncertainties are fairly
309 homogeneous spatially, but degrade near the periphery of the study region where azimuthal
310 coverage is sub-optimal. For H/V measurements, uncertainties are also spatially quite
311 homogeneous but are slightly higher in the central US than in the western or eastern US because
312 fewer earthquakes are observed there.

313 **2.6 Example data**

314 As discussed in section 3, we invert data at each station individually. Receiver functions and
315 Rayleigh wave H/V measurements are obtained independently at each station. However,
316 dispersion maps are produce on a spatial grid that extends between stations, but we interpolate
317 them to station locations so as to produce station-specific dispersion curves. Thus, at the vast
318 majority of stations across the US, we have Rayleigh wave group and phase speed curves as well

319 as a Rayleigh wave H/V curve and a receiver function, together with uncertainty estimates of all
320 quantities. Examples of such station-specific data are presented in [Figure 6](#) for the six stations
321 identified in [Figure 1b](#) with red stars. Rayleigh wave data are presented on a discrete grid of
322 periods with 1σ error bars. Receiver functions are presented in terms of a grey corridor, which
323 also represents the 1σ uncertainty at each time.

324 Much information about local structure can be seen directly in the data in [Figure 6](#). For example,
325 the reverberations in the receiver function, high H/V values at short periods, and slow short
326 period group velocities reveal that the stations at Lambert, MT and Gary, TX lie in sedimentary
327 basins. The strong Moho P-to-S phase conversion near 4.5 sec on the receiver function at
328 Winston, NM indicates that there is a sharp Moho there. A later P-to-S conversion at Crested
329 Butte, CO indicates a deeper Moho than at Winston, NM. The location of the airy phase on the
330 group velocity curve at longer periods than at Winston, NM similarly is consistent with a deeper
331 crust. The relatively flat receiver function at Red Bud, IL indicates a gradient or perhaps
332 complicated Moho structure, which is consistent with a relatively shallow (nearly horizontal)
333 airy phase on the group velocity curve.

334 **3. Joint Bayesian Monte Carlo Inversion**

335 We describe here the joint Bayesian Monte Carlo inversion. The inversion procedure is very
336 similar to that applied by [Shen et al. \(2013a,b,c\)](#) to Rayleigh wave dispersion and receiver
337 functions, except here the joint inversion is extended to incorporate measurements of Rayleigh
338 wave H/V ratios in three steps. In the first step, we perform an initial Monte Carlo inversion
339 without the involvement of receiver functions and the H/V ratio measurements. Such a inversion
340 produces a model of the crust and uppermost mantle V_{sv} for the contiguous US based on surface
341 wave dispersion alone. We refer to this as the surface wave or SW inversion. In the second step,
342 we introduce receiver function data and H/V measurements. [Figure 6](#) presents example fits to the
343 data for six stations and demonstrates the compatibility of the three data sets that are inverted
344 under the Bayesian Monte Carlo framework. The solid lines in each panel of [Figure 6](#) show
345 predicted data from the best-fitting model of the posterior distribution of models that results from
346 the joint inversion. In the third and final step, a new 3-D model constrained by all three types of
347 data (“All Data”) is generated. The model is determined from the posterior distribution of

348 accepted models beneath each station and model uncertainties are related to the spread of the
349 posterior distribution.

350 **3.1 Model specification**

351 At present, the only surface wave data we use are Rayleigh waves (and not Love waves), which
352 are primarily sensitive to V_{sv} . Thus, although we assume the model to be isotropic,
353 $V_{sv}=V_{sh}=V_s$, and we refer to the model as a V_s model, it is actually a V_{sv} model. The V_s model
354 beneath each station is stratified into three principal layers in which V_s changes smoothly
355 vertically. The top layer is the sedimentary layer defined by three unknowns: layer thickness and
356 V_s at the top and bottom of the layer with V_s increasing linearly with depth. The second layer is
357 the crystalline crust, parameterized with five unknowns: four cubic B-splines and crustal
358 thickness. Finally, there is the uppermost mantle layer with five cubic B-splines, yielding a total
359 of 13 free parameters at each location. Thus, V_s changes smoothly with depth in the crust and
360 mantle and, as discussed in the next paragraph, increases monotonically with depth in the crust.
361 We set the thickness of the uppermost mantle layer so that the total thickness of all three layers is
362 200 km. For the initial surface wave (SW) inversion, the model space is based on perturbations
363 to a reference model consisting of the 3D model of [Shapiro and Ritzwoller \(2002\)](#) for crustal V_s ,
364 crustal thickness, and mantle V_s . The initial sedimentary model is from [Mooney and Kaban](#)
365 [\(2010\)](#). [Table 3](#) presents a summary of the range of perturbations to model variables allowed in
366 the inversion.

367 In addition, the following three prior constraints are imposed during the Monte Carlo sampling
368 of model space. (1) V_s increases with depth across the two model discontinuities at the base of
369 the sediments and Moho. (2) V_s increases monotonically with depth in the crystalline crust. (3)
370 At all depths, $V_s < 4.9$ km/sec. These constraints are viewed as hypotheses to be tested. In the
371 sedimentary layer, we scale V_p and density from V_s according to [Brocher \(2005\)](#):

$$372 \quad V_p = 0.941 + 2.095V_s - 0.821V_s^2 + 0.268V_s^3 - 0.0251V_s^4, \quad (1)$$

$$373 \quad \rho = 1.227 + 1.53V_s - 0.837V_s^2 + 0.207V_s^3 - 0.0166V_s^4, \quad (2)$$

374 where we have rounded here to three significant figures. This scaling relationship makes the
375 V_p/V_s ratio greater than 2 in the sedimentary layer where $V_s < 3$ km/sec. In the crystalline crust
376 and uppermost mantle, the V_p/V_s ratio is fixed to be 1.75. Equation (2) is also used for density in

377 the crystalline crust. In the mantle, density is scaled from Vs perturbations relative to 4.5 km/s
378 with 10 kg/m^3 per 1% velocity change (Hacker and Abers, 2003). The Q model from PREM
379 (Dziewonski and Anderson, 1981) is used in the sedimentary layer and crystalline crust to apply
380 the physical dispersion correction (Kanamori and Anderson, 1977) and each resulting model is
381 reduced to 1 sec period. Shear Q in the mantle is set to be 150 across the entire study region and
382 with depth.

383 These choices reduce the volume of model space searched, but if they are inaccurate (as they will
384 be at some locations), they will impose a systematic error on the resulting models. Systematic
385 errors are discussed in section 5.3 and compared with random error, which we discuss in section
386 4.2.

387 **3.2 Prior and posterior distributions**

388 Shen et al. (2013b) describe Bayesian Monte Carlo joint inversion method in detail. The method
389 is influenced strongly by Mosegaard and Tarantola (1995). We only provide a cursory summary
390 here and concentrate on the presentation of the results. The joint inversion method constructs a
391 prior distribution of models at each location defined by allowed perturbations relative to the
392 reference model as well as model constraints. The principal output is the posterior distribution of
393 models that satisfy the receiver function and surface wave data (Rayleigh phase and group
394 speeds and H/V) within tolerances that depend on data uncertainties. The statistical properties of
395 the posterior distribution quantify aspects of model error as discussed later in the paper.

396 The Bayesian nature of the inversion refers to the fact that we sample model space to construct
397 explicitly both the prior and posterior model distributions and that the relationship between these
398 distributions is mediated by the Likelihood function and governed by Bayes Theorem. Let $\pi(\mathbf{m})$
399 be the prior distribution of models and $P(\mathbf{m})$ be the posterior distribution. Bayes Theorem tells us
400 that

$$401 \quad P(\mathbf{m}) = k L(\mathbf{m}) \pi(\mathbf{m}) \quad (3)$$

402 where k is a normalization constant (which does not affect the shape of the posterior distribution)
403 and $L(\mathbf{m})$ is the likelihood function, which is a measure of the degree of fit to the data by the
404 model \mathbf{m} as follows:

$$405 \quad L(\mathbf{m}) = \exp(-S(\mathbf{m})) \quad (4)$$

406
$$S(\mathbf{m}) = \sum_{i=1}^N \frac{(d_i - d_i^{\text{pred}})^2}{2\sigma_i^2} \quad (5)$$

407 Here d_i is an observation with uncertainty σ_i , d_i^{pred} is the predicted datum from model \mathbf{m} , and N is
 408 the number of observations. [Shen et al. \(2013b\)](#) modified the likelihood function by introducing
 409 an additional weight to discriminate between the dispersion measurements and receiver functions
 410 in the likelihood function (further downweighting the receiver functions) but that is not done
 411 here. The only data weights are the estimated measurement errors.

412 The posterior distribution reflects both the prior constraints and the data used in the inversion.
 413 The Monte Carlo nature of the inversion refers to the fact that the search of model space is a
 414 stochastic process in which Markov chains of models are governed by a transition probability
 415 that depends on the fit to the data. The transition probability we use is the Metropolis Law, as
 416 described by [Shen et al. \(2013b\)](#). For each station we retain on average about 8500 models in the
 417 posterior distribution. Most of these models are not statistically independent of one another and
 418 we discuss the impact of this fact on our interpretation of the posterior distribution in section 4.1.

419 Examples of marginal prior and posterior distributions for particular model characteristics are
 420 shown for two stations in [Figure 7](#), in which there is an explicit comparison between results
 421 using surface wave dispersion alone (SW) and using all three data sets (All Data: surface wave
 422 dispersion, receiver functions, H/V measurement). The prior distribution is represented with the
 423 grey histograms, the posterior distribution based on Rayleigh wave dispersion alone is presented
 424 as the black-outlined white histograms, and the posterior distribution based on all three data sets
 425 is shown with the red histogram. As seen in [Figure 6a](#), because of a clear Moho P-to-S
 426 conversion in the receiver function at station Z21A (Winston, NM), the joint inversion better
 427 constrains lower crustal Vs and crustal structure ([Fig. 7b,c](#)). Surface wave data alone do not
 428 constrain either crustal thickness or the jump in Vs across Moho at this station well. As seen in
 429 [Figure 6c](#) (Lambert, MT), the receiver function and H/V ratio are characteristic of thick
 430 sediments, and the joint inversion better constrains shallow crustal structure than the inversion
 431 with surface wave dispersion alone ([Fig. 7d](#)). Because reverberations in the receiver function
 432 obscure a possible Moho P-to-S conversion in the receiver function, the joint inversion does not,
 433 however, constrain lower crustal structure or crustal thickness appreciably better than the surface
 434 wave dispersion data alone ([Fig. 7e,f](#)). The details of the inversion at each station depend on the

435 nature of the receiver function and H/V measurements, but on average the vertical discontinuity
436 structure of the crust is clarified, and the vertical resolution of the model is improved by
437 introducing these data into the inversion with surface wave dispersion data. This is discussed
438 further in section 4.3 below.

439 We present examples of resulting models at a variety of locations in [Figure 8](#). Each model is
440 presented beneath a single station and corresponds to the data presented in [Figure 6](#). At each
441 depth the width of the full posterior distribution is shown, as are the mean and standard deviation
442 of the posterior distribution which we use to summarize the 3D model.

443 **3.3 Fit to the data**

444 There are fairly strong constraints imposed in the inversion, including the smoothness of the
445 model between discontinuities, the monotonic increase of shear wave speeds with depth in the
446 crust, particular relationships between V_s , V_p , and ρ as a function of depth, and a specified range
447 of values considered for each model variable ([Table 3](#)). These constraints are imposed to reduce
448 the model space searched and make the Monte Carlo search more efficient, but we view them as
449 hypotheses which are tested in the inversion. The first question we have is whether the model is
450 sufficiently flexible to allow the data to be fit across the entire region of study. If the data can be
451 fit subject to the constraints, then extending the model beyond the constraints is not substantiated
452 by the data alone. There may be good reasons to believe that the earth does not satisfy the
453 particular constraints imposed here, but if the data are fit subject to the constraints this issue
454 needs to be taken up in the construction of the prior distribution.

455 [Figure 9](#) presents a summary of data fit in the joint inversion of all three data types, in which the
456 square root of reduced chi-squared is shown for Rayleigh wave phase speed, Rayleigh wave
457 group speed, Rayleigh wave H/V measurements, and receiver functions. We refer to the square
458 root of reduced chi-squared misfit as “reduced χ misfit”, which is defined as follows:

$$459 \quad \chi_{red} = \sqrt{\chi_{red}^2} = \left(\frac{2}{N} S(\mathbf{m}) \right)^{1/2} \quad (6)$$

460 where $S(\mathbf{m})$ is the misfit function defined for model \mathbf{m} by equation (5) and N is the number of
461 observations. Misfit to the Rayleigh wave data ([Fig. 9a-c](#)) is averaged over period and misfit to
462 the azimuthally independent receiver functions is averaged over time (from 0 to 10 sec). A χ_{red} of

463 unity means that the data are fit on average at the level of 1σ , where σ represents data error, a
464 value of 2 implies that the data are fit on average at the level of 2σ , and so forth.

465 On average, Rayleigh wave phase and group speeds are fit to better than 2σ (Fig. 9a,b).
466 Exceptions occur in regions of thick sediments where short period group speeds are particularly
467 sensitive; e.g., the Mississippi Embayment and Gulf Coast, the Green River basin of
468 southwestern Wyoming, the Central Valley of California. In these regions, greater flexibility in
469 the construction of the sedimentary model is probably required, perhaps to include a larger range
470 and perhaps different depth variation of the V_p/V_s ratio and relaxation of the constraint on the
471 monotonic increase of V_s with depth in the basin. H/V is also fit on average to better than 2σ
472 (Fig. 9c) but there are more regions where the data are fit poorly. Again, most of these are in
473 sedimentary basins and H/V is strongly sensitive to sedimentary structure. The overall higher
474 level of misfit for H/V illustrates that this datum tends to compete with short period group speeds
475 in the inversion. These two data types can be reconciled on average, but greater model flexibility
476 is probably needed in several locations across the US. We have chosen not to allow this greater
477 flexibility here, choosing instead a single parameterization across the US for simplicity. The
478 model presented in this paper is not intended to be the last word on structure across the US. As
479 Figure 9d shows, receiver functions are typically fit to better than 1σ across the US. There are
480 exceptional stations where azimuthally-independent receiver functions cannot be well fit jointly
481 with the other data in the inversion, but they are rare. The exceptional fit to the receiver functions
482 may mean that we have somewhat overestimated the uncertainties in the receiver functions. The
483 effect is that we do not attempt to fit small wiggles in the azimuthally-independent receiver
484 functions.

485 **4. Results**

486 At each location and for each depth, we summarize the posterior distribution of models with its
487 mean (\bar{m}) and standard deviation (σ_m). Examples of the mean and standard deviation of the
488 posterior distribution can be read off the vertical profiles shown in Figure 8. The addition of
489 different data into the inversion makes the posterior distributions increasing Gaussian in
490 character. This effect can be seen clearly in the marginal distributions presented in Figure 7. For
491 example, at station Z21A (Fig. 6a-c), the prior distributions are approximately uniform for all
492 three model variables. For the inversion using surface wave data alone, the posterior distribution

493 is strongly bi-modal in the lower crust and fairly uniform for crustal thickness. However, when
494 receiver functions and H/V measurements are added to the inversion, the posterior distributions
495 are much more Gaussian in shape and not multi-modal. This is also true for stations C23A in the
496 shallow crust (Fig. 6d) where the introduction of H/V measurements strongly has affected the
497 posterior distribution. However, the posterior distribution in the lower crust and for crustal
498 thickness is bi- or multi-modal (Fig. 6e-f) because sedimentary reverberations in the receiver
499 function at this location obscure constraints on crustal thickness. At most locations and for most
500 model characteristics across the US, the mean and standard deviation provide reliable summaries
501 of the posterior distribution except in a small minority of cases when lower crustal and Moho
502 distributions may bifurcate. Thus, in the following we summarize the model in terms of these
503 statistics, (\bar{m}, σ_m) , but retain the caveat that in some locations (particularly in sedimentary
504 basins) the posterior distribution may possess complications not captured by the mean and
505 standard deviation. To define the final 3D model, we follow Shen et al. (2013a,b) and apply
506 simple kriging to interpolate the depth dependent quantities (\bar{m}, σ_m) onto a $0.25^\circ \times 0.25^\circ$ grid,
507 and construct a uniform model of the crust and uppermost mantle to a depth of 150 km across the
508 US.

509 **4.1 Regionally averaged models and variations within each region**

510 Before turning to discuss the sub-regional scale variations in the 3D model, we first seek to
511 assess large-scale averages and variations in the model. To do this we divide the contiguous US
512 into three regions, identified in Figure 10a as the western region, the continental core region, and
513 the eastern region. The eastern region also encompasses much of the South, and is perhaps best
514 viewed as the margin of the continent that has been tectonically modified with influence from the
515 South and East. Figure 10b presents the three regional averages computed from the mean of the
516 posterior distribution at each station across each region. At each location we stretch or compress
517 the crustal model vertically to match the average crustal thickness in the region before computing
518 the regional average. Similarly, depth in the mantle is taken relative to Moho depth which we
519 then normalize to the average Moho depth. Not surprisingly, the recently tectonically deformed
520 western region is distinct, with considerably slower crust and mantle and thinner crust than the
521 other regions. The eastern region is also somewhat slower than the core region with a thinner
522 crust.

523 Spatial variations across each of the three regions are shown in [Figure 10c](#), in which the standard
524 deviation relative to the regional mean is presented at each depth. Spatial variability is greatest
525 near the surface, which is caused predominantly by variations between locations with and
526 without sediments. Due to the exceptionally thick sediments in the Mississippi Embayment, the
527 greatest shallow variability lies in the eastern region. In the middle crust, the western region is
528 considerably more variable (~3%) than the other regions, being approximately twice as variable
529 as in the core region (~1.5%). Variability peaks up near the Moho due to lateral variations in
530 Moho structure; some locations have a gradient Moho others have a sharp Moho. These
531 variations have a greater imprint on uppermost mantle structure than on lower crustal structure
532 and decay quickly with depth in the mantle. In the mantle, regional variations lie between 1.5%
533 (eastern region) and 3% (western region). The core region has larger geographical variations in
534 the mantle than the eastern region due to heterogeneity beneath the western Great Plains, which
535 appears to be affected by orogens that lie largely in the western region and affect crustal structure
536 only in the western region. Mantle heterogeneity in the core region, which is about 2%, is
537 actually larger than mid-crustal heterogeneity in that region (~1.5%).

538 **4.2 Assessing model uncertainty: Fluctuations, random errors, and systematic errors**

539 In order to interpret the spatial variations observed in the means of the posterior distributions, it
540 is necessary to compare them with estimates of model uncertainties. One candidate for model
541 uncertainty is the standard deviation of the posterior distribution, σ_m , whose average across the
542 contiguous US as a function of depth is shown with the solid black line in [Figure 11a](#). Average
543 values for σ_m are about 1.5% in the crust, although they dip appreciably in the middle crust, and
544 are somewhat larger in the mantle (~1.8% on average). These values peak near the free surface
545 and Moho due to trade-offs between internal structures and boundary topography.

546 A great many factors affect the standard deviation of the posterior distribution, σ_m . Posterior
547 distributions are affected by uncertainties in the data, which control which models are accepted
548 to form the distributions, but they are also affected strongly by trade-offs between model
549 variables at different depths. Vertical model oscillations are particularly troublesome and
550 important, and are often non-physical. In defining the prior distribution, we have attempted to
551 limit such oscillations and trade-offs by introducing vertically smooth basis functions as well as
552 model constraints (positive jump across discontinuities, maximum velocity in each layer,

553 monotonic increase of shear wave speed in the crust). Nevertheless, the spread of the posterior
 554 distribution still reflects such effects and, as a consequence, strongly reflects the model prior.
 555 Indeed, relaxing the prior constraints produces more vertically oscillatory models which
 556 produces a larger standard deviation in the posterior distribution, but with a much smaller impact
 557 on the mean of the distribution. For this reason, the standard deviation of the posterior
 558 distribution σ_m does not provide an ideal estimate of the stability or reliability of the mean of the
 559 posterior distribution, which we take as the value of the model at each location and depth.

560 The inadequacy of σ_m to measure model uncertainty can be seen further by comparing the
 561 spatially averaged σ_m , shown with a solid black line in [Figure 11a](#), with the spatial variations
 562 within each of the three regions, shown in [Figure 10c](#). The spatially averaged σ_m is about the
 563 same size as the variations within each region. If σ_m were used as the estimate of model
 564 uncertainty, then the interpretation of structural variations within regions may be questionable.
 565 The geological coherence of the model and the stability of the posterior distributions, however,
 566 imply that σ_m is an overly conservative estimate of model uncertainty, albeit one that captures
 567 an estimate of the relative reliability of the resulting model. An example of this is shown in
 568 [Figure 11b](#), which illustrates that the mean of the posterior distribution at 70 km depth in the
 569 mantle changes smoothly along the Snake River Plain, and fluctuates at a level much smaller
 570 than σ_m .

571 We seek a more useful estimate of model uncertainty than σ_m . In doing so we would like to
 572 discriminate between model fluctuations, which we interpret as random errors caused
 573 predominantly by observational errors, from systematic errors caused by choices made in the
 574 construction of the prior distribution, including such things as model parameterization, the extent
 575 of the model space searched, and constraints imposed in the inversion. Let us define the notation
 576 $\langle . \rangle$ to mean the expected value of an estimated quantity, and “e” to represent model error.
 577 Thus, the expected value of the estimated model, $\langle \mathbf{m} \rangle$, will be a combination of the real model,
 578 \mathbf{m} , and the estimated error, $\langle \mathbf{e} \rangle$, as follows:

$$579 \quad \langle \mathbf{m} \rangle = \mathbf{m} + \langle \mathbf{e} \rangle = \mathbf{m} + \langle \mathbf{e}_{\text{sys}} + \mathbf{e}_{\text{ran}} \rangle = \mathbf{m} + \langle \mathbf{e}_{\text{sys}} \rangle + \langle \mathbf{e}_{\text{ran}} \rangle \quad (7)$$

580 We consider the model error to arise from two components, a systematic (\mathbf{e}_{sys}) and a random
 581 (\mathbf{e}_{ran}) contribution. The last equality in equation (7) follows from the assumed independence

582 between the systematic errors, which are caused locally by the deviation of the earth from our
583 assumptions and constraints, and the random errors, which are caused by other non-systematic
584 factors such as measurement errors.

585 Our approach is to equate random error with model fluctuations, which are inversely related to
586 the stability of the mean of the posterior distribution. The aim is for our assessment of random
587 error to reflect the fluctuations observed in the model, such as those seen in [Figure 11b](#) along the
588 Snake River Plain. We posit that the standard deviation of the mean of the posterior distribution,
589 $\sigma_{\bar{m}}$, provides a reasonable estimate of the stability of the mean of the model or the random error
590 in the model, $\langle e_{\text{ran}} \rangle$, and that this error is controlled largely (but not exclusively) by
591 measurement error. One method to estimate $\sigma_{\bar{m}}$ is to scale the standard deviation of the posterior
592 distribution (σ_m) by the inverse square root of the number of independent models in the
593 distribution. We describe how we estimate the number of independent models in the next
594 paragraph, but when we apply the scaling we obtain an average $\sigma_{\bar{m}}$ across the US shown with a
595 dashed line in [Figure 10c](#) and a red line in [Figure 11a](#). We estimate that on average in the central
596 crust is about 0.2% and in the mantle to about 100 km depth it is about 0.4% except directly
597 beneath Moho. These values are considerably smaller than the variations we observe within the
598 three regions of [Figure 10](#) and fairly represent our degree of belief in the model characteristics.
599 The variations in structure within the regions are the subject of sections 4.3, 4.4, 5.1, and 5.2.

600 The standard deviation of the mean of the posterior distribution, $\sigma_{\bar{m}}$, which we identify with the
601 random model error, is determined from the mean of the posterior distribution here by dividing
602 by a number between 4 and 5. We arrive at this range by determining that the number of
603 independent models in the posterior distribution is 0.2% - 0.3% of the models in the distribution.
604 The average number of models in the posterior distribution is about 8500; thus only between
605 about 16 and 25 models are independent, on average, and applying the square root we get a
606 scaling factor of 4 or 5. The procedure we use to determine the number of independent models is
607 based on the discussion of [Mosegaard and Tarantola \(1995\)](#), who present a method based on
608 analyzing the likelihood function within the equilibrium part of each Markov chain. Let $\{m_i\}$ be
609 an ordered set of models that compose the equilibrium part of a Markov chain sampling of model
610 space. Typically, the Likelihood function increases in magnitude as the Markov chain progresses
611 from the initial or seed model and then plateaus (e.g., [Shen et al., 2013b, Fig. 8](#)) where it

612 oscillates. The equilibrium part of the Markov chain is the plateau region. Now consider the
613 discrete function $L(m_i)$, which is the likelihood as a function of model number within the
614 equilibrium region of the Markov chain. Mosegaard and Taratola suggest computing the
615 autocorrelation of $L(m_i)$ such that the number of models that are required for the autocorrelation
616 to return to 0 is the number of models needed to re-establish statistical independence. Given our
617 sampling algorithm, we find that the Markov chain has to march through between 300 and 500
618 accepted models before it achieves independence relative to its starting state. Thus, only
619 approximately 1 in 300 to 500 models in the posterior distribution are independent. This means
620 that, on average, the local standard deviation of the distribution should be divided by between 4
621 and 5 to estimate the standard deviation in the mean of the distribution, $\sigma_{\bar{m}}$, which we equate
622 with $\langle e_{\text{ran}} \rangle$.

623 As a consistency test of this estimate of the standard deviation of the mean of the posterior
624 distribution, $\sigma_{\bar{m}}$, we have performed several brute force calculations of the standard deviation of
625 the mean for a number of stations by re-running the Bayesian Monte Carlo inversions many
626 times. This allows us to construct a set of different posterior distributions from which we can
627 compute the standard deviation of the mean across these distributions. The results for station
628 X57A (Hartsville, SC) are shown in [Figure 11c](#), which compares the standard deviation of the
629 mean with the original standard deviation of the posterior distribution at this point. On average,
630 from 5 to 150 km depth, the standard deviation of the mean, $\sigma_{\bar{m}}$, is about 25% of the standard
631 deviation of the posterior distribution, σ_m . This result is consistent with the scaling analysis
632 based on the Likelihood function, but is numerically much more expensive to compute. We
633 obtain similar but not identical results at other stations.

634 In the rest of the paper and in all figures, when summarizing the posterior distribution we will
635 present the standard deviation of the posterior distribution, σ_m , which provides a reasonable
636 relative error estimate. To estimate the random error in order to quantify the stability of the
637 model, however, one should divide these values by 4 - 5 to get a better estimate of the standard
638 deviation of the mean, $\sigma_{\bar{m}}$. The standard deviation of the mean not only includes the effect of
639 measurement errors but also the effects of covariances between model variables and, therefore,
640 remains a fairly conservative estimate of model uncertainty caused by random errors. However,
641 the standard deviation of the mean does not include the effect of systematic errors caused by

642 erroneous assumptions and constraints imposed in the inversion. An assessment of the nature and
643 potential magnitude of systematic error is presented in section 5.3.

644 **4.3 Crustal model**

645 Horizontal slices of the mean of the posterior distribution for several depths in the crust are
646 presented in [Figure 12](#). [Figure 12a,b](#) illustrates the effect on estimated shallow structures of the
647 inclusion of receiver functions and Rayleigh wave ellipticity measurements. Sedimentary basins
648 dominate the structural variations in the top 5 km of the crust. The introduction of receiver
649 functions and Rayleigh wave ellipticity measurements brings shallow structures, notably
650 sedimentary basins, into sharper focus both laterally and vertically. This improves the crustal
651 model, at least in the upper half of the crust.

652 There are a great many crustal features worthy of note and serious discussion, but this is beyond
653 the scope of this paper. However, we note that there is stronger variation across the mid-
654 continent in the middle crust than in the lower crust. We believe that the relatively low wave
655 speeds (green anomalies) in the middle crust in [Figure 12c](#) across Nebraska, Kansas, Missouri,
656 and Iowa are what [Chu and Helmberger \(2014\)](#) refer to as the “massive low velocity zone in the
657 lower crust”. If so, it is in fact a mid-crustal feature and although large in areal extent is only
658 slow in a relative sense.

659 We note that the discussion in section 4.1 based on the regionalization of the US into three
660 regions was motivated by lower crustal structure, which is quite homogeneous across the core of
661 the continent between the Rocky Mountain Front and the Greenville Front, which cuts across the
662 South and eastern Midwest of the US.

663 The mean of the posterior distribution for crustal thickness is presented in [Figure 13](#). The
664 thickest crust lies under the Rocky Mountains in Colorado, and the thickest crust in the East is
665 beneath the Appalachian Mountains. These results are not surprising, but there are many local
666 variations in crustal thickness that deserve greater attention than we can pay them here; e.g., the
667 very thin crust of eastern North Dakota, the thick crust extending from western New York
668 through Kentucky in the region between the Greenville Front and the Appalachian Mountains,
669 and the large region of relatively thick crust spanning the Mid-Continent Rift.

670 The mean of the posterior distribution of the vertical jump in Vs from the crust to the mantle is
671 presented in [Figure 14](#). On average Vs increases across the Moho from the crust to the mantle
672 by about 300 m/s. However, there is substantial variation. For example, there are much larger
673 jumps across the Moho in much of the Basin and Range province and in southern Ontario
674 between Lake Huron and Lakes Erie and Ontario. However, much smaller jumps produce a near
675 gradient Moho, which is observed beneath the Colorado Plateau, in the Pacific Northwest
676 overlying the subducting slab, beneath Illinois and in other places distributed across the US.

677 The standard deviation of the posterior distribution of crustal velocities, crustal thicknesses, and
678 the jumps in Vs across Moho, are presented in [Figures 15, 13b, and 14b](#), respectively. As
679 discussed in section 4.2, to obtain an estimate of the standard deviation of the mean of the
680 posterior distribution, which is a better representation of the random error in the model, one
681 should divide the uncertainties shown in [Figures 15, 13b, and 14b](#) by approximately 4-5.

682 Uncertainties in the Vs jump across Moho are presented in [Figure 14b](#). Generally, uncertainties
683 are largest where the jumps in Vs are largest; for example, the Basin and Range and the Colorado
684 Rocky Mountains. Large jumps are usually imposed by the receiver functions, which do not
685 provide precise constraints on the magnitude of the jump in Vs.

686 Uncertainties in crustal velocities grow toward the top and bottom of the crust, as shown in
687 [Figure 11a](#) and discussed already, and are quite laterally homogeneous across the US ([Fig. 15](#)).
688 They are largest in the Mississippi Embayment due to the extremely thick sediments found there.
689 The geographical pattern of uncertainties in crustal thickness correlates with crustal thickness
690 such that the larger uncertainties tend to be near the core of the continent. The depth of Moho for
691 thicker crust is simply harder to determine than for thinner crust because the airy phase in the
692 group velocity curve, which reflects crustal thickness, migrates to longer periods and is more
693 difficult to resolve clearly. The introduction of receiver functions in the inversion reduces the
694 uncertainty in crustal thickness, on average. This is shown in [Figure 16a](#). The inversion of surface
695 wave dispersion together with receiver functions and Rayleigh wave ellipticity reduces
696 uncertainty in Moho depth at about 2/3 of the stations. At the other stations, however, the
697 introduction of receiver functions in the inversion actually increases the uncertainty. In many
698 cases this is because the receiver function reveals that the station is underlain by a gradient Moho
699 or a complicated Moho structure such that crustal thickness is difficult to resolve. Indeed, the

700 uncertainty in crustal thickness is strongly correlated with the jump in V_s across Moho as **Figure**
701 **16b** shows. A gradient Moho, characterized by a small jump at Moho, tends to produce large
702 uncertainties in crustal thickness.

703 **4.4 Mantle model**

704 Uppermost mantle structure directly beneath the Moho varies strongly across the US as shown in
705 **Figure 17**. Across most of the US, the vertical slope of uppermost mantle V_s right beneath the
706 Moho is essentially neutral such that V_s changes only minimally with depth. A vertical profile
707 that provides an example of this is at Hartsville, SC, and is seen in **Figure 8f**. Such locations are
708 colored white in **Figure 17**. At some locations, however, there is a strong negative slope with
709 depth in the uppermost mantle, which typically indicates the existence of a low velocity zone
710 (LVZ) in the shallow mantle. Such locations are identified with warm colors in **Figure 17** and are
711 mainly confined to the western US. An example vertical profile is at Crested Butte, CO as can be
712 seen in **Figure 8b**. In contrast, some locations have a positive slope with depth, meaning that
713 there is no LVZ in the shallow mantle. Such locations are identified with cool colors in **Figure 17**
714 and are mainly found in the eastern US. An example vertical profile is at Red Bud, IL as can be
715 seen in **Figure 8e**. Typically, shallow mantle LVZs are found across much of the western US
716 outside the Wyoming craton, the Colorado Plateau, and the Cascadia subduction zone. The
717 strongest positive slopes in the uppermost mantle occur between the Greenville Front and the
718 Appalachian Mountains, although weaker positive slopes also extend across large parts of the
719 Midwest.

720 Several horizontal slices of V_s at depths of 70, 90, and 120 km in the upper mantle are presented
721 in **Figure 18**. The most prominent contrast is the East-West dichotomy. Many of the structural
722 features within the West (e.g., Snake River Plain and High Lava Plains low velocity anomaly,
723 rimming low velocity anomalies around the Colorado Plateau, Wyoming craton) are well known
724 now, as they appeared in earlier studies that were prefaces to the current paper (e.g., Moschetti et
725 al., 2007, 2010a,b; Yang et al., 2008, 2011; Bensen et al., 2009; Lin et al., 2011; Shen et al.,
726 2013a,b,c). Unlike low velocity anomalies that typically attenuate with depth, the Wyoming
727 craton high velocity anomaly increases with prominence with depth. The Cascadia slab is
728 apparent at 120 km depth. The most prominent upper mantle anomaly in the East is the Reelfoot
729 Rift (Pollitz and Mooney, 2014), which is predominantly a shallow low velocity mantle anomaly.

730 Relative low velocities in the uppermost mantle also underlie the Appalachian Mountains, the
731 most prominent of which are found beneath New England and western Virginia.

732 The standard deviation of the posterior distribution in upper mantle shear wave speeds is
733 presented in [Figure 19](#). Again, as discussed earlier, to obtain a better estimate of the random
734 error in the model, one should divide the uncertainties shown in [Figures 19](#) by approximately 4-
735 5. Uncertainties are fairly homogeneous with location across the US but grow below 100 km
736 depth as [Figure 11a](#) indicates.

737 **5. Discussion**

738 The features of the model are often most clearly discerned in vertical transects. Here we expand
739 the discussion of model features by discussing four long East-West transects across the entire US
740 as well as three pairs of shorter vertical profiles situated in crossing patterns through notable
741 features: the Snake River Plain, the Reelfoot Rift, and the Appalachian Mountains with the bulls-
742 eye of the last pair of profiles in western Virginia. The locations of these profiles are identified in
743 [Figure 20](#). In addition, we discuss the potential for systematic bias of the resulting 3D model. In
744 particular, we consider the effect of the assumed relation between V_s and density as well as our
745 assumption of a constant intermediate Q value of 150 in the mantle.

746 **5.1 Long East-West transects through the model**

747 [Figure 21](#) presents vertical transects through the 3D model across the entire US along four lines
748 of latitude: A-A' 46.5°N, B-B' 42°N, C-C' 38°N, D-D' 34°N. As with the horizontal views of
749 the model shown in [Figures 12](#) and [18](#), the vertical transects present the mean of the posterior
750 distribution at each depth derived from the model based on all data: surface wave dispersion,
751 receiver functions, and Rayleigh wave H/V measurements. Each vertical transect is divided into
752 a “crustal panel”, which presents the top 60 km, and a “mantle panel”, which presents depths
753 from 30 to 150 km. The vertical exaggeration of the crustal panel is greater so that crustal
754 features can be seen. Crustal velocities are presented as absolute quantities, but mantle velocities
755 are presented as perturbations relative to 4.4 km/s.

756 Transect A-A' goes through the northern Cascades and northern Rocky Mountain Cordillera, the
757 Great Plains of Montana, North Dakota, and Minnesota, through the Upper Peninsula of
758 Michigan and parts of Lake Superior, through southern Ontario and Quebec, and then terminates

759 near the northern tip of Maine. Six model features are particularly noteworthy, which we discuss
760 from west to east, most of which are near the western end of the profile. (1) The supraslab mantle
761 wedge is imaged as a slow feature in the uppermost mantle beneath the Cascades. The
762 subducting slab lies to the west of the wedge and appears as relatively fast locally. (2) Shallow
763 low velocities underlie the Pasco basin of south-central Washington. (3) Relatively low crustal
764 velocities lie beneath the Cordillera, although the thickest crust along the transect lies east of the
765 Cordillera beneath the Great Plains of Montana and western North Dakota. (4) The fast mantle
766 wave speeds of the Great Plains set on slowly east of the Cordillera through eastern Montana so
767 that there is no abrupt onset of high mantle wave speeds in the West at this latitude. (5) In eastern
768 North Dakota, crustal thickness reduces abruptly and enigmatically. (6) The model is relatively
769 homogeneous from Minnesota eastward both in the crust and mantle, with the highest wave
770 speeds in the mantle occurring from Minnesota to Michigan.

771 Transect B-B' extends along 42°N from the southern Cascades, through the northern Basin and
772 Range province and high lava plains, through the Wyoming Craton and central Great Plains, and
773 terminates in eastern Massachusetts. We highlight four features from west to east. (1) The
774 relatively high-velocity subducting slab contrasts with the exceptionally low velocity supraslab
775 mantle wedge, which merges with the slow upper mantle beneath the Basin and Range province
776 and high lava plains to the east. (2) The very slow Green River sediments overlie the Wyoming
777 craton that has velocity anomalies that amplify with depth in the mantle. (3) Relatively slow
778 mantle velocities lie between the Wyoming craton and the Great Plains, following the “Cheyenne
779 Belt” (e.g., [Houston et al., 1989](#)) from northeastern Colorado to the Black Hills ([Fig. 18b,c](#)) of
780 southwestern South Dakota. (4) Fast mantle velocities found across the eastern US terminate
781 abruptly near the edge of the northern Appalachians in eastern New York.

782 Transect C-C' extends along 38°N from the Great Valley of California, through the Sierras, the
783 Basin and Range province, the Colorado Plateau and Rockies, the Rio Grande Rift and then
784 across the central Great Plains and Appalachians to terminate near the coast of central Virginia.
785 This transect has a large number of noteworthy features, which we again discuss them from west
786 to east. (1) The sediments of the Great Valley appear clearly. (2) Low upper mantle velocities
787 underlie the central Basin and Range province beneath a clearly defined mantle lid. As seen in
788 [Figure 14](#), some of the strongest uppermost mantle negative vertical velocity gradients exist in
789 the central Basin and Range province. This is not because uppermost mantle velocities beneath

790 the central Basin and Range province are the lowest across the continent, but because of the
791 existence of a high velocity lid right below Moho. (3) The crust and mantle of the Colorado
792 Plateau are distinct from surrounding areas, being much faster than the Basin and Range or the
793 Colorado Rockies. (4) In contrast, the crust and mantle of the Colorado Rockies are quite slow
794 and the thickest crust along this transect occurs beneath the Rockies. (5) High velocities in the
795 crust and mantle beneath the Great Plains set on rapidly east of the Rocky Mountain front,
796 although the transition occurs near to the front in the crust and farther to the east in the mantle.
797 (6) Low velocities occur in the mantle beneath the eastern Appalachians in western Virginia near
798 the eastern edge of thick crust. Thinner crust is observed in eastern Virginia but it is underlain by
799 faster mantle.

800 Finally, transect D-D' extends along 34°N from the southern California coast near Los Angeles,
801 through the Coastal Range and Mojave Desert, through the southern Basin and Range Province,
802 across the Rio Grande Rift, through the southern Great Plains, the Mississippi Embayment and
803 the Reelfoot Rift, and the southern Appalachians, to terminate near the coast of southern North
804 Carolina. (1) Low velocity mantle underlies the Mohave Desert and southern Basin and Range
805 province, but as with the Basin and Range farther north there is a significant relative high
806 velocity lid in the uppermost mantle. (2) The lowest mantle wave speeds lie beneath the Rio
807 Grande Rift, and they are shallower than the lowest velocities beneath the Basin and Range
808 province. (3) The Great Plains high velocities in the mantle set on abruptly near the eastern
809 terminus of the Rio Grande Rift. (4) At this latitude, the thickest Mississippi Embayment
810 sediments lie just to the west of the Reelfoot Rift, which appears as a shallow mantle relative low
811 velocity feature. (5) Relatively low wave speeds in the uppermost mantle extend from the
812 Reelfoot Rift in southern Arkansas across the southern US to eastern South Carolina and then are
813 replaced by faster mantle shear wave speeds nearer to the Atlantic coast.

814 **5.2 Shorter crossing transects through the model**

815 The transects X1 and X2 in [Figure 22a](#) run along and across the Snake-River Plain (SNP).
816 Profile X2 runs along the SNP. The slow mantle velocities predominantly lie between depths of
817 50 and 100 km, deepen slightly to the southwest along the SNP, and are slowest where the SNP
818 crosses 42.7°N latitude, which is considerably west of Yellowstone. The crossing profile, X1,
819 illustrates the cross-sectional width of the low velocity anomaly in the mantle beneath the SNP.

820 This profile also contrasts the SNP low velocity anomaly with the high velocities beneath the
821 Wyoming craton southeast of the SNP. The velocity anomaly beneath the Wyoming craton
822 intensifies with depth in contrast to the shallower focus of the low velocity anomaly beneath the
823 SNP.

824 Transects Y1 and Y2 in [Figure 22b](#) run through a geologically much older feature, the Reelfoot
825 Rift. The amplitude of the velocity anomaly is, therefore, smaller. The profile along the rift, Y2,
826 shows that the lowest mantle shear wave speeds lie between depths of about 50 and 90 km. The
827 lowest velocities lie in a nearly horizontal band, but relatively low velocity anomalies extend
828 deeper into the mantle in the southwestern part of the profile. The crust thickens along the rift to
829 the northeast and becomes faster in the northern part of the rift compared to the southern rift, as
830 evidenced by upward curved crustal isolines. The crossing profile, Y1, reveals the width of the
831 mantle low velocity anomaly. The low velocity anomaly beneath the far southern extent of the
832 Appalachians in the shallow mantle also can be seen in profile Y1.

833 Transects Z1 and Z2 in [Figure 22c](#) lie along and transverse to the Appalachian Mountains,
834 crossing in western Virginia. Transect Z2 highlights that along the Appalachians there are three
835 centers with mantle low velocity anomalies: beneath northern Georgia, beneath the Blue Ridge
836 Mountains of western Virginia, and below the Green Mountains and White Mountains of New
837 England. The transverse profile in Z1 goes through western Virginia and shows that the anomaly
838 is concentrated in the shallow mantle, but extends through the model to at least 150 km. This is
839 in contrast the northern Georgia anomaly, which is confined to the shallow mantle above 80 km
840 depth, but is similar to the anomaly beneath New England. The New England velocity anomaly
841 is considerably stronger than the other two along the Appalachians and is arguably stronger than
842 the anomaly that underlies the Reelfoot Rift. We note that [Chu et al. \(2013\)](#) discuss a potential
843 Cretaceous hot spot track that would lie along the central and northern Appalachians, from
844 western Virginia into New England where mantle low velocities are seen in [Figure 22c](#).

845 Due to different average velocities in the mantle and different color scales it may not be
846 immediately obvious that the velocity anomalies in [Figure 22](#) beneath the Snake River Plain are
847 much slower than beneath the Reelfoot Rift and the Appalachians. The lowest velocities beneath
848 the SNP are about 8% below 4.3 km/s (~ 3.96 km/s) but the lowest velocities beneath New
849 England are only about 4% below 4.55 km/s (~ 4.36 km/s). Nevertheless, mantle structure

850 beneath the Reelfoot Rift and the Appalachians illustrates that significant mantle heterogeneity
851 occurs across the central and eastern US.

852 **5.3 Potential for systematic error**

853 In section 4.2, we considered of estimate of model error, $\langle \mathbf{e} \rangle$, to be composed of systematic and
854 random components:

$$855 \quad \langle \mathbf{e} \rangle = \langle \mathbf{e}_{\text{sys}} \rangle + \langle \mathbf{e}_{\text{ran}} \rangle \quad (8)$$

856 We argued that $\langle \mathbf{e}_{\text{ran}} \rangle$ should encompass model fluctuations and will be controlled
857 predominantly by errors in the data, although trade-offs between model variables at different
858 depths are also important. We came to identify it with the standard deviation of the mean of the
859 posterior distribution at each location and depth:

$$860 \quad \langle \mathbf{e}_{\text{ran}} \rangle = \sigma_{\bar{m}} \quad (9)$$

861 We computed $\sigma_{\bar{m}}$ by scaling the standard deviation of the posterior distribution, σ_m , inversely
862 by the square root of the number of independent models in the posterior distribution, and
863 estimated this number by considering the characteristics of the Likelihood function as suggested
864 by [Mosegaard and Tarantola \(1995\)](#). We found on average that to compute $\sigma_{\bar{m}}$ we needed to
865 scale σ_m by 1/4 – 1/5. On average, this result captures our degree of belief in the models
866 concerning the effect of non-systematic errors in the mean of the posterior. Estimates of random
867 error are designed to capture model stability and quantify the degree of fluctuation in the model
868 that results from measurement error. However, as we discuss here, systematic errors may be
869 considerably larger than random errors and random error estimates should be seen as providing a
870 lower bound on the likely errors in the resulting model.

871 The evaluation of systematic errors in the resulting model is a thornier subject than random
872 errors because it involves an assessment of the effect of assumptions and constraints imposed in
873 the inversion in the final models, and we do not know how the earth deviates from our
874 assumptions. Three of the most important effects to consider are: (1) the scaling of V_p with V_s ,
875 (2) the scaling of density (ρ) with V_s , and (3) the choice of Q in the mantle. The effect of the
876 choice of Q on the estimated model arises through the correction for physical dispersion
877 ([Kanamori and Anderson, 1977](#)), which is strongest when Q is low. The large Q of the crust
878 mitigates the effect on our model of ignorance of its exact value, but Q in the mantle is typically

879 much smaller which means that ignorance of mantle Q may have a more significant impact on
880 the estimated model. The assumptions we made about V_p , ρ , and Q are discussed in section 3.1,
881 in equations (1) and (2) and the paragraph that follows them.

882 [Shen et al. \(2013b\)](#) discussed at some length the effect of varying the V_p : V_s ratio in the
883 inversion. They introduced the crustal V_p : V_s ratio as a variable in their inversion and found two
884 important effects. First, they found that using surface wave dispersion data and receiver
885 functions truncated 10 sec after the P-phase arrival, the posterior distribution of V_p : V_s was
886 approximately uniform. This means that V_p : V_s could not be estimated with the data they used.
887 We introduce Rayleigh wave H/V measurements relative to their data set but do not believe that
888 this will influence the posterior distribution of V_p : V_s appreciably. Second, they found that the
889 choice of the V_p : V_s ratio dominantly affected their estimate of crustal thickness. Varying V_p : V_s
890 from 1.70 to 1.80, for example, changes the mean of the posterior distribution for crustal
891 thickness by about 3 km, on average. Thus, a reasonable estimate of the effect on crustal
892 thickness of variations in V_p : V_s around the value of 1.75 that we impose in the crust is about
893 ± 1.5 km. This will impact regions where receiver functions constrain crustal thickness in our
894 model and, therefore, will exclude sedimentary basins where reverberations in the receiver
895 functions typically obscure the observation of the time of the Moho phase conversion. The
896 standard deviation of the mean of crustal thickness in the posterior distribution ([Fig 13b](#), divided
897 by 4-5) is on average about 1 km across the US. Thus, the systematic error caused by V_p : V_s
898 deviating from our assumed value of 1.75 in the crust may very well be larger than random error
899 in some locations.

900 We now discuss systematic effects on the estimated models due to Q in the mantle differing from
901 our assumption of 150 and ρ in the crust differing from the relation with V_s given by equation
902 (2). The results we present here are shown for the inversion at station X57A in Hartsville, SC.
903 Results at other stations are similar but not identical.

904 Rayleigh wave phase speeds are sensitive to Q because V_s presented in the model depends on the
905 physical dispersion correction ([Kanamori and Anderson, 1977](#)). [Figure 23a](#) illustrates the effects
906 of changing Q in the mantle from 150 to both 75 and 300 using blue and green lines,
907 respectively. The effect on H/V measurements is shown in [Figure 23b](#). Halving Q from 150 to 75
908 has a larger effect than doubling Q from 150 to 300 on Rayleigh wave phase speeds and H/V

909 measurements. The affect on estimates of the mean of the posterior distribution of changing
910 mantle Q from 150 to 75 and 300 is shown in [Figure 23c](#). The effect is largely confined to the
911 mantle with much smaller effects in the crust. If mantle Q were in fact 75 rather than the 150 we
912 assumed, then the estimated Vs in the mantle would be increased by about 0.7% on average from
913 60 to 150 km depth. In contrast, if Q were actually 300 then the estimated Vs in the mantle
914 would be decreased on average by about 0.4% in the same depth range. Because much of the
915 western US probably may have a lower mantle Q than 150 and the eastern US probably has a
916 larger Q than this value (Dalton et al., 2008), model bias due to the assumed Q model is probably
917 larger in the West than in the East. The net impact is that our estimate of mantle Vs in the West
918 may be biased low by in excess of 0.5%. The Vs values we estimated in the East may be biased
919 high by this effect by a smaller value, perhaps in excess of 0.25%. The bias in the East due to
920 uncertainty in Q probably lies within the standard deviation of the mean, which we equate with
921 random error, but the bias in the West may be larger than our estimate of random error.
922 However, both in the West and in the East the bias may be spatially coherent over large areas.

923 Rayleigh wave phase speeds and H/V measurements also possess sensitivity to crustal density.
924 [Figure 24](#) presents sensitivity kernels showing the sensitivity of Rayleigh wave phase speeds and
925 H/V measurements to density and Vs perturbations. An important difference is that for phase
926 speeds the density kernel changes sign. A positive Vs perturbation in the crust will produce a
927 positive perturbation in Rayleigh wave phase speed, but a positive crustal density perturbation
928 will produce an effect on phase speed that could be positive, negative, or zero depending on
929 period and how the perturbation is distributed vertically in the crust. However, for density
930 perturbations that are focused on the top half of the crust, a positive crustal density perturbation
931 will produce a negative effect on phase speed. For H/V, the shapes of the Vs and density kernels
932 are similar and both change sign with depth. However, the largest kernel amplitudes are negative
933 and near the surface. Again, if perturbations are focused in the upper half of the crust then
934 positive perturbations in density or Vs will produce negative perturbation on H/V. Finally, it is
935 worth noting that for kernels that change sign in the crust, the effect of perturbations applied
936 across the whole crust will tend to cancel. As described in the next paragraph, we apply a
937 constant crustal density perturbation across the entire crust. Thus, the effect both on phase speeds
938 and H/V is mostly at long periods where the sign change of the kernel occurs in the mantle.

939 **Figure 23a,b** show the impact on phase speed and H/V measurements of changing crustal density
940 by 0.1 g/cm^3 across the entire crust relative to the value given by equation (2). This perturbation
941 ranges from 3% to 4% depending on depth in the crust. A positive crustal density perturbation
942 will decrease phase speed at all periods, but due to the oscillation of the sensitivity kernel in the
943 crust at short periods the impact will be experienced dominantly at intermediate periods (**Fig.**
944 **23a**). Similarly, the impact on H/V will predominantly be at longer periods (**Fig. 23b**). Bias of
945 the model, therefore, will mostly be confined to the uppermost mantle as **Figure 23c** illustrates. A
946 systematic error of density of 3%-4% across the entire crust would produce a bias in Vs of 0.6%-
947 0.8% from the Moho to about 100 km depth in the mantle, with a smaller effect in the lowermost
948 crust. The details of the bias will depend on the vertical distribution of the density error, but we
949 believe that systematic errors in the mantle of 0.5% may be common. If density errors are not
950 distributed as evenly in the crust, then a bias of crustal Vs could occur.

951 In summary, we have discussed three potential sources of systematic error here: the scaling
952 relation between Vp and Vs, the scaling relation between density and Vs, and the assumed value
953 of Q in the mantle. We believe that errors in the assumed crustal Vp:Vs ratio mostly likely will
954 bias estimates of crustal thickness. Errors of up to 1.5 km are to be expected in some places,
955 which is larger than average random error across the US (~1 km). The impact of error in the
956 assumed crustal density on estimated model Vs will depend in detail on the vertical distribution
957 of the error in density, but we show that (perhaps contrary to expectation) model bias in the
958 mantle can be appreciable. We show that a systematic error in crustal density across the entire
959 crust of 3%-4% can bias Vs in the uppermost mantle by more than 0.5%, which is larger than
960 average random error. Finally, errors in Q assumed in the mantle will also bias estimated Vs in
961 the mantle. We discuss ways in which systematic errors may be reduced in the future in section
962 6.

963 **6. Conclusions**

964 We present a 3D model of crustal and uppermost mantle Vs to a depth of about 150 km across
965 the contiguous US. The model is composed on a set of vertical 1D profiles beneath each of the
966 1816 USArray Transportable Array (TA) stations by jointly inverting Rayleigh wave dispersion,
967 receiver functions, and Rayleigh wave ellipticity (H/V) measurements. Rayleigh wave dispersion
968 curves are derived from ambient noise and earthquakes, which agree in the period band of

969 overlap. Estimates of measurement error for all data allow us to invert the different data sets
970 together. A Bayesian Monte Carlo inversion procedure provides the basis for the inversion and a
971 posterior distribution of models is constructed beneath each TA station. We summarize these
972 distributions at each location and depth with the mean, \bar{m} , and standard deviation, σ_m , and we
973 then interpolate these depth dependent statistics onto a $0.25^\circ \times 0.25^\circ$ across the US by simple
974 kriging. The resulting depth dependent interpolated pair (\bar{m}, σ_m) as a function of depth across
975 the US forms the 3D model.

976 We argue here that the standard deviation of the posterior distribution, σ_m , is not an ideal
977 estimate of absolute model uncertainty, but it provides useful information about relative
978 uncertainty. It is too large to represent random error and does not include an estimate of
979 systematic error. A better estimate of random error of the model is the standard deviation of the
980 mean of the posterior distribution, $\sigma_{\bar{m}}$. This statistic provides a better estimate of the fluctuations
981 observed in the 3D model and more accurately reflects the impact on model variables of data
982 uncertainties. Using two different methods, we demonstrate that on average $\sigma_{\bar{m}}$ can be estimated
983 by scaling σ_m by about 0.2 – 0.25. Doing so, we find that random model error in Vs averages
984 about 0.2% in the mid-crust and 0.4% in the mantle, but these error grow near Moho and the free
985 surface.

986 A great many structural features are determined reliably in the 3D model. We do not focus here
987 on interpreting these features or even pointing them out systematically, but provide views of the
988 model across the continent. We do highlight three prominent features of the model beneath and
989 across the Snake River Plain, the Reelfoot Rift, and the Appalachian Mountains. The observation
990 of three low velocity features beneath the Appalachians in western Virginia, northern Georgia,
991 and New England are new to the best of our knowledge. We believe that the explication of the
992 model will require a number of papers dedicated to individual structural features, such as the
993 paper on the Mid-Continent Rift by [Shen et al. \(2013c\)](#).

994 Although we discuss random error at some length, systematic error is probably larger and of
995 greater concern because it is more difficult to estimate reliably. Systematic error results from the
996 deviation of the constraints and assumptions that we impose in the inversion from the real earth.
997 Our discussion of systematic error aims to quantify the probable magnitude and nature of several

998 important types of error. In so doing, it provides the basis to identify fruitful directions to
999 advance the model as part of future research.

1000 We discuss three potential sources of systematic error here: deviation of crustal V_p/V_s from
1001 1.75, the introduction of a crustal density perturbation relative to the assumed ρ/V_s scaling
1002 relation given by equation (2), and deviation of mantle Q from the value of 150 assumed in our
1003 inversion. We find that systematic errors are most likely to accrue to estimates of crustal
1004 thickness and V_s in the mantle. Even crustal density errors, if they persevere throughout the
1005 crust, will manifest dominantly as bias of V_s in the mantle rather than in the crust, although bias
1006 of crustal V_s is also possible if density error is confined to shallow depths. Such systematic
1007 errors arising from several separate sources may constructively or destructively interfere with
1008 one another, but errors of 0.5%-1% in V_s at upper mantle depths are probably not unlikely,
1009 which is larger than average random error. Such errors may be coherent over large regions (e.g.,
1010 mantle Q in the West may be consistently lower than 150 and in the East consistently higher) or
1011 may vary rapidly laterally (e.g., geological variations affecting crustal density).

1012 Future research is called for that will beat down systematic error by introducing better
1013 information in the inversion to improve constraints on V_p , density, and mantle Q . For example,
1014 V_p/V_s can be better constrained by introducing longer P-to-S receiver functions into the analysis
1015 (e.g., [Zhu and Kanamori, 2000](#); [Chen and Niu, 2013](#)). S-to-P receiver functions would also
1016 provide new and valuable constraints (e.g., [Hansen and Dueker, 2009](#); [Lekic et al., 2014](#);
1017 [Fischer, 2015](#)). In addition, a more accurate density-to- V_s scaling relationship may arise by
1018 applying gravity (e.g., [Maceira and Ammon, 2009](#)) and surface wave local amplification data in
1019 the inversion simultaneously (e.g., [Eddy and Ekstrom, 2014](#); [Lin et al., 2012a](#)). Moreover, there
1020 are many other fruitful directions to improve and extend the model presented here in future work.
1021 We mention only three. First, it will be important to include the introduction of Love waves,
1022 which will provide information about radial anisotropy (e.g., [Moschetti et al., 2010a,b](#); [Xie et al.,](#)
1023 [2013](#)). Second, it is also important to perform the simultaneous interpretation of Rayleigh wave
1024 azimuthal anisotropy (e.g., [Lin et al., 2011](#)) with other data in order to constrain the full elasticity
1025 tensor (e.g., [Xie et al., 2015](#)). Third, the increasing availability of dense (large N) arrays
1026 improves the ability to constrain discontinuities in the interior of the crust, which are not
1027 included in the present study (e.g., [Deng et al., 2015](#)).

1028
1029
1030
1031
1032
1033
1034
1035
1036
1037
1038
1039
1040
1041
1042
1043
1044
1045
1046
1047
1048
1049
1050

Acknowledgments. The authors thank Fan-Chi Lin and Vera Schulte-Pelkum for valuable conversations and Lili Feng for help in preparing some of the ambient noise measurements. The facilities of the IRIS Data Management System, and specifically the IRIS Data Management Center, were used to access the waveform and metadata required in this study. The IRIS DMS is funded through the National Science Foundation and specifically the GEO Directorate through the Instrumentation and Facilities Program of the National Science Foundation under Cooperative Agreement EAR-0552316. This work was supported by NSF grant EAR-1252085 at the University of Colorado at Boulder. This work utilized the Janus supercomputer, which is supported by the National Science Foundation (award number CNS-0821794) and the University of Colorado Boulder. The Janus supercomputer is a joint effort of the University of Colorado Boulder, the University of Colorado Denver and the National Center for Atmospheric Research.

1051 **Figure 1.** Area of study, geographic and tectonic features, and station coverage. (a) Map of the
1052 contiguous US with major physiographic boundaries (Fenneman and Johnson, 1946) shown with
1053 red lines. Black abbreviations note the names of tectonic regions, blue abbreviations identify two
1054 rifts, red symbols denote sedimentary basins, and the black dashed line, divided by the
1055 Mississippi Embayment, marks the location of the Grenville Front (GF). Location names are
1056 identified in Table 1. (b) Stations used in this study are shown as gray circles. Red stars mark the
1057 locations of the six example stations whose data and inversion results are shown later in the
1058 paper: Z21A near Winston, NM; Q22A near Crested Butte, CO; C23A near Lambert, MT; 239A
1059 near Gary, TX; R43A near Red Bud, IL; and X57A near Hartsville, SC.

1060
1061 **Figure 2.** Rayleigh wave group and phase speed maps. (a-b) Group velocity maps at 8 and 28 sec
1062 produced from ambient noise straight-ray tomography, respectively. (c-d) Phase velocity maps at
1063 8 and 28 sec produced from ambient noise eikonal tomography, respectively. (e-f) Phase velocity
1064 maps at 40 and 60 sec produced from earthquake Helmholtz tomography, respectively.

1065
1066 **Figure 3.** Rayleigh wave H/V ratio measurements at 28 and 60 sec, respectively, presented at the
1067 stations where they are observed.

1068
1069 **Figure 4.** Estimated measurement uncertainties as a function of period averaged across the US.
1070 (a) Raleigh wave group and phase speed uncertainties are presented as a function of period.
1071 Group speed uncertainties are derived from ambient noise tomography between 8 and 40 sec
1072 period, and phase speed uncertainties are from ambient noise at periods from 8 and 26 sec, a
1073 combination of ambient noise and earthquake tomography from 28 to 36 sec period, and
1074 earthquake tomography from 40 to 90 sec period. (b) Uncertainty in Rayleigh wave H/V
1075 measurements presented as a function of period from 20 to 90 sec. Dispersion uncertainties
1076 minimize around 20 sec period and grow toward shorter and longer periods. Uncertainties in H/V
1077 measurements grow approximately linearly with period.

1078
1079 **Figure 5.** Period averaged measurement uncertainty as a function of spatial location. (a) Phase
1080 speed uncertainties averaged from 8 to 90 sec period. (b) Group speed uncertainty averaged from
1081 8 to 40 sec period. (c) Raleigh wave H/V measurement uncertainty averaged from 20 to 90 sec
1082 period. Uncertainties in all observables are fairly homogeneous spatially, but grow near the
1083 periphery of the array.

1084
1085 **Figure 6.** Example data from the six locations (a-f) identified with red stars in Fig. 1. For each
1086 location three vertically-arrayed panels show the three data types: (Top Panel) the receiver
1087 function is shown with a grey corridor (1 standard deviation error around the mean at each time),
1088 (Middle Panel) Rayleigh wave H/V measurements are shown with 1 standard deviation error
1089 bars, and (Bottom Panel) Rayleigh wave phase and group velocities (phase speeds are faster than
1090 group speeds at each period here) are presented with 1 standard deviation error bars. Solid lines
1091 in each panel are local predictions from the best-fitting model in the posterior distribution
1092 derived from the joint inversion of all three data sets.

1093
1094 **Figure 7.** Example comparison of prior and posterior distributions in the Bayesian Monte Carlo
1095 inversion for three model characteristics at two stations: (a-c) Z21A (Winston NM) and (d-f)
1096 C23A (Lambert MT). Grey histograms are the prior distribution, white histograms are the

1097 posterior distribution using surface wave dispersion data alone (Rayleigh wave group and phase
1098 speed measurements), and red histograms are the posterior distributions for the joint inversion of
1099 surface wave dispersion data, receiver functions, and Rayleigh wave H/V measurements at each
1100 station. Top Row: shear wave speed averaged between 0 and 5 km depth, Middle Row: shear
1101 wave speed directly above the Moho, Bottom Row: crustal thickness (local elevation + depth of
1102 Moho below the geoid). If the red distribution is narrower and more peaked than the white
1103 distribution, then data other than surface wave dispersion constrain that model variable. For
1104 example, the receiver function at station Z21A (Fig. 6a) improves the crustal thickness estimate
1105 but not at station C23A where surface sediments obscure the Moho phase conversion in the
1106 receiver function (Fig. 6c).
1107

1108 **Figure 8.** Examples of the depth-dependence of the width of the posterior distribution from the
1109 joint inversion of all data at the six locations identified with red stars in Fig. 1. The full width of
1110 the posterior distribution for shear wave speed is shown with the grey shaded corridor. The mean
1111 of the distribution is identified with a solid black line and the one standard deviation contours are
1112 shown with red lines. For each location, the model is presented in two panels: an upper panel
1113 shows the model to 8 km depth in order to highlight sedimentary structure (shear velocity,
1114 thickness) and a lower panel shows the model to 150 km depth. The standard deviation of the
1115 posterior distribution is largest near the Moho and below 120 km depth.
1116

1117 **Figure 9.** Geographic variation in the fit to the data by the best-fitting model that results from the
1118 joint inversion of all data, presented at each station. Fit to (a) Rayleigh wave phase speed data
1119 averaged from 8 to 90 sec period, (b) Rayleigh wave group speed data averaged from 8 to 40 sec
1120 period, (c) Rayleigh wave H/V measurements averaged from 20 to 90 sec period, and (d)
1121 receiver function data averaged from 0 to 10 sec after the arrival of the P-wave. Fits are defined
1122 as the square root of the reduced χ^2 misfit (eqn. (6)).
1123

1124 **Figure 10.** (a) The definition of the three regions in which regional averages and variability are
1125 computed: (red circles) “Western Region” west of the Rocky Mountain front, (blue circles)
1126 “Continental Core Region” between the Rocky Mountain front and the Greenville front (dashed
1127 line), and (green circles) the “Eastern Region” east and south of the Greenville front. (b) Shear
1128 wave speed as a function of depth averaged within each of the regions, color-coded in
1129 accordance with the regional colors in (a). (c) Spatial variations in shear wave speeds across each
1130 region presented with colors as in (b), defined as the standard deviation around the mean at each
1131 depth. The dashed black line is the estimate of the standard deviation in the mean of the posterior
1132 distribution averaged across the US, which we interpret as the average model error due to
1133 random processes.
1134

1135 **Figure 11.** (a) Black line: standard deviation of the posterior distribution (σ_m) averaged across
1136 the entire US. Red line: estimate of the standard deviation of the mean ($\sigma_{\bar{m}}$) of the posterior
1137 distribution averaged across the US (computed by scaling σ_m by 0.2), which we interpret as the
1138 average model error due to random processes (same as dashed line in Fig. 10c). (b) Variation in
1139 V_s (solid black line: the mean of the posterior distribution) along the Snake River Plain (profile
1140 X2, Fig. 22). Dashed lines mark $\pm 1 \sigma_m$ and the grey corridor marks $\pm 1 \sigma_{\bar{m}}$. (c) Comparison of
1141 (black line) σ_m and (red line) $\sigma_{\bar{m}}$ for the inversion at station X57A (Hartsville, SC). $\sigma_{\bar{m}}$ is

1142 computed by brute force in which numerous posterior distributions are computed at this station
1143 and the mean of the posterior distribution are computed from them.

1144
1145 **Figure 12.** Various crustal features. (a) Mean of the posterior distribution of the average shear
1146 wave speed averaged in the top 5 km below the free surface using surface wave dispersion
1147 measurements alone. (b) Same as (a), but the inversion uses all data (including receiver functions
1148 and Rayleigh wave H/V measurements). Shallow structure is modified predominantly by the
1149 introduction of the H/V data. (c) Mean of the posterior distribution of the shear wave speed in the
1150 middle crust averaged within 4 km of the mid-point between the free surface and Moho, taken
1151 from the inversion using all data. (c) Mean of the posterior distribution of the shear wave speed
1152 in the lower crust averaged within 3 km of Moho in the crust, taken from the inversion using all
1153 data.

1154
1155 **Figure 13.** Crustal thickness. (a) Mean of the posterior distribution of crustal thickness (distance
1156 from the free surface to Moho) taken from the inversion using all data. (b) Standard deviation of
1157 the posterior distribution (σ_m) of crustal thickness from the inversion using all data.

1158
1159 **Figure 14.** (a) The jump in Vs across Moho presented as the difference in Vs directly below and
1160 above Moho, taken from the mean of the posterior distribution at each depth and location. (b)
1161 The standard deviation of the difference between the shear wave speed below and above Moho
1162 computed using all models in the posterior distribution at each point.

1163
1164 **Figure 15.** The standard deviation of the posterior distribution, σ_m , for Vs at different depths in
1165 the crust: (a) averaged over the top 5 km, (b) averaged in the middle crust within 4 km of the
1166 mid-point between the free surface and Moho, and (c) averaged in the lower crust within 3 km of
1167 Moho. In the crust, σ_m is largest near the free surface and Moho.

1168
1169 **Figure 16.** (a) Histogram of the difference between the local standard deviation of the posterior
1170 distribution (σ_m) of crustal thickness determined in the inversion using all data (**Fig. 13b**), std
1171 dev (All), and the standard deviation based on surface wave data alone, std dev (SW), at the
1172 same location. (b) Plot of std dev (All) versus the jump across Moho (**Fig. 14a**) at the same
1173 location.

1174
1175 **Figure 17.** A Low Velocity Zone (LVZ) in the shallow mantle? Plot of the difference between Vs
1176 at the top of the mantle directly below Moho and Vs 20 km below Moho, using the mean of the
1177 posterior distribution at each location. Warm colors indicate a negative vertical gradient
1178 indicative of a shallow LVZ and cool colors indicate a positive vertical gradient in the uppermost
1179 mantle indicative of no LVZ.

1180
1181 **Figure 18.** Mantle shear wave speeds at three depths, presented as the mean of the posterior
1182 distribution at each location: (a) 70 km depth, (b) 90 km depth, and (c) 120 km depth. Vs values
1183 are averaged vertically within 5 km of each stated depth.

1184

1185 **Figure 19.** The standard deviation of the posterior distribution, σ_m , for Vs at different depths in
1186 the mantle within ± 5 km of (d) 70 km, (e) 90 km, and (f) 120 km, respectively. This quantity is
1187 generally larger in the mantle than in the crust and grows particularly below 100 km depth.
1188

1189 **Figure 20.** The location of the vertical transects through the 3D model. Long east-west transects
1190 A-A', B-B', C-C', and D-D' are presented in **Fig. 21**. The shorter pairs of crossing transects, X1-
1191 X2, Y1-Y2, Z1-Z2, are shown in **Fig. 22**.
1192

1193 **Figure 21.** Four east-west oriented vertical transects through the 3D model, with locations
1194 identified in **Fig. 20**, defined as the mean of the posterior distribution of Vs at each location and
1195 depth. Each transect is part of a pair of depth profiles with different vertical exaggerations: one
1196 for the crust (top 60 km) and the other for the uppermost mantle (30 -150 km). Depth is defined
1197 as the distance below the free surface, absolute crustal velocities are presented according to the
1198 inset legend, crustal thickness is identified with a bold solid black line, isolines in the crust and
1199 mantle are placed at intervals of 0.2 km/s and 3%, respectively, and mantle velocities are
1200 presented as perturbations relative to 4.4 km/s in percent. Local surface topography is also
1201 indicated, as are abbreviated names of selected structural and geographic features, most of which
1202 are identified in **Table 1** with the exception of NRM (northern Rocky Mountains), NBR, and
1203 SBR (northern and southern Basin and Range, respectively).
1204

1205 **Figure 22.** Three pairs of shorter crossing vertical transects with locations identified in **Fig. 20**.
1206 Profiles X1 and X2 are oriented along and across the Snake River Plain, profiles Y1 and Y2
1207 target the Reelfoot Rift, and profiles Z1 and Z2 target the Appalachians, crossing in western
1208 Virginia. Definitions and formatting are similar to **Fig. 21** but there are differences. Crustal
1209 velocities are presented on the same absolute scale as in **Fig. 21** and mantle velocities are
1210 perturbations relative to a constant value, but the mantle reference for profiles X1 and X2 is 4.3
1211 km/s and the reference for profiles Y1, Y2, Z1, and Z2 is 4.55 km/s. The color scale for profiles
1212 X1 and X2 ranges between $\pm 8\%$, as in **Fig. 21**, but the scale for the other profiles ranges only
1213 between $\pm 4\%$. Abbreviations are identified in **Table 1** with the exception of SAM (southern
1214 Appalachian Mountains).
1215

1216 **Figure 23.** Simulated effects of systematic errors evaluated by: (blue lines) changing Q from 150
1217 to 75 in the mantle, (green lines), changing Q from 150 to 300 in the mantle, and (red line)s
1218 increasing density by 0.1 g/cm^3 throughout the crystalline crust. (a) Effect on Rayleigh wave
1219 phase velocity as a function of period. (b) Same as (a), but for the effect on Rayleigh wave
1220 ellipticity, H/V. (c) The effect on the estimated mean of the posterior distribution of Vs. All
1221 results are presented by perturbing around the mean of the posterior distribution for station X57A
1222 (Hartsville, SC).
1223

1224 **Figure 24.** Sensitivity of (a) Rayleigh wave phase speed and (b) ellipticity (H/V) to perturbations
1225 in (red lines) Vs and (green lines) density at periods of 20 sec and 50 sec.
1226
1227

1228 Allison, C.M., Porter, R.C., Fouch, M.J. and Semken, S., Seismic evidence for lithospheric
1229 modification beneath the Mojave Neovolcanic Province, Southern California. *Geophysical*
1230 *Research Letters*, 40(19), pp.5119-5124, 2013.

1231

1232 Agrawal, M., J. Pulliam, M. K. Sen, and H. Gurrola, Lithospheric structure of the Texas-Gulf of
1233 Mexico passive margin from surface wave dispersion and migrated Ps receiver functions,
1234 *Geochem. Geophys. Geosyst.*, **16**, 2221–2239, doi:10.1002/2015GC005803, 2015.

1235

1236 Bailey, I.W., Miller, M.S., Liu, K. and Levander, A., Vs and density structure beneath the
1237 Colorado Plateau constrained by gravity anomalies and joint inversions of receiver function and
1238 phase velocity data. *Journal of Geophysical Research: Solid Earth* (1978–2012), 117(B2), 2012.

1239

1240 Barmin, M.P., Ritzwoller, M.H. and Levshin, A.L., A Fast and Reliable Method for Surface
1241 Wave Tomography. *Pure and Applied Geophysics*, 158(8), pp.1351-1375, 2011.

1242

1243 Benoit, M. H., C. Ebinger, and M. Crampton, Orogenic bending around a rigid Proterozoic
1244 magmatic rift beneath the Central Appalachian Mountains, *Earth Planet. Sci. Lett.*, **402**, 197–
1245 208, 2014.

1246

1247 Bensen, G.D., M.H. Ritzwoller, M.P. Barmin, A.L. Levshin, F. Lin, M.P. Moschetti, N.M.
1248 Shapiro, and Y. Yang, Processing seismic ambient noise data to obtain reliable broad-band
1249 surface wave dispersion measurements, *Geophys. J. Int.*, 169, 1239-1260, doi: 10.1111/j.1365-
1250 246X.2007.03374.x, 2007.

1251

1252 Bensen, G.D., M.H. Ritzwoller, and Y. Yang, A 3D shear velocity model of the crust and
1253 uppermost mantle beneath the United States from ambient seismic noise, *Geophys. J. Int.*,
1254 177(3), 1177-1196, 2009.

1255

1256 Bodin, T., Sambridge, M., Tkalčić, H., Arroucau, P., Gallagher, K. and Rawlinson, N.,
1257 Transdimensional inversion of receiver functions and surface wave dispersion. *Journal of*
1258 *Geophysical Research: Solid Earth* (1978–2012), 117(B2), 2012.

1259

1260 Boore, D.M. and M.N. Toksoz, Rayleigh wave particle motion and crustal structure, *Bull. Seism.*
1261 *Soc. Am.*, 59(1), 331-346, 1969.

1262

1263 Boué, P., Roux, P., Campillo, M. and Briand, X., Phase velocity tomography of surface waves
1264 using ambient noise cross correlation and array processing. *Journal of Geophysical Research:*
1265 *Solid Earth*, 119(1), pp.519-529, 2014.

1266

1267 Brocher, T.M., Empirical relations between elastic wave speeds and density in the Earth's crust,
1268 *Bull. Seism. Soc. Am.*, 95, 2081-2092, doi:10.1785.0120050077, 2005.

1269

1270 Calkins, J.A., Zandt, G., Girardi, J., Dueker, K., Gehrels, G.E. and Ducea, M.N.,
1271 Characterization of the crust of the Coast Mountains Batholith, British Columbia, from P to S
1272 converted seismic waves and petrologic modeling. *Earth and Planetary Science Letters*, 289(1),
1273 pp.145-155, 2010.

1274
1275 Calkins, J.A., Abers, G.A., Ekstrom, G., Creager, K.C. and Rondenay, S., Shallow structure of
1276 the Cascadia subduction zone beneath western Washington from spectral ambient noise
1277 correlation. *Journal of Geophysical Research: Solid Earth* (1978–2012), 116(B7), 2011.
1278
1279 Chang, S.J., Baag, C.E. and Langston, C.A. Joint analysis of teleseismic receiver functions and
1280 surface wave dispersion using the genetic algorithm. *Bulletin of the Seismological Society of
1281 America*, 94(2), pp.691-704, 2004.
1282
1283 Chen, Y. and Niu, F., Ray-parameter based stacking and enhanced pre-conditioning for stable
1284 inversion of receiver function data. *Geophysical Journal International*, 204(3), doi:
1285 10.1093/gji/ggt179, 2013.
1286
1287 Chu, R., W. Leng, D.V. Helmberger, and M. Gurnis, Hidden hotspot track beneath the eastern
1288 United States, *Nature Geoscience*, doi:10.1038/NGEO1949, 2013.
1289
1290 Chu, R. and Helmberger, D., Lithospheric waveguide beneath the Midwestern United States;
1291 massive low-velocity zone in the lower crust. *Geochemistry, Geophysics, Geosystems*, 15(4),
1292 pp.1348-1362, 2014.
1293
1294 Dalton, C.A., Ekström, G. and Dziewoński, A.M., The global attenuation structure of the upper
1295 mantle. *Journal of Geophysical Research: Solid Earth* (1978–2012), 113(B9), 2008.
1296
1297 Delorey, A.A. and Vidale, J.E., Basin shear-wave velocities beneath Seattle, Washington, from
1298 noise-correlation Rayleigh waves. *Bulletin of the Seismological Society of America*, 101(5),
1299 pp.2162-2175, 2011.
1300
1301 Deng, Y., W. Shen, T. Xu, and M.H. Ritzwoller, Crustal layering in northeastern Tibet: A case
1302 study based on joint inversion of receiver functions and surface wave dispersion, *Geophys. J.
1303 Int.*, 203(1), 692-706, 2015.
1304
1305 Dziewonski, A.M. and Anderson, D.L., Preliminary reference Earth model. *Physics of the earth
1306 and planetary interiors*, 25(4), pp.297-356, 1981.
1307
1308 Eagar, K. C., M. J. Fouch, D. E. James, and R. W. Carlson, Crustal structure beneath the High
1309 Lava Plains of eastern Oregon and surrounding regions from receiver function analysis, *J.
1310 Geophys. Res.*, **116**, B02313, doi:10.1029/2010JB007795, 2011.
1311
1312 Eddy, C. L., & Ekström, G., Local amplification of Rayleigh waves in the continental United
1313 States observed on the USArray. *Earth and Planetary Science Letters*, 402, 50-57, 2014.
1314
1315 Ekström, G., Love and Rayleigh phase-velocity maps, 5–40 s, of the western and central USA
1316 from USArray data. *Earth and Planetary Science Letters*, 402, pp.42-49, 2014.
1317
1318 Fischer, K.M. Crust and Lithospheric Structure - Seismological Constraints on the Lithosphere-
1319 Asthenosphere Boundary, *Treatise on Geophysics*, 587-612, 2015.

1320
1321 Frassetto, A. M., G. Zandt, H. Gilbert, T. J. Owens, and C. H. Jones, Structure of the Sierra
1322 Nevada from receiver functions and implications for lithospheric foundering, *Geosphere*, 7(4),
1323 898–921, 2011.
1324
1325 Fu, Y.V. and Li, A., Crustal shear wave velocity and radial anisotropy beneath the Rio Grande
1326 rift from ambient noise tomography. *Journal of Geophysical Research: Solid Earth*, 120(2),
1327 pp.1005-1019, 2015.
1328
1329 Gaité, B., Iglesias, A., Villaseñor, A., Herraiz, M. and Pacheco, J.F., Crustal structure of Mexico
1330 and surrounding regions from seismic ambient noise tomography. *Geophysical Journal*
1331 *International*, 188(3), pp.1413-1424, 2012.
1332
1333 Gao, H., Humphreys, E.D., Yao, H. and van der Hilst, R.D., Crust and lithosphere structure of
1334 the northwestern US with ambient noise tomography: Terrane accretion and Cascade arc
1335 development. *Earth and Planetary Science Letters*, 304(1), pp.202-211, 2011.
1336
1337 Gao, H. and Shen, Y., Validation of Shear-Wave Velocity Models of the Pacific
1338 Northwest. *Bulletin of the Seismological Society of America*, 102(6), pp.2611-2621, 2012.
1339
1340 Gao, H., Crustal seismic structure beneath the source area of the Columbia River flood basalt:
1341 Bifurcation of the Moho driven by lithosphere delamination, *Geophys. Res. Lett.*,
1342 doi:10.1002/2015GL066625, 2015.
1343
1344 Gashawbeza, E.M., Klemperer, S.L., Wilson, C.K., and Miller, E.L., Nature of the crust beneath
1345 northwest Basin and Range province from teleseismic receiver function data, *Journal of*
1346 *Geophysical Research*, 113, B10308, doi: 10.1029/2007JB005306, 2008.
1347
1348 Gilbert, H. (2012), Crustal structure and signatures of recent tectonism as influenced by ancient
1349 terranes in the western United States, *Geosphere*, 8(1), 141–157.
1350
1351 Hacker, B.R., Abers, G.A. and Peacock, S.M., Subduction factory 1. Theoretical mineralogy,
1352 densities, seismic wave speeds, and H₂O contents. *Journal of Geophysical Research: Solid*
1353 *Earth (1978–2012)*, 108(B1), 2003.
1354
1355 Hansen, S., and K. Dueker, P- and S-wave receiver function images of crustal imbrication
1356 beneath the Cheyenne Belt in southeast Wyoming, *Bull. Seismol. Soc. Am.*, 99(3), 1953–1961,
1357 2009.
1358
1359 Hansen, S.M., Dueker, K.G., Stachnik, J.C., Aster, R.C. and Karlstrom, K.E., A rootless
1360 Rockies—Support and lithospheric structure of the Colorado Rocky Mountains inferred from
1361 CREST and TA seismic data. *Geochemistry, Geophysics, Geosystems*, 14(8), pp.2670-2695,
1362 2013.
1363
1364 Hopper, E., Ford, H.A., Fischer, K.M., Lekic, V., Fouch, M.J., The lithosphere–asthenosphere
1365 boundary and the tectonic and magmatic history of the north-western United States. *Earth*

1366 *Planet. Sci. Lett.*, 402, 69–81, 2014.
1367
1368 Houston, R.S., Duebendorfer, E.M., Karlstrom, K.E. and Premo, W.R., A review of the geology
1369 and structure of the Cheyenne belt and Proterozoic rocks of southern Wyoming. *Geological*
1370 *Society of America Special Papers*, 235, pp.1-12, 1989.
1371
1372 Jin, G. and Gaherty, J.B. Surface wave phase-velocity tomography based on multichannel cross-
1373 correlation. *Geophysical Journal International*, 201(3), pp.1383-1398, 2015.
1374
1375 Jones, C. H., and R. A. Phinney, Seismic structure of the lithosphere from teleseismic converted
1376 arrivals observed at small arrays in the southern Sierra Nevada and vicinity, California, J.
1377 *Geophys. Res.*, 103(B5), 10,065–10,090, doi:10.1029/97JB03540, 1998.
1378
1379 Julia, J., Ammon, C.J., Herrmann, R.B. and Correig, A.M., Joint inversion of receiver function
1380 and surface wave dispersion observations. *Geophysical Journal International*, 143(1), pp.99-112,
1381 2000.
1382
1383 Kanamori, H. and D. Anderson, Importance of physical dispersion in surface wave and free
1384 oscillation problems : Review, *Revs. Geophys. Space Phys.*, 15(1):105-112, 1977.
1385
1386 Kang, D., W. Shen, J. Ning, and M.H. Ritzwoller, Seismic evidence for lithospheric modification
1387 associated with intra-continental volcanism in Northeastern China, *Geophys. J. Int.*, 204(1), 215-
1388 235, 2016.
1389
1390 Kao, H., Y. Behr, C. Currie, R. Hyndman, J. Townend, F.-C. Lin, M.H. Ritzwoller, S.-J. Shan,
1391 and J. He, Ambient seismic noise tomography of Canada and adjacent regions: Part I. Crustal
1392 structures, *J. Geophys. Res.*, 118, 5865-5887, doi:10.1002/2013JB010535, 2013.
1393
1394 Last, R.J., Nyblade, A.A., Langston, C.A. and Owens, T.J. Crustal structure of the East African
1395 Plateau from receiver functions and Rayleigh wave phase velocities. *Journal of Geophysical*
1396 *Research: Solid Earth* (1978–2012), 102(B11), pp.24469-24483, 1997.
1397
1398 Lawrence, J.F. and Wiens, D.A. Combined receiver-function and surface wave phase-velocity
1399 inversion using a niching genetic algorithm: application to Patagonia. *Bulletin of the*
1400 *Seismological Society of America*, 94(3), pp.977-987, 2004.
1401
1402 Lebedev, S., Adam, J.M.C. and Meier, T. Mapping the Moho with seismic surface waves: a
1403 review, resolution analysis, and recommended inversion strategies. *Tectonophysics*, 609, 377-
1404 394, 2013.
1405
1406 Lekić, Vedran, Fischer, Karen M. Contrasting lithospheric signatures across the western United
1407 States revealed by Sp receiver functions, *Earth and Planetary Science Letters*, 402, 90-98, 2014.
1408
1409 Levander, A., and M. S. Miller, Evolutionary aspects of lithosphere discontinuity structure in the
1410 western US, *Geochem. Geophys. Geosyst.*, **13**, Q0AK07, doi:10.1029/2012GC004056, 2012.
1411

1412 Levander, A., B. Schmandt, M. S. Miller, K. Liu, K. E. Karlstrom, R. S. Crow, C.-T. Lee, and E.
1413 D. Humphreys, Continuing Colorado plateau uplift by delamination-style convective lithospheric
1414 downwelling, *Nature*, **472**(7344), 461–465, 2011.

1415
1416 Levshin, A.L. and M.H. Ritzwoller, Automated detection, extraction, and measurement of
1417 regional surface waves, *Pure Appl Geophys*, 158(8), 1531 - 1545, 2001.

1418
1419 Li, P. and Lin, G., Adaptive ambient noise tomography and its application to the Garlock Fault,
1420 southern California. *Geophysical Journal International*, p.ggu073, 2014.

1421
1422 Liang, C. and Langston, C.A., Ambient seismic noise tomography and structure of eastern North
1423 America. *Journal of Geophysical Research: Solid Earth* (1978–2012), 113(B3), 2008.

1424
1425 Liang, C. and Langston, C.A., Three-dimensional crustal structure of eastern North America
1426 extracted from ambient noise. *Journal of Geophysical Research: Solid Earth* (1978–
1427 2012), 114(B3), 2009.

1428
1429 Ligorria, J. P., and C. J. Ammon, Iterative deconvolution and receiver-function estimation,
1430 Bulletin of the Seismological Society of America, 89(5), 1395-1400, 1999.

1431 Lin, F., M.P. Moschetti, and M.H. Ritzwoller, Surface wave tomography of the western United
1432 States from ambient seismic noise: Rayleigh and Love wave phase velocity maps, *Geophys. J.*
1433 *Int.*, doi:10.1111/j1365-246X.2008.03720.x, 2008.

1434
1435 Lin, F.-C., M.H. Ritzwoller, and R. Snieder, Eikonal Tomography: Surface wave tomography by
1436 phase-front tracking across a regional broad-band seismic array, *Geophys. J. Int.*, 177(3), 1091-
1437 1110, 2009.

1438
1439 Lin, F.C. and M.H. Ritzwoller, Helmholtz surface wave tomography for isotropic and
1440 azimuthally anisotropic structure, *Geophys. J. Int.*, 186, 1104-1120, doi:10.1111/j.1365-
1441 246X.2011.05070.x, 2011.

1442
1443 Lin, F.C., M.H. Ritzwoller, Y. Yang, M.P. Moschetti, and M.J. Fouch, Complex and variable
1444 crustal and uppermost mantle seismic anisotropy in the western United States , *Nature*
1445 *Geoscience*, Vol 4, Issue 1, 55-61, Jan 2011.

1446
1447 Lin, F.-C., V. Tsai, and M.H. Ritzwoller, The local amplification of surface waves: A new
1448 observable to constrain elastic velocities, density, and anelastic attenuation, *J. Geophys. Res.*,
1449 117, B06302, doi:10.1029/2012JB009208, 2012a.

1450
1451 Lin, F. C., B. Schmandt, and V. C. Tsai, Joint inversion of Rayleigh wave phase velocity and
1452 ellipticity using USArray: Constraining velocity and density structure in the upper crust,
1453 *Geophys. Res. Lett.*, **39**, L12303, doi:10.1029/2012GL052196, 2012b.

1454
1455 Lin, F. C., V. C. Tsai, and B. Schmandt, 3-D crustal structure of the western United States:
1456 Application of Rayleigh-wave ellipticity extracted from noise cross-correlations, *Geophys. J.*
1457 *Int.*, **198**, 656–670, 2014.

1458
1459 Lin, F.-C. and B. Schmandt, Upper crustal azimuthal anisotropy across the contiguous US
1460 determined by Rayleigh wave ellipticity, *Geophys. Res. Letts.*, 41(23), 8301-8307, 2014.
1461
1462 Liu, K., Levander, A., Zhai, Y., Porritt, R.W. and Allen, R.M., Asthenospheric flow and
1463 lithospheric evolution near the Mendocino Triple Junction. *Earth and Planetary Science*
1464 *Letters*, 323, pp.60-71, 2012.
1465
1466 Liu Q-Y, Li Y, J.H. Chen, Van Der Hilst, R.D., Guo B., Wang J., Qi S.H. and Li S.C., Joint
1467 inversion of receiver function and ambient noise based on Bayesian theory. *Chinese Journal of*
1468 *Geophysics*, 53(6), pp.961-972, 2010.
1469
1470 Ma, S., Prieto, G.A. and Beroza, G.C., Testing community velocity models for southern
1471 California using the ambient seismic field. *Bulletin of the Seismological Society of*
1472 *America*, 98(6), pp.2694-2714, 2008.
1473
1474 Maceira, M. and Ammon, C.J., Joint inversion of surface wave velocity and gravity observations
1475 and its application to central Asian basins shear velocity structure. *Journal of Geophysical*
1476 *Research: Solid Earth (1978–2012)*, 114(B2), 2009.
1477
1478 Mooney, W.D. and Kaban, M.K., The North American upper mantle: Density, composition, and
1479 evolution. *Journal of Geophysical Research: Solid Earth (1978–2012)*, 115(B12), 2010.
1480
1481 Mordret, A., Shapiro, N.M., Singh, S., Roux, P., Montagner, J.P. and Barkved, O. Azimuthal
1482 anisotropy at Valhall: The Helmholtz equation approach. *Geophysical Research Letters*, 40(11),
1483 pp.2636-2641, 2013.
1484
1485 Moschetti, M.P., M.H. Ritzwoller, and N.M. Shapiro, Surface wave tomography of the western
1486 United States from ambient seismic noise: Rayleigh wave group velocity maps, *Geochem.,*
1487 *Geophys., Geosys.*, 8, Q08010, doi:10.1029/2007GC001655, 2007.
1488
1489 Moschetti, M.P., M.H. Ritzwoller, and F.C. Lin, Seismic evidence for widespread crustal
1490 deformation caused by extension in the western USA, *Nature*, 464, Number 7290, 885-889, 8
1491 April 2010a.
1492
1493 Moschetti, M.P., M.H. Ritzwoller, F.C. Lin, and Y. Yang, Crustal shear velocity structure of the
1494 western US inferred from ambient noise and earthquake data, *J. Geophys. Res.*, 115, B10306,
1495 doi:10.1029/2010JB007448, 2010b.
1496
1497 Mosegaard, K., and A. Tarantola, Monte Carlo sampling of solutions to inverse problems, *J.*
1498 *Geophys. Res.*, 100(B7), 12,431–12,447, doi:10.1029/94JB03097, 1995.
1499
1500 Obrebski, M., Allen, R., Pollitz, F.F., and Hung, S.-H., Lithosphere-asthenosphere interaction
1501 beneath the western US from the joint inversion of body-wave travel times and surface-wave
1502 phase velocities, *Geophys. J. Int.*, 185, 1003-1021, 2011.
1503

1504 Özalaybey, S., Savage, M.K., Sheehan, A.F., Louie, J.N. and Brune, J.N., Shear-wave velocity
1505 structure in the northern Basin and Range province from the combined analysis of receiver
1506 functions and surface waves. *Bulletin of the Seismological Society of America*, 87(1), pp.183-
1507 199, 1997.

1508
1509 Parker, E. H., R. B. Hawman, K. M. Fischer, and L. S. Wagner, Crustal evolution across the
1510 southern Appalachians: Initial results from the SESAME broadband array, *Geophys. Res. Lett.*,
1511 **40**, 3853–3857, doi:10.1002/grl.50761, 2013.

1512
1513 Pollitz, F.F. and Snoke, J.A., Rayleigh-wave phase-velocity maps and three-dimensional shear-
1514 velocity structure of the western US from local non-plane surface-wave tomography, *Geophys. J.*
1515 *Int.*, 180, 1153-1169, 2010.

1516
1517 Pollitz, F. F., and W. D. Mooney, Seismic structure of the Central US crust and shallow upper
1518 mantle: Uniqueness of the Reelfoot Rift, *Earth Planet. Sci. Lett.*, **402**, 157–166, 2014.

1519
1520 Porritt, R.W., Allen, R.M., Boyarko, D.C. and Brudzinski, M.R., Investigation of Cascadia
1521 segmentation with ambient noise tomography. *Earth and Planetary Science Letters*, 309(1),
1522 pp.67-76, 2011.

1523
1524 Porritt, R.W., Allen, R.M., and Pollitz, F.F., Seismic imaging east of the Rocky Mountains with
1525 USArray, *Earth and Planetary Science Letters*, doi:10.1016/j.epsl.2013.10.034, 2014.

1526
1527 Porter, R.C., Fouch, M.J., Schmerr, N.C., Dynamic lithosphere within the Great Basin, *Geochem.*
1528 *Geophys. Geosyst.*, 15, 1128–1146, 2014.

1529
1530 Porter, R., Liu, Y. and Holt, W.E., Lithospheric Records of Orogeny within the Continental
1531 US. *Geophysical Research Letters*, 2015.

1532
1533 Prieto, G.A. and Beroza, G.C., Earthquake ground motion prediction using the ambient seismic
1534 field. *Geophysical Research Letters*, 35(14), 2008.

1535
1536 Ritzwoller, M.H., Lin, F.C. and Shen, W., Ambient noise tomography with a large
1537 seismic array. *Comptes Rendus Geoscience*, 343(8), pp.558-570, 2011.

1538 Sabra, K.G., Gerstoft, P., Roux, P., Kuperman, W.A. and Fehler, M.C. Surface wave tomography
1539 from microseisms in Southern California. *Geophysical Research Letters*, 32(14), 2005.

1540
1541 Shapiro, N.M. M. Campillo, L. Stehly, and M.H. Ritzwoller, High resolution surface wave
1542 tomography from ambient seismic noise, *Science*, 307(5715), 1615-1618, 11 March 2005.

1543
1544 Shen, W., M.H. Ritzwoller, and V. Schulte-Pelkum, A 3-D model of the crust and uppermost
1545 mantle beneath the central and western US by joint inversion of receiver functions and surface
1546 wave dispersion, *J. Geophys. Res.*, doi:10.1029/2012JB009602, 118, 1-15, 2013a.

1547

1548 Shen, W., M.H. Ritzwoller, V. Schulte-Pelkum, F.-C. Lin, Joint inversion of surface wave
1549 dispersion and receiver functions: A Bayesian Monte-Carlo approach, *Geophys. J. Int.*, 192, 807-
1550 836, doi:10.1093/gji/ggs050, 2013b.

1551
1552 Shen, W., M.H. Ritzwoller, and V. Schulte-Pelkum, Crustal and uppermost mantle structure in
1553 the central US encompassing the Midcontinent Rift, *J. Geophys. Res.*, 118, 4325-4344,
1554 doi:10.1002/jgrb.50321, 2013c.

1555
1556 Shen, W., M.H. Ritzwoller, D. Kang, Y. Kim, J. Ning, F.-C. Lin, W. Wang, Y. Zheng, and L.
1557 Zhou, A seismic reference model for the crust and uppermost mantle beneath China from surface
1558 wave dispersion, *Geophys. J. Int.*, in press, 2015.

1559
1560 Schmandt, B. and F.-C. Lin, P and S wave tomography of the mantle beneath the United States,
1561 *Geophys. Res. Letts.*, 41(18), 6342-6349, 2014.

1562
1563 Stachnik, J.C., Dueker, K., Schutt, D.L., and Yuan, H., Imaging Yellowstone plume-lithosphere
1564 interactions from inversion of ballistic and diffusive Rayleigh wave dispersion and crustal
1565 thickness data, *Geochemistry Geophysics Geosystems*, 9, Q06004,
1566 doi:10.1029/2008GC001992, 2008.

1567
1568 Tanimoto, T., and L. Rivera (2008), The ZH ratio method for long-period seismic data:
1569 Sensitivity kernels and observational techniques, *Geophys. J. Int.*, **172**(1), 187–198.

1570
1571 Taylor, S.R., Gerstoft, P. and Fehler, M.C., Estimating site amplification factors from ambient
1572 noise. *Geophysical Research Letters*, 36(9), 2009.

1573
1574 Tian, Y., W. Shen, and M.H. Ritzwoller, Crustal and uppermost mantle shear velocity structure
1575 adjacent to the Juan de Fuca Ridge from ambient seismic noise, *Geochem. Geophys. Geosyst.*,
1576 14(8), 3221-3233, doi:10.1002/ggge.20206, 2013.

1577
1578 Thurner, S., R. Margolis, A. Levander, and F. Niu, PdS receiver function evidence for crustal
1579 scale thrusting, relic subduction, and mafic underplating in the Trans-Hudson Orogen and
1580 Yavapai province, *Earth Planet. Sci. Lett.*, **426**, 13–22, 2015.

1581
1582 Tibuleac, I.M. and von Seggern, D., Crust-mantle boundary reflectors in Nevada from ambient
1583 seismic noise autocorrelations. *Geophysical Journal International*, 189(1), pp.493-500, 2012.

1584
1585 Tokam, A.P.K., Tabod, C.T., Nyblade, A.A., Julià, J., Wiens, D.A. and Pasyanos, M.E.,
1586 Structure of the crust beneath Cameroon, West Africa, from the joint inversion of Rayleigh wave
1587 group velocities and receiver functions. *Geophysical Journal International*, 183(2), pp.1061-
1588 1076, 2010.

1589
1590 Wagner, L. S., K. Stewart, and K. Metcalf, Crustal-scale shortening structures beneath the Blue
1591 Ridge Mountains, North Carolina, USA, *Lithosphere*, **4**(3), 242–256, 2012.

1592
1593 Wilson, D. C., R. Aster, S. Grand, J. Ni, and W. S. Baldrige, High-resolution receiver function

1594 imaging reveals Colorado Plateau lithospheric architecture and mantle-supported topography,
1595 *Geophys. Res. Lett.*, **37**, L20313, doi:10.1029/2010GL044799, 2010.

1596

1597 Xie, J., M.H. Ritzwoller, W. Shen, Y. Yang, Y. Zheng, and L. Zhou, Crustal radial anisotropy
1598 across eastern Tibet and the western Yangtze craton, *J. Geophys. Res.*, 118, 4226-4252,
1599 doi:10.1002/jgrb.50296, 2013.

1600

1601 Xie, J., M.H. Ritzwoller, S. Brownlee, and B. Hacker, Inferring the oriented elastic tensor from
1602 surface wave observations: Preliminary application across the Western US, *Geophys. J. Int.*, 201,
1603 996-1021, 2015.

1604

1605 Yang, Y., Application of teleseismic long-period surface waves from ambient noise in regional
1606 surface wave tomography: a case study in western USA. *Geophysical Journal
1607 International*, 198(3), pp.1644-1652, 2014.

1608

1609 Yang, Y., M.H. Ritzwoller, F.-C. Lin, M.P. Moschetti, and N.M. Shapiro, The structure of the
1610 crust and uppermost mantle beneath the western US revealed by ambient noise and earthquake
1611 tomography, *J. Geophys. Res.*, 113, B12310, 2008.

1612

1613 Yang, Y., M.H. Ritzwoller, and C.H. Jones, Crustal structure determined from ambient noise
1614 tomography near the magmatic centers of the Coso region, southeastern California, *Geochem.
1615 Geophys. Geosyst.*, 12, Q02009, doi:10.1029/2010GC003362, 2011.

1616

1617 Yao, H., van Der Hilst, R. D., & Maarten, V, Surface-wave array tomography in SE Tibet
1618 from ambient seismic noise and two-station analysis—I. Phase velocity maps. *Geophysical
1619 Journal International*, 166(2), 732-744, 2006.

1620

1621 Yeck, W. L., A. F. Sheehan, M. L. Anderson, E. A. Erslev, K. C. Miller, and C. S. Siddoway
1622 (2014), Structure of the Bighorn Mountain region, Wyoming, from teleseismic receiver function
1623 analysis: Implications for the kinematics of Laramide shortening, *J. Geophys. Res. Solid Earth*,
1624 **119**, 7028–7042, doi:10.1002/2013JB010769.

1625

1626 Zigone, D., Ben-Zion, Y., Campillo, M. and Roux, P., Seismic tomography of the Southern
1627 California plate boundary region from noise-based Rayleigh and Love waves. *Pure and Applied
1628 Geophysics*, 172(5), pp.1007-1032, 2015.

1629

1630 Zhou, L., J. Xie, W. Shen, Y. Zheng, Y. Yang. H. Shi, and M.H. Ritzwoller, The structure of the
1631 crust and uppermost mantle beneath South China from ambient noise and earthquake
1632 tomography, *Geophys. J. Int.*, doi: 10.1111/j.1365-246X.2012.05423.x, 2012.

1633

1634 Zhu, L. and Kanamori, H., Moho depth variation in southern California from teleseismic receiver
1635 functions. *Journal of Geophysical Research B*, 105(B2), pp.2969-2980, 2000.

1636

1637

1638

Figure 1

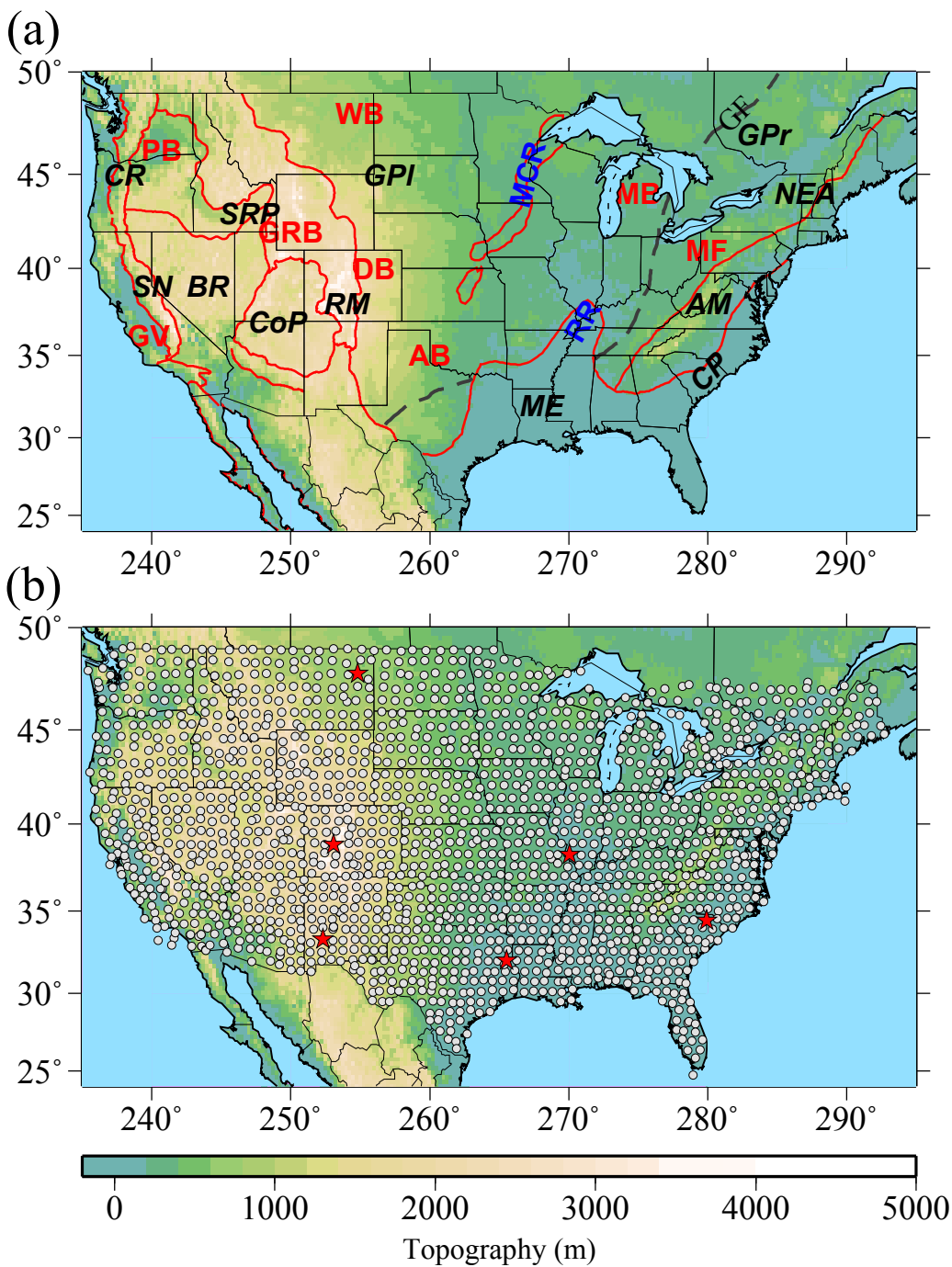


Figure 2

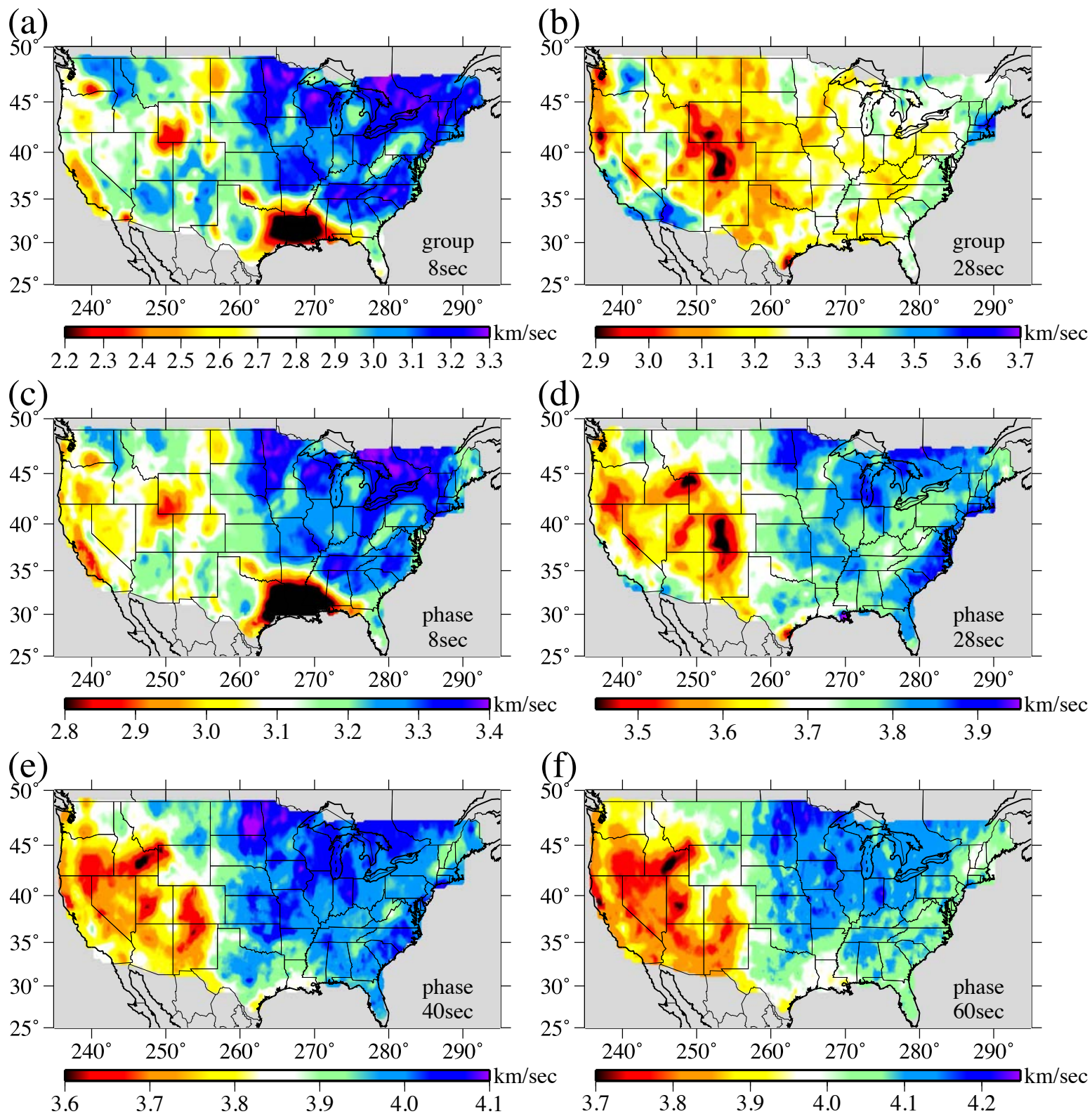
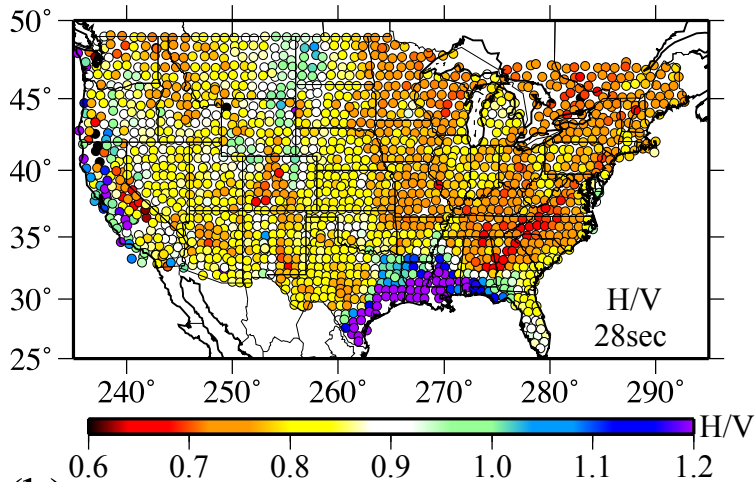


Figure 3

(a)



(b)

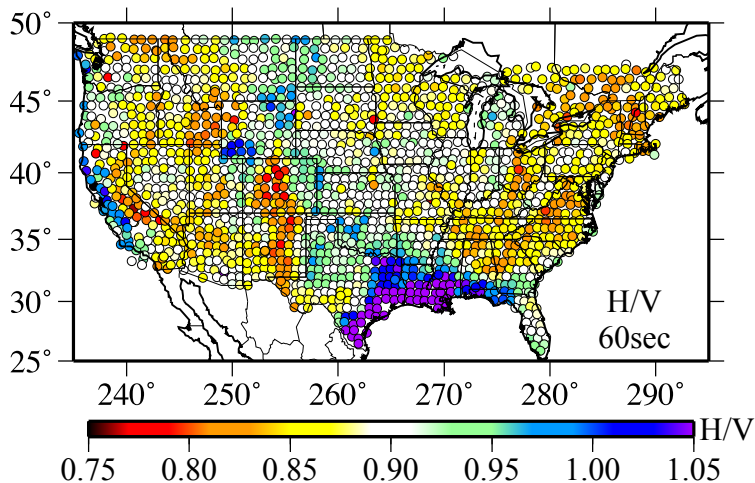


Figure 4

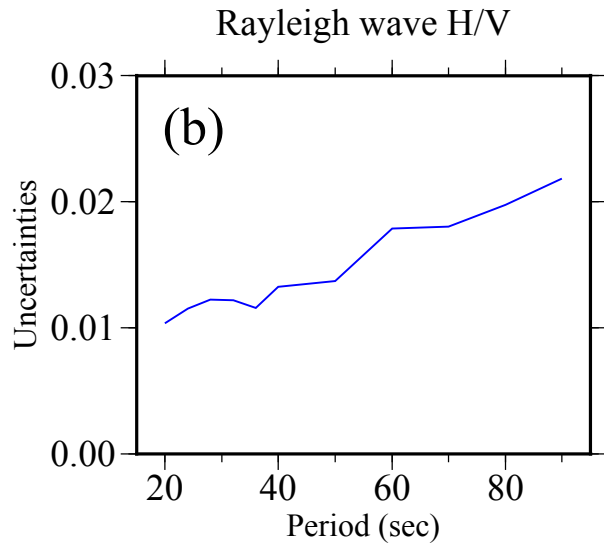
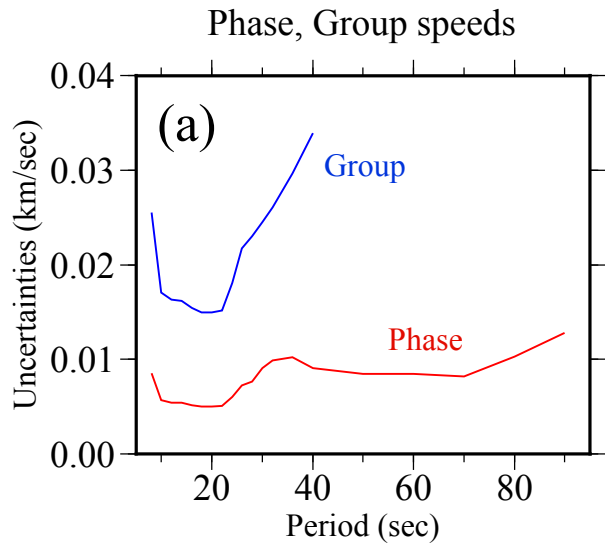


Figure 5

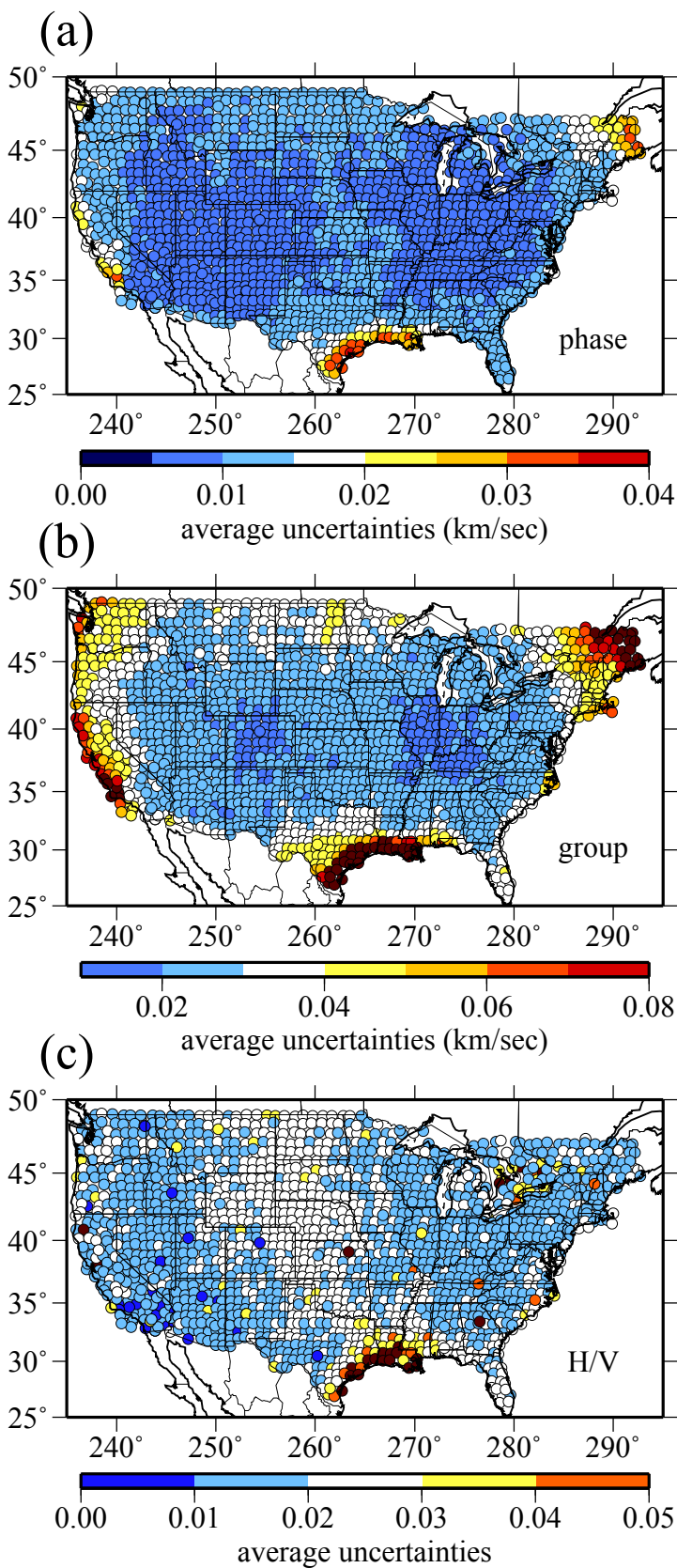


Figure 6

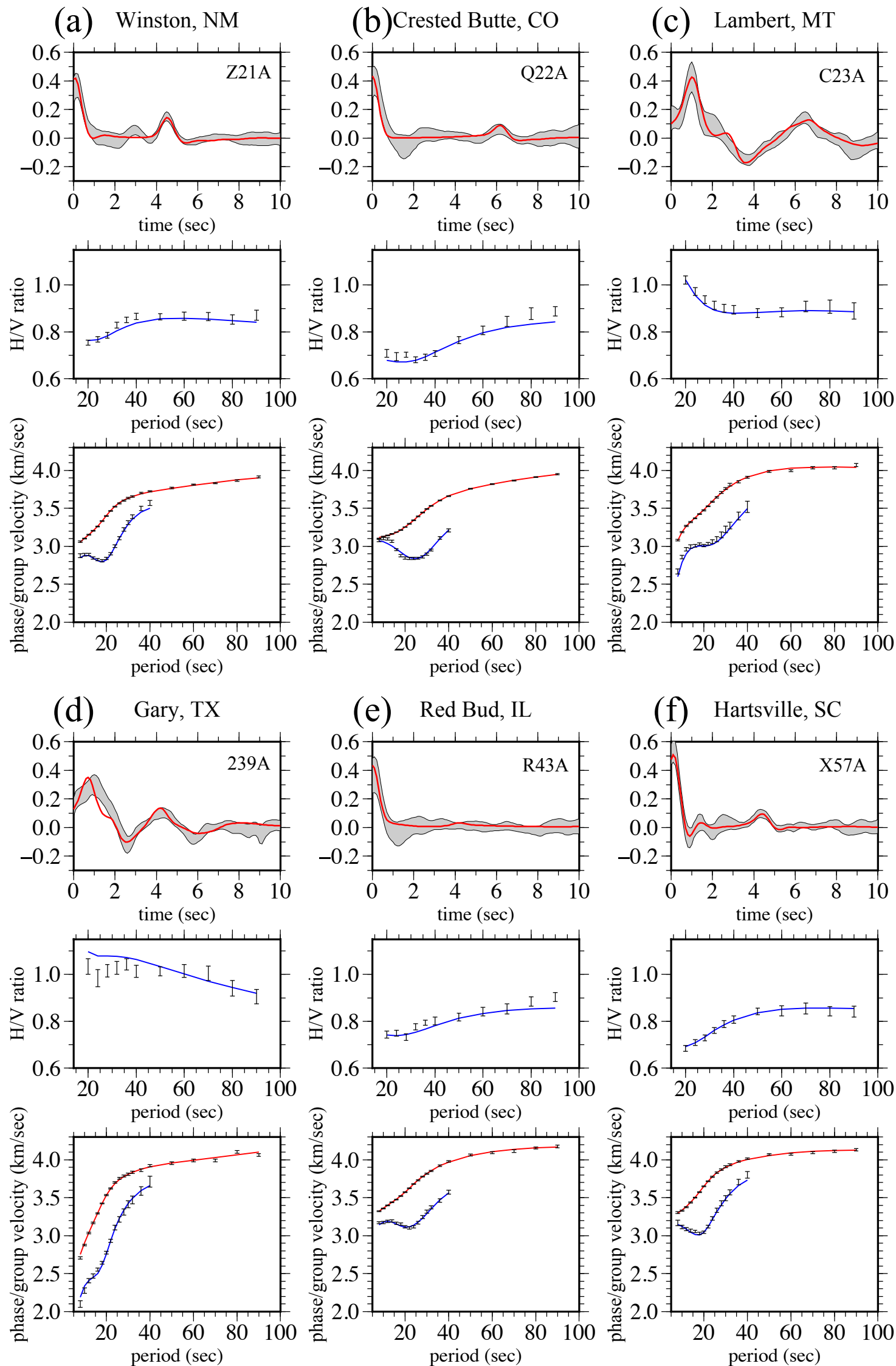


Figure 7

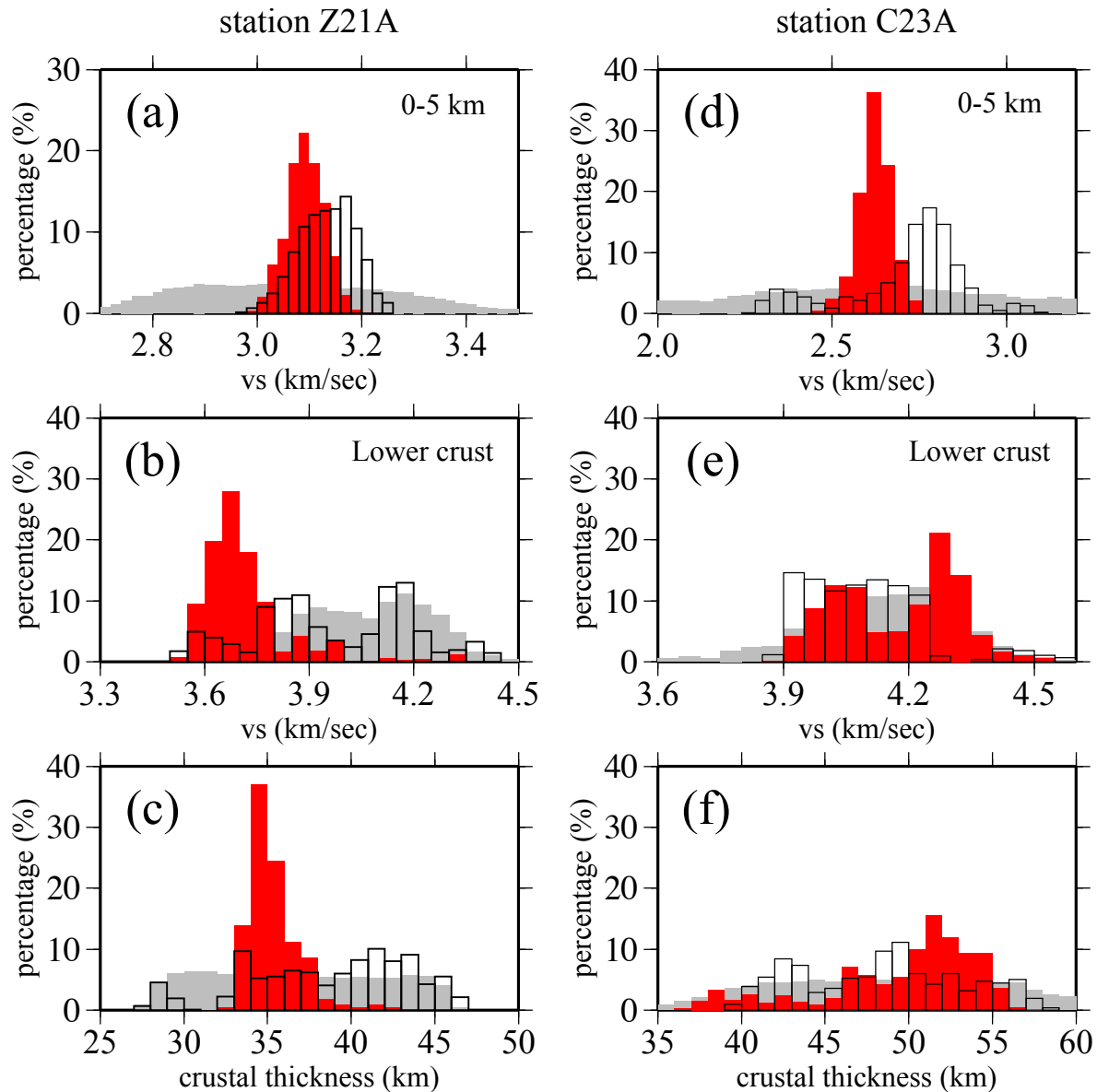


Figure 8

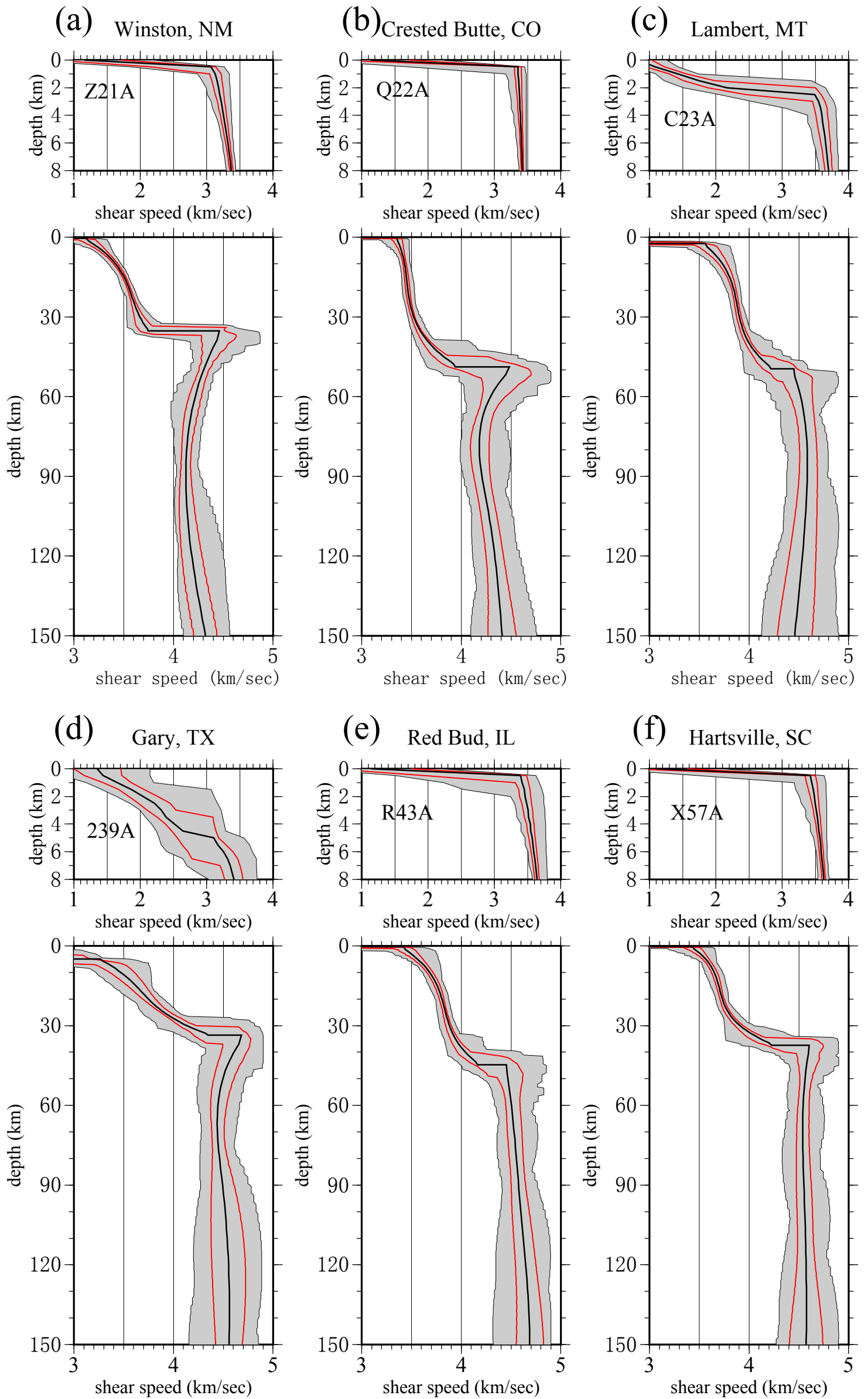


Figure 9

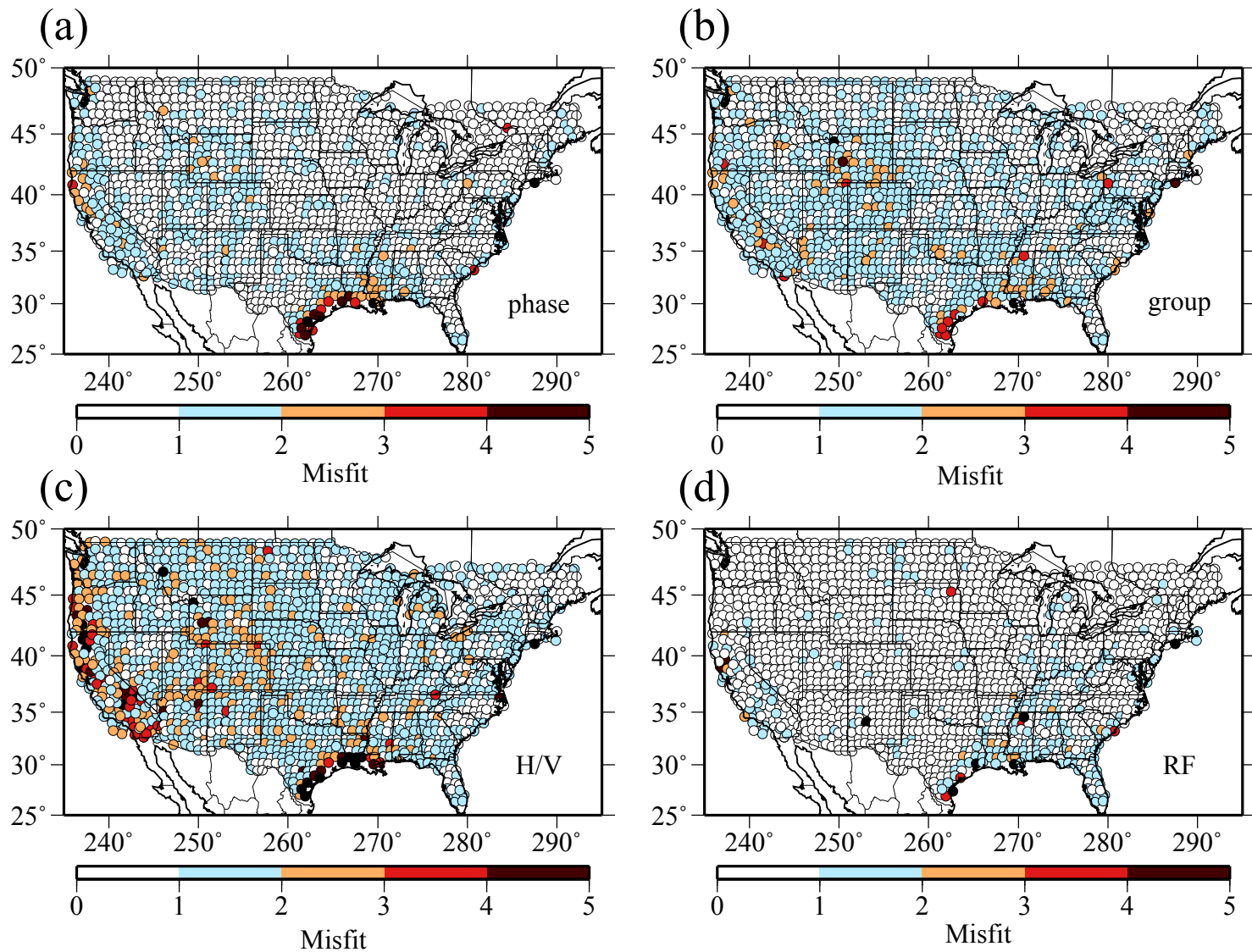
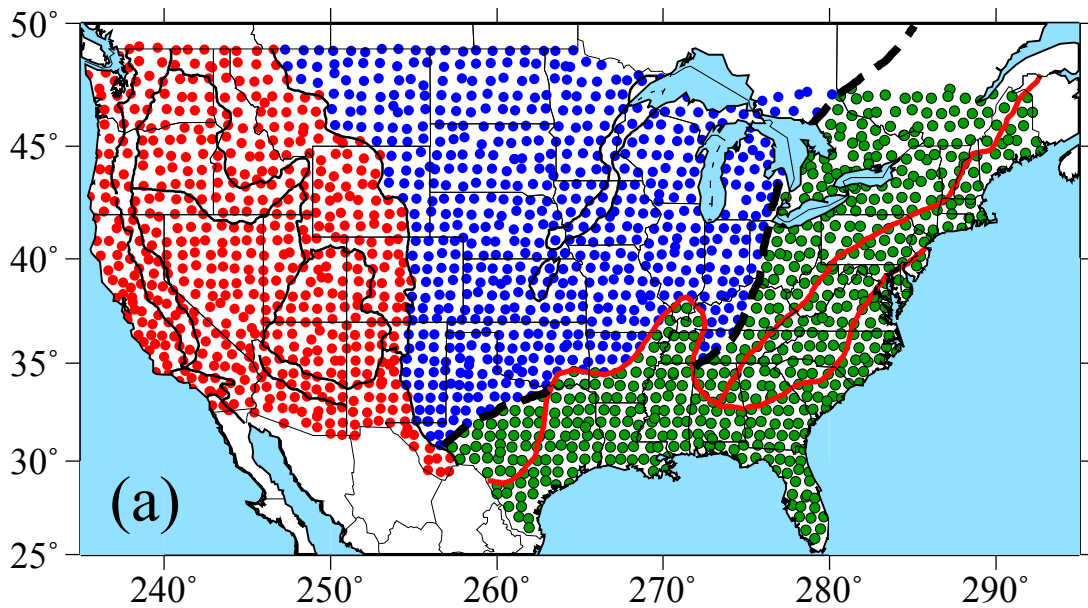
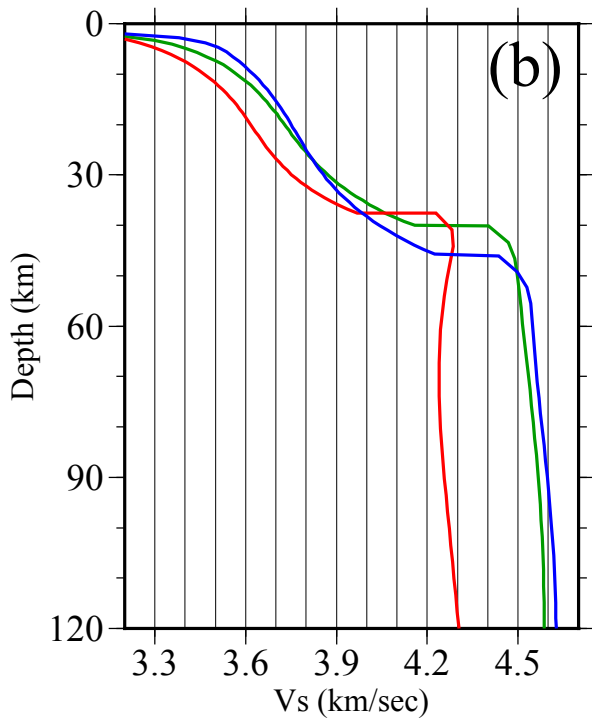


Figure 10



Average models



Variations within each region

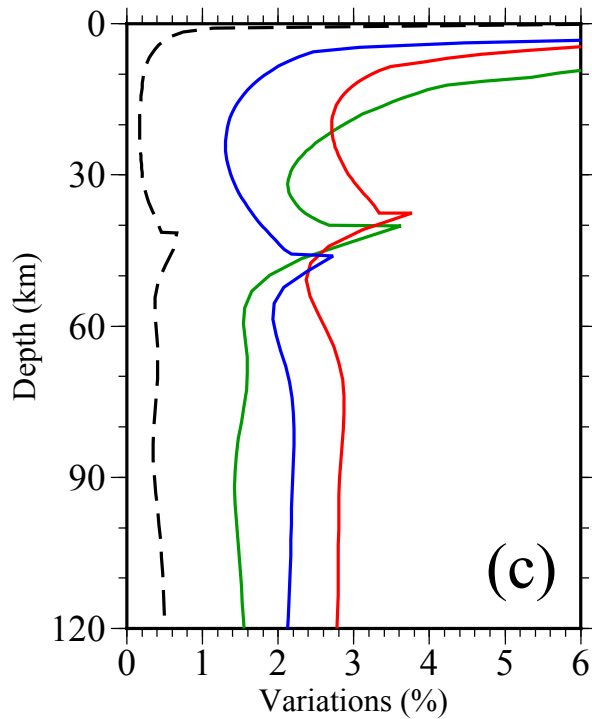


Figure 11

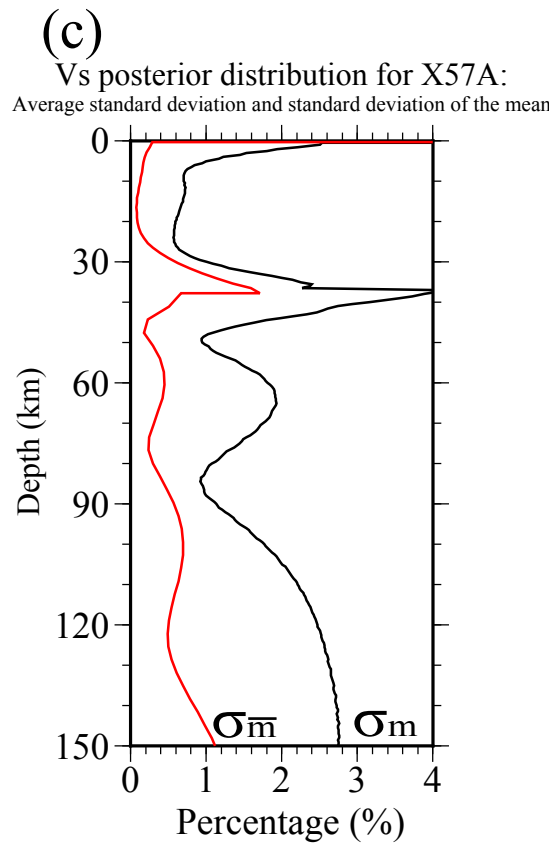
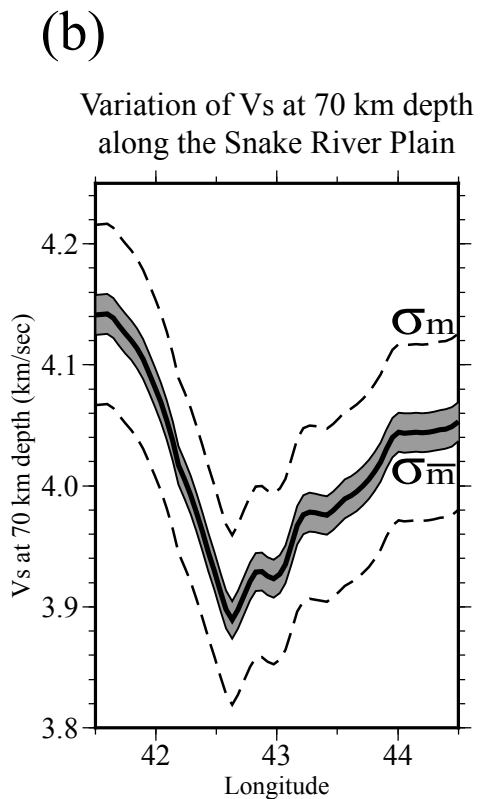
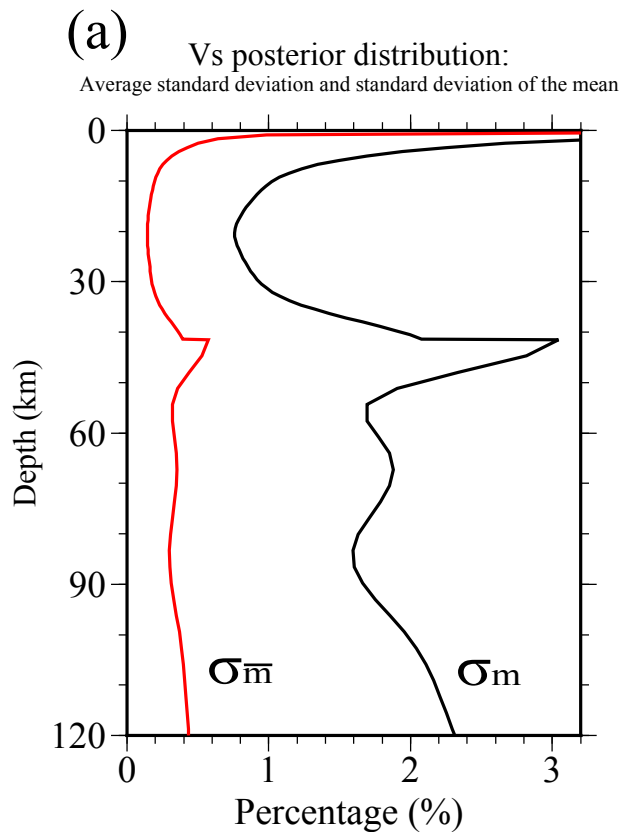


Figure 12

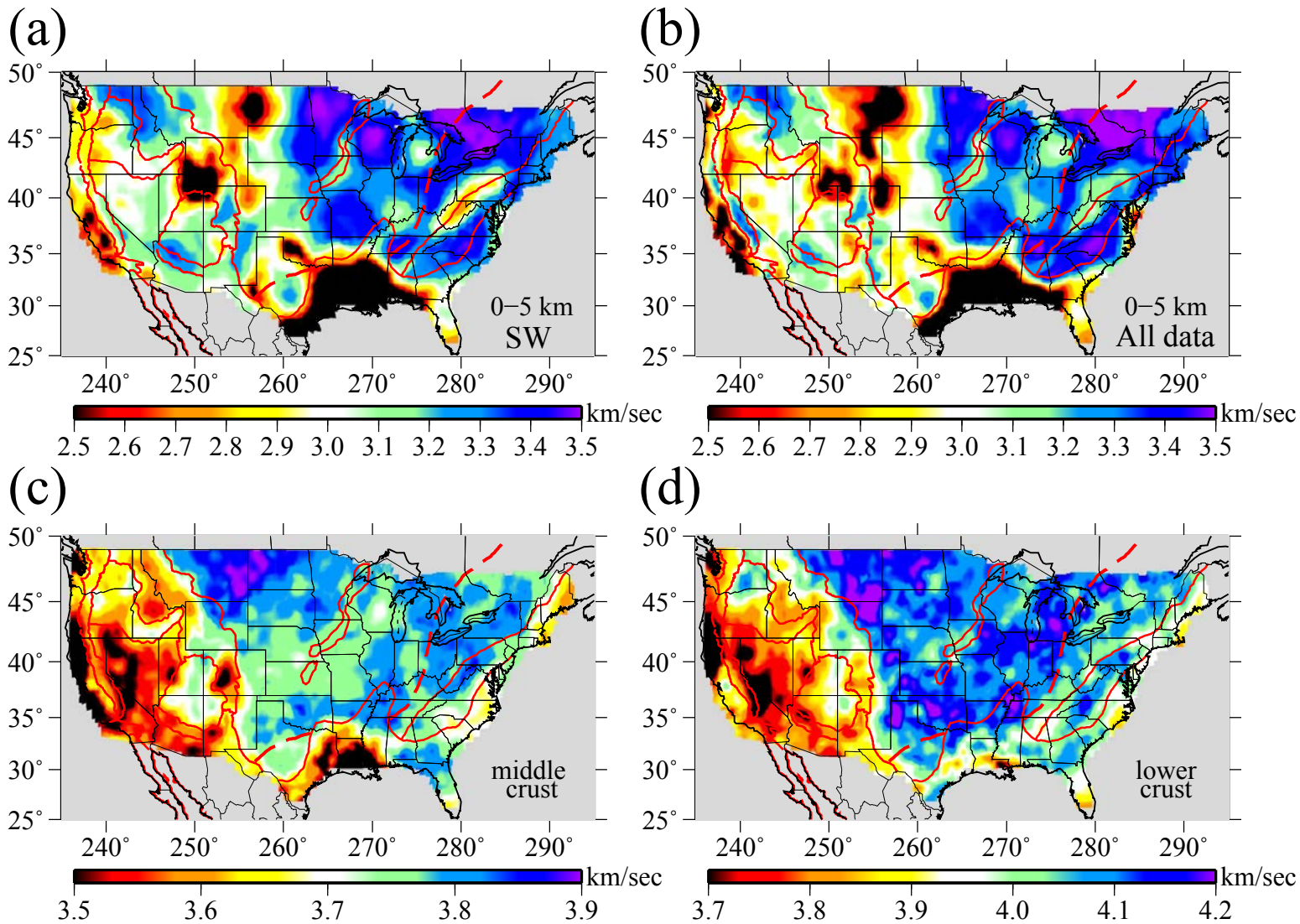
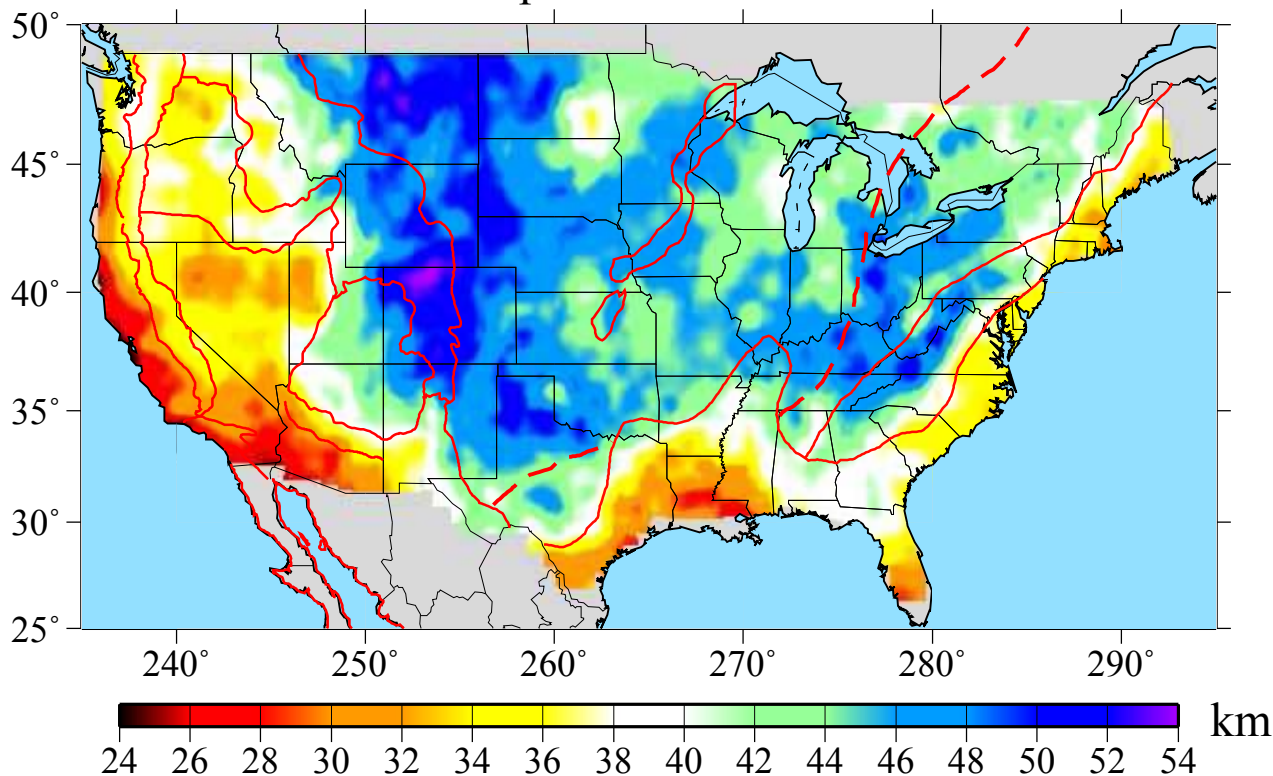


Figure 13

Crustal thickness

(a)

Mean of posterior distribution



(b)

Standard deviation of posterior distribution

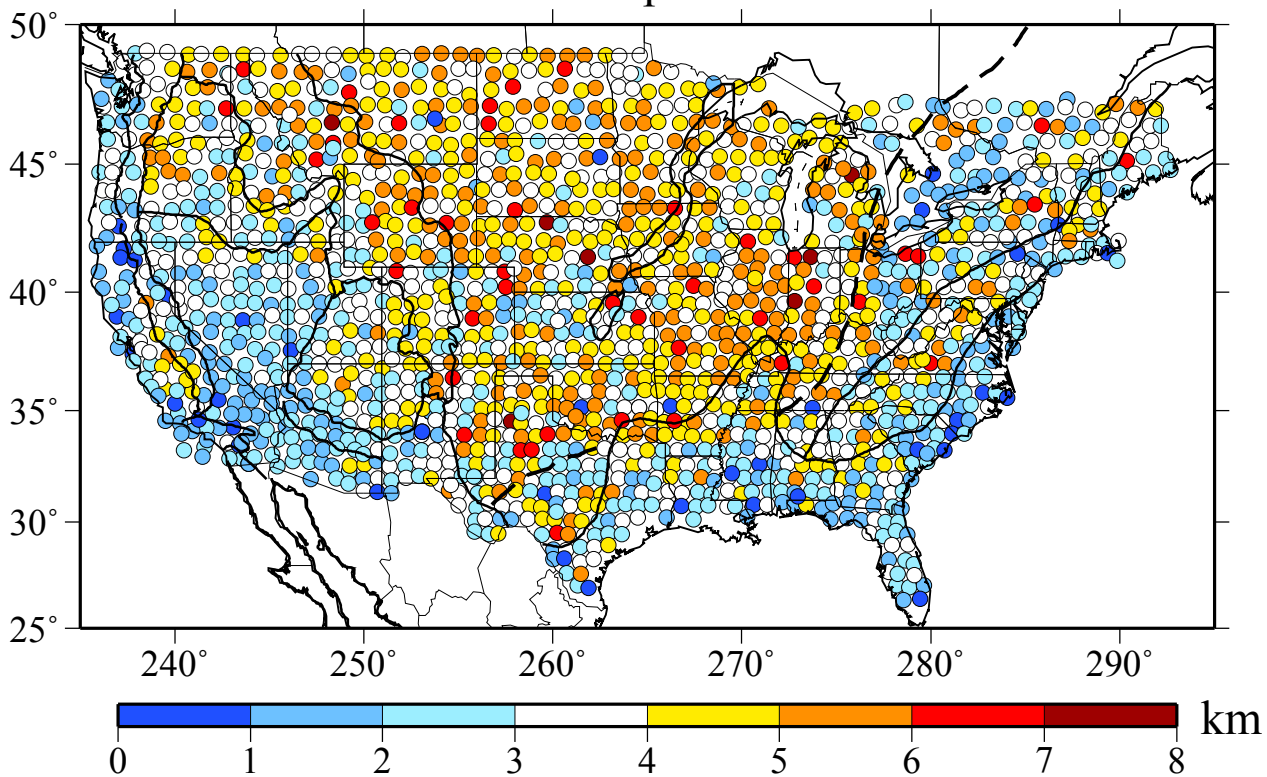
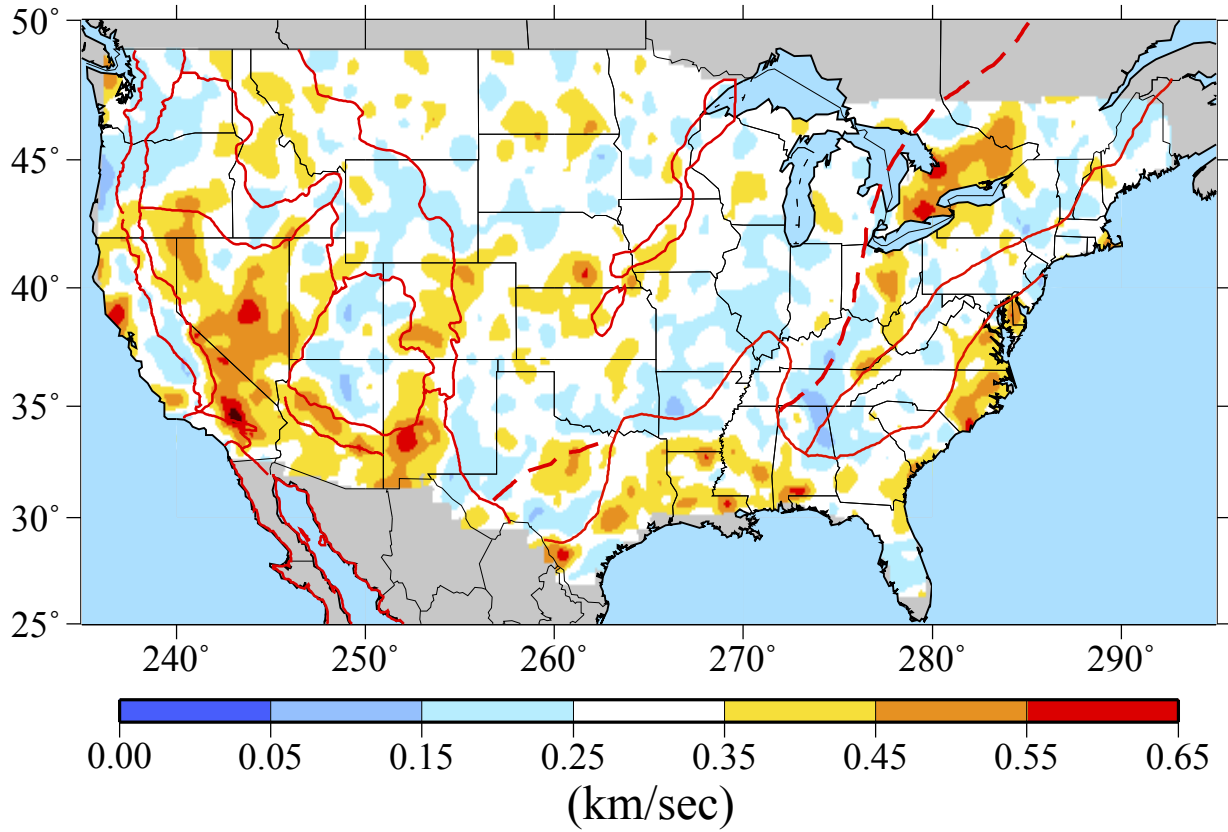


Figure 14

Vs jump across Moho
(a) Mean of posterior distribution



(b) Standard deviation of posterior distribution

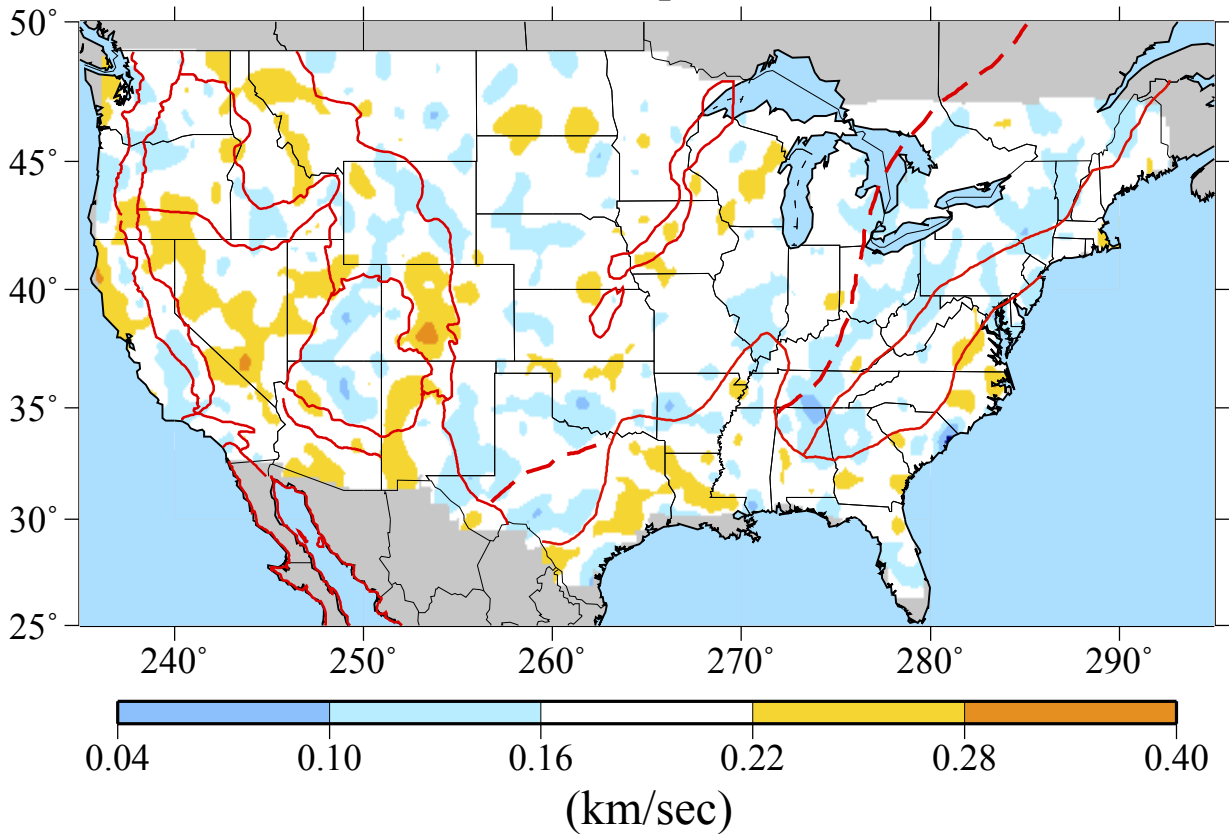


Figure 15

Standard deviation of the posterior distribution

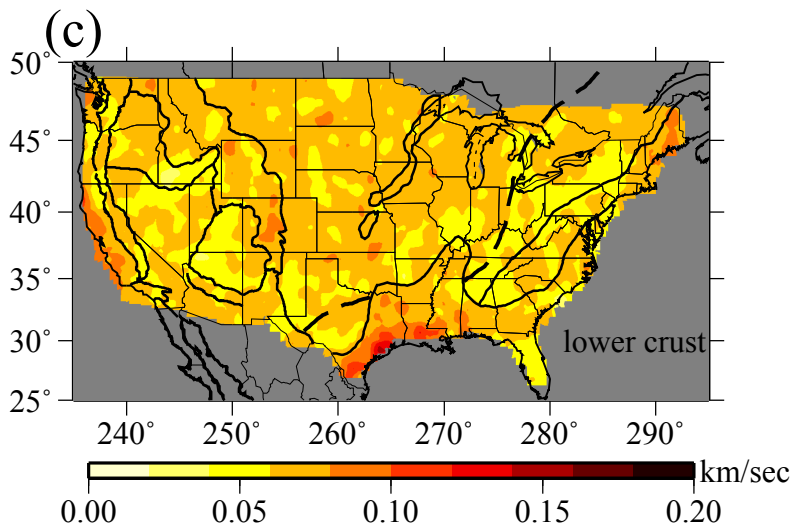
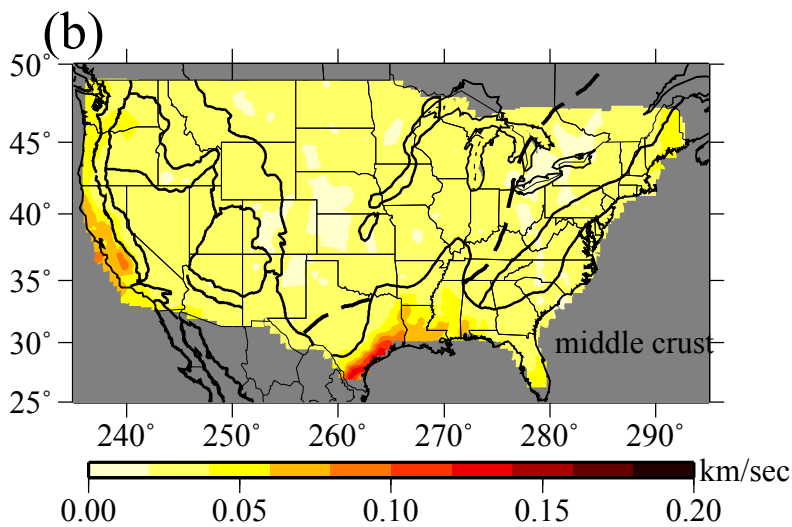
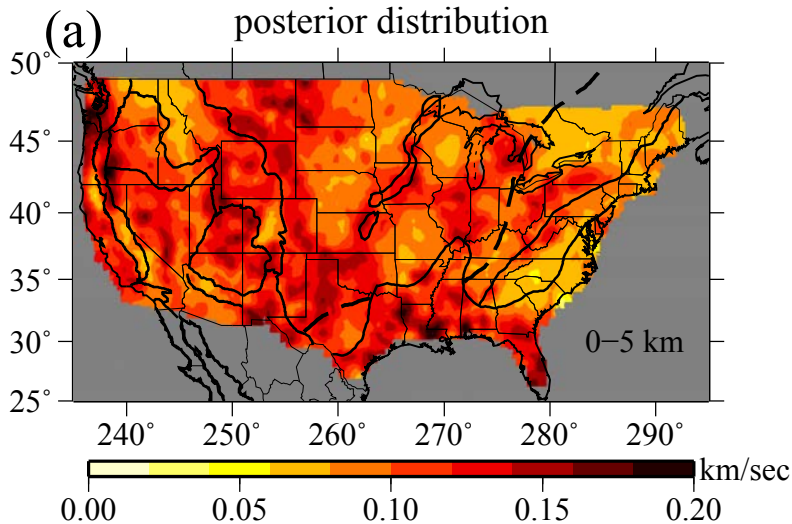


Figure 16

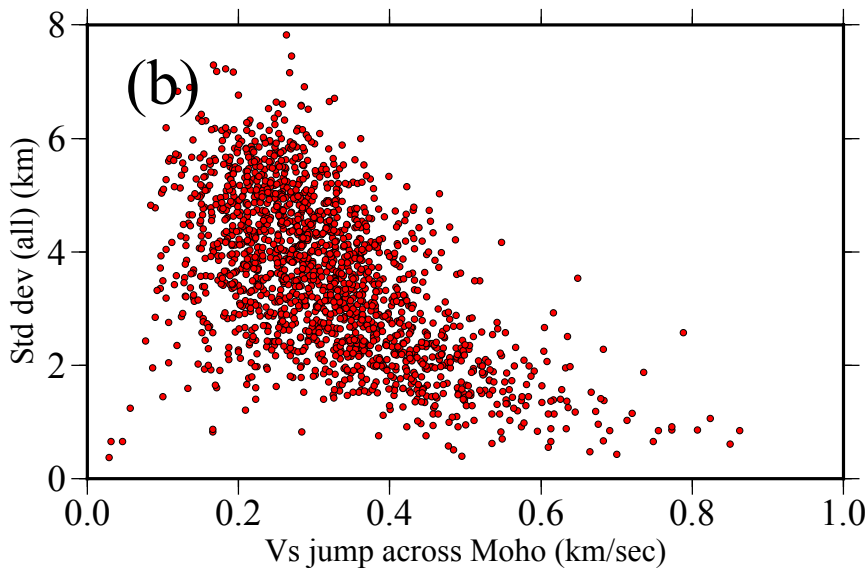
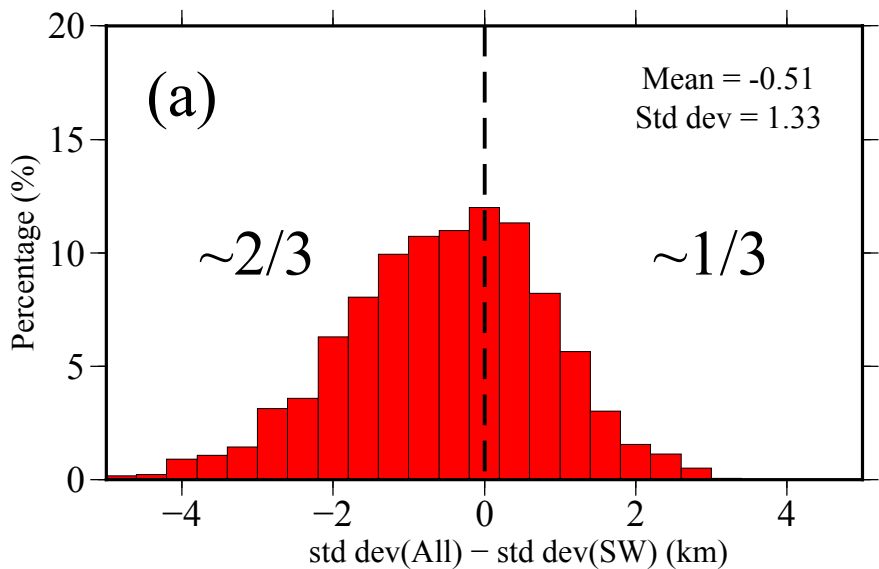


Figure 17

Slope of V_s in the uppermost mantle

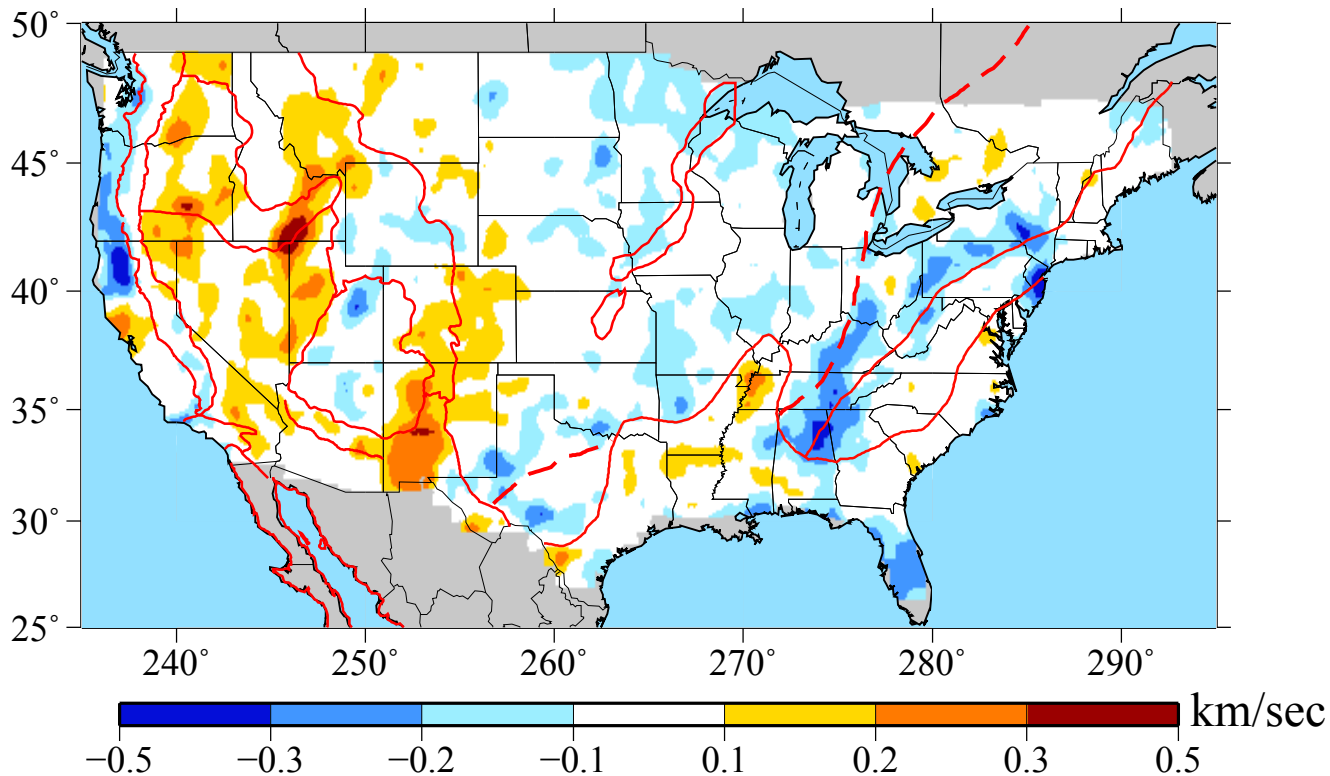


Figure 18

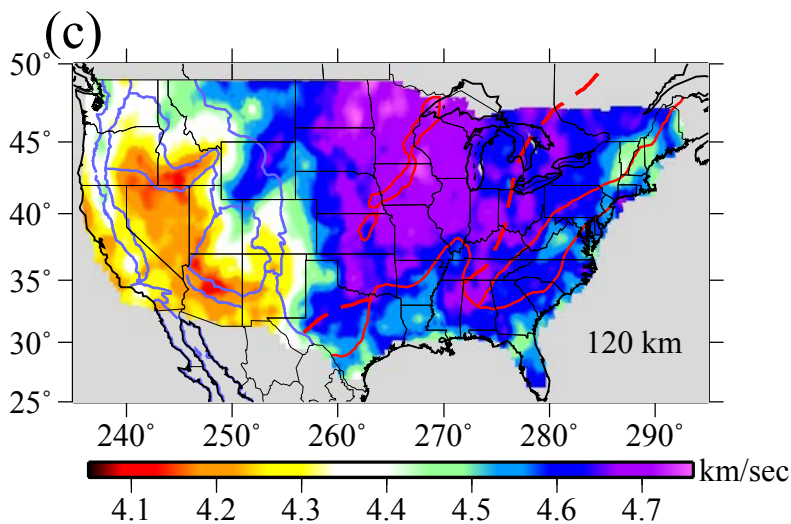
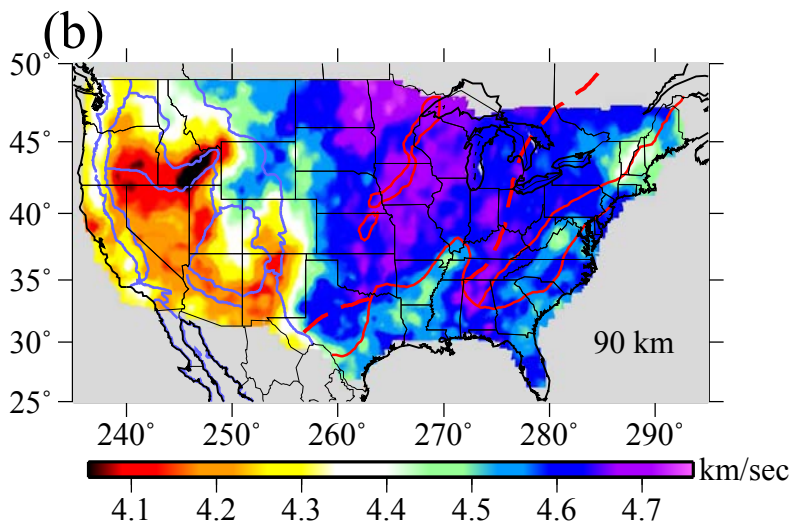
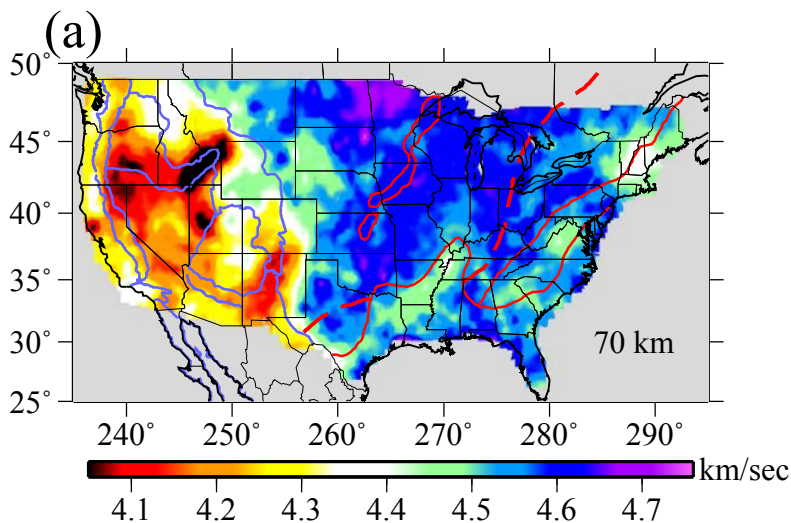


Figure 19

Standard deviation of the posterior distribution

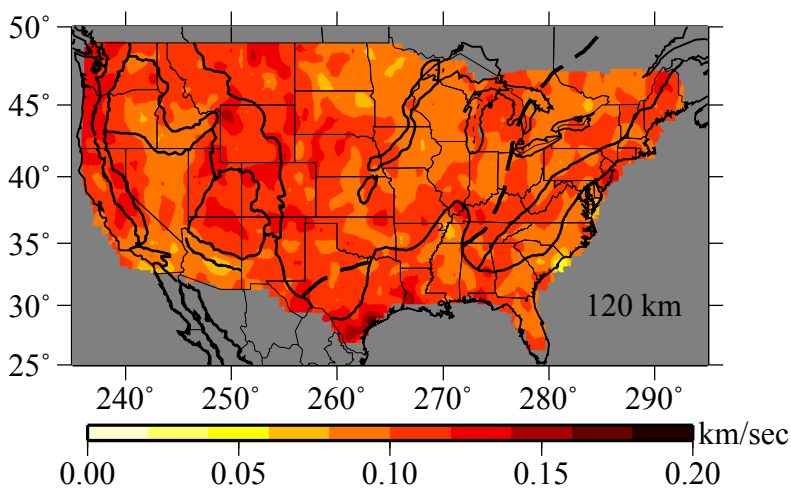
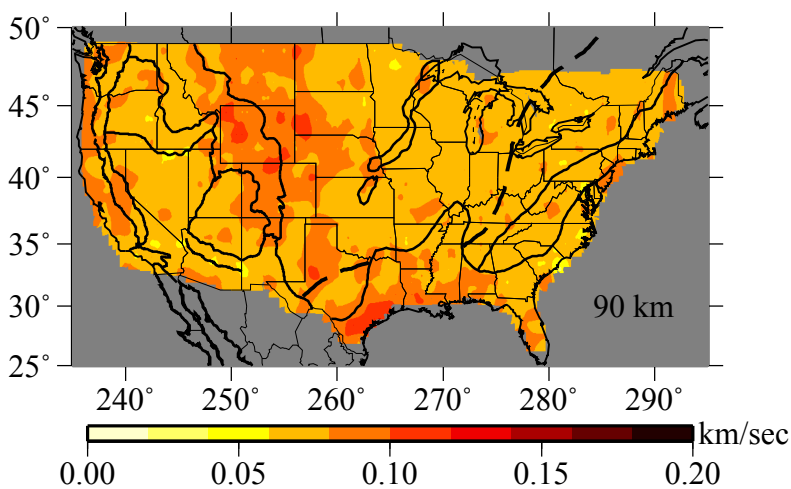
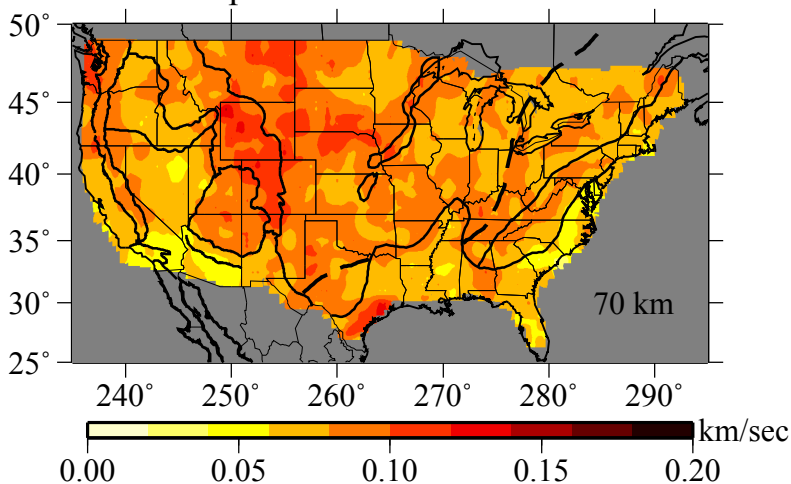


Figure 20

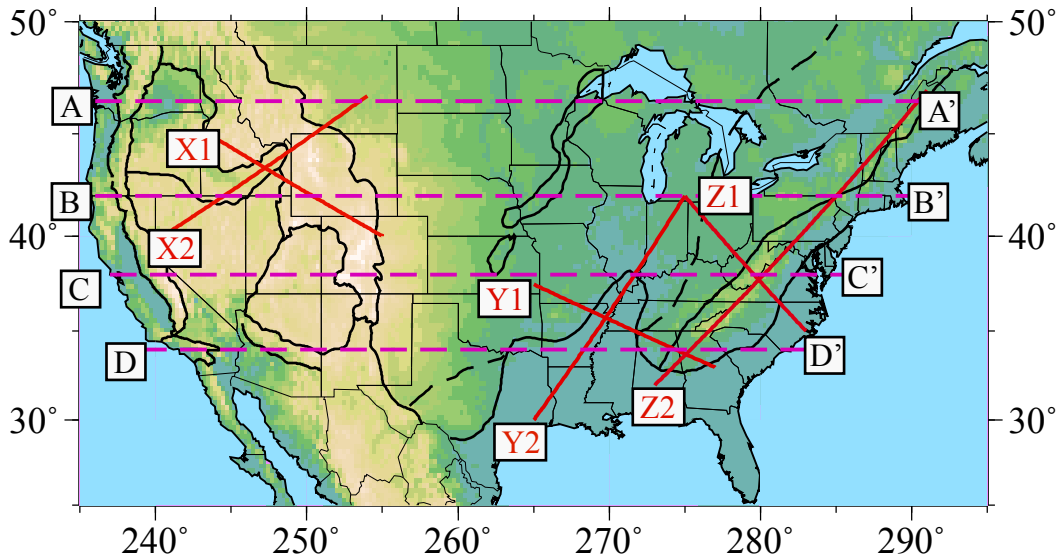


Figure 21

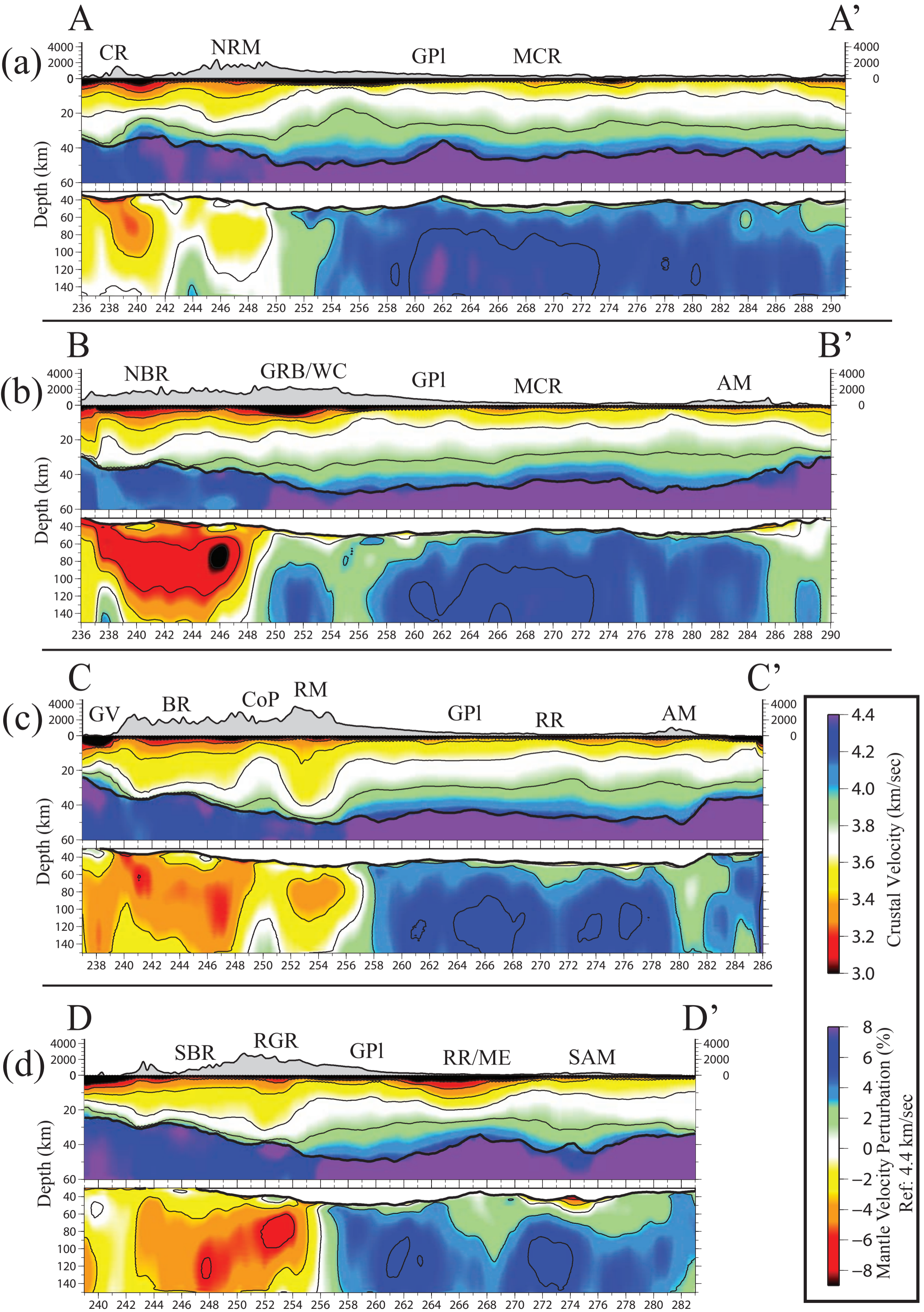


Fig. 22

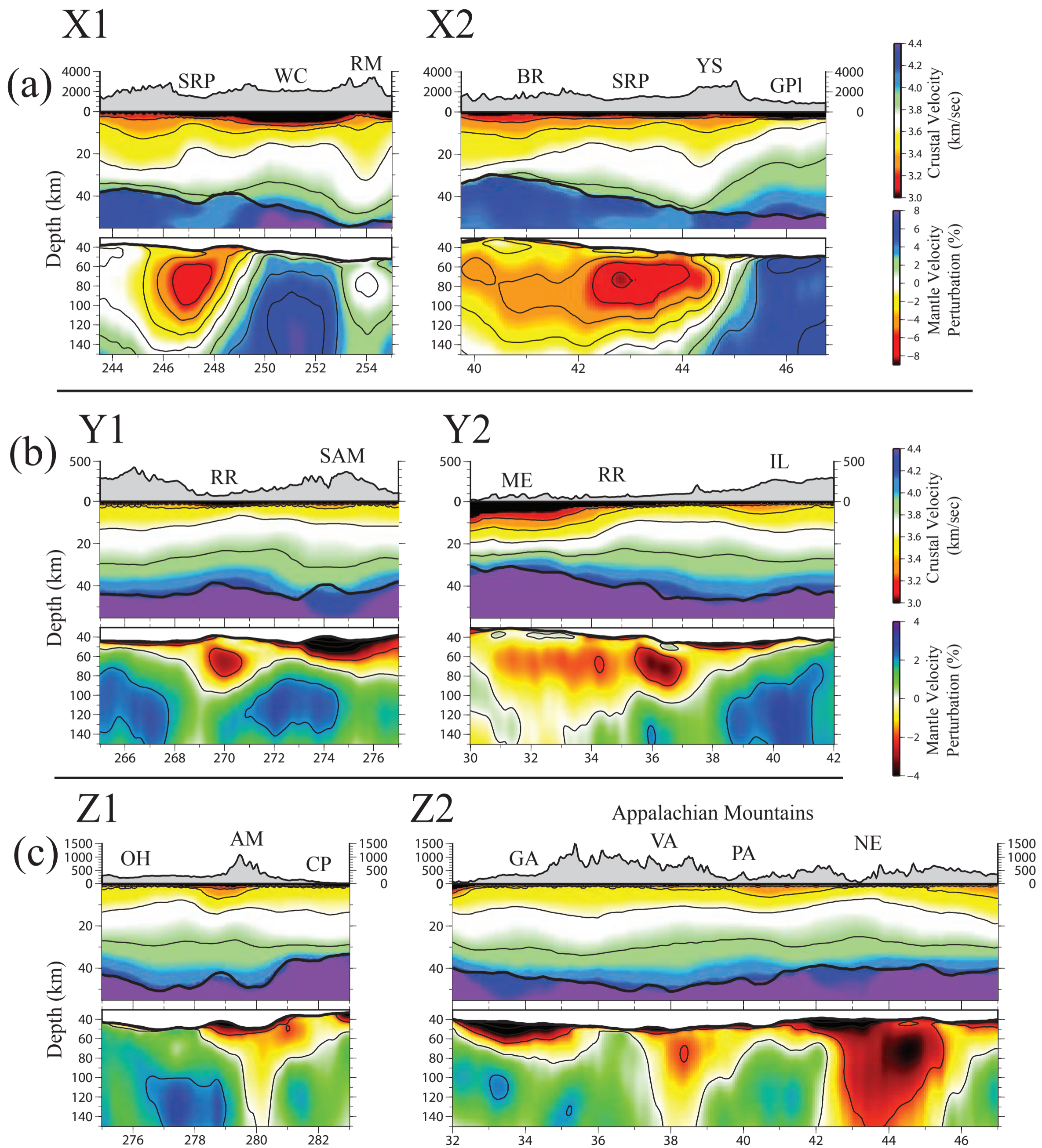


Figure 23

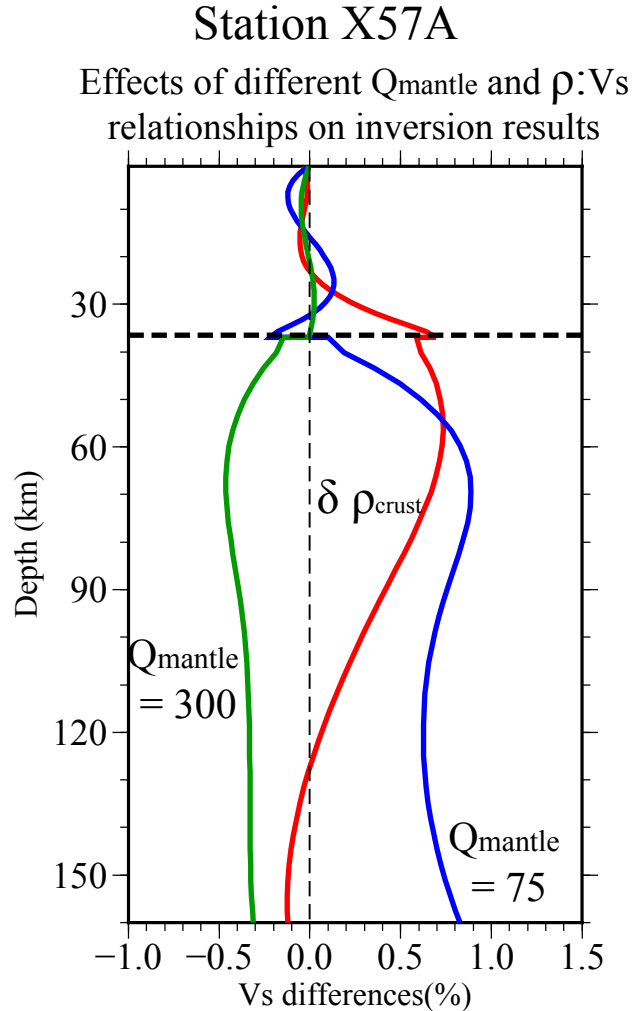
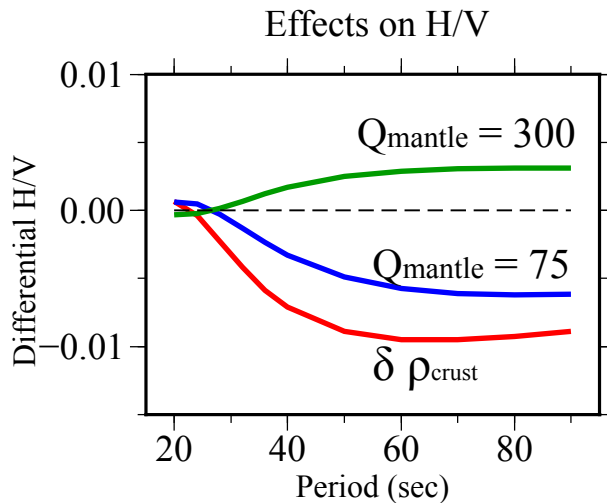
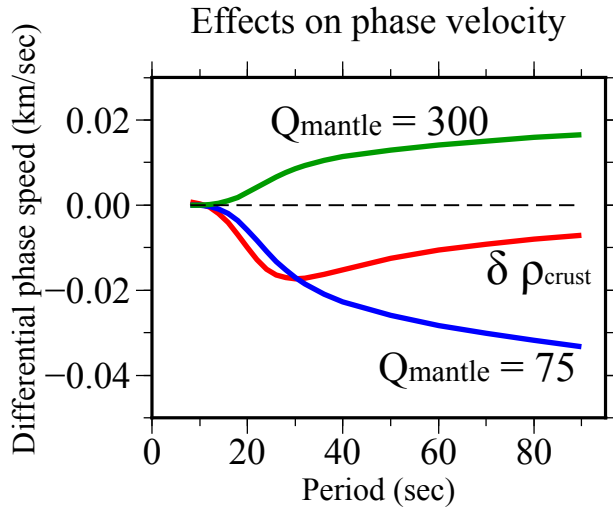


Figure 24

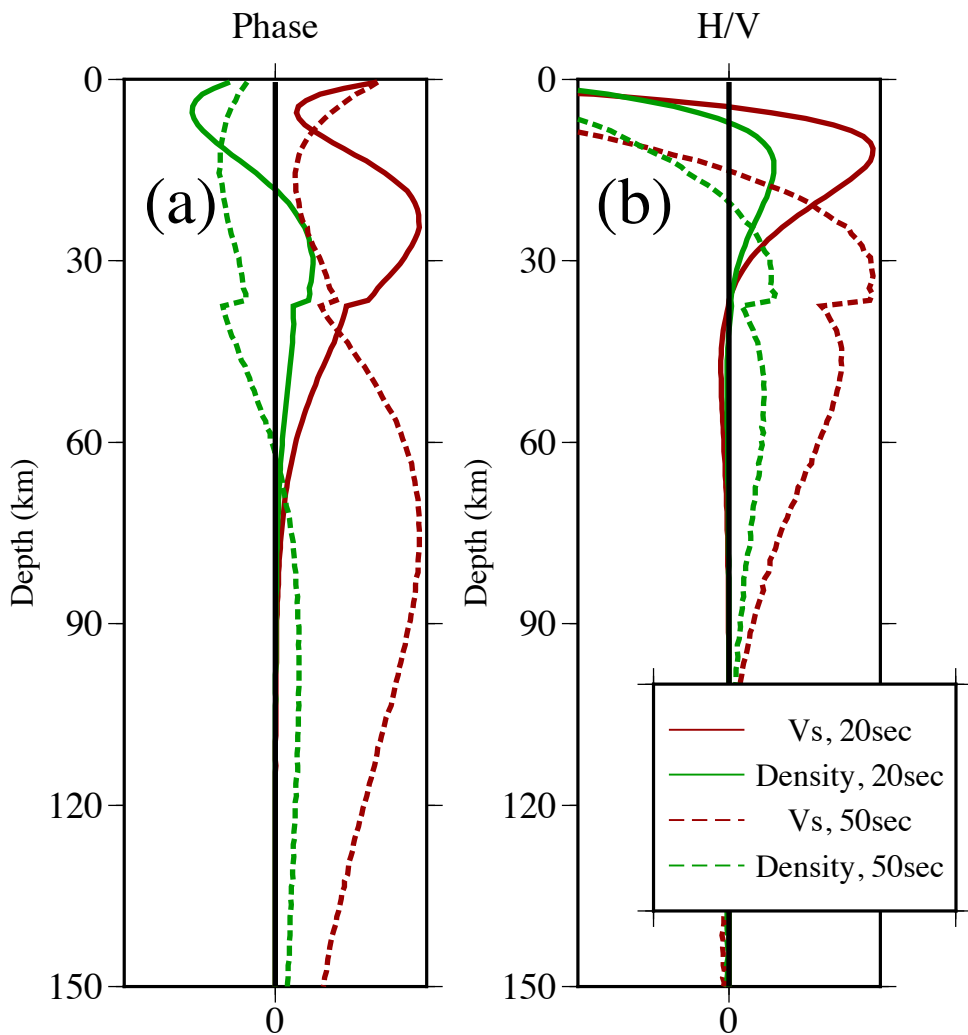


Table 1. Abbreviations of tectonic features and geographic names marked in **Figs. 1, 21, and 22.**

| | | |
|---------------------------|-------------|---------------------------|
| Sedimentary Basins | AB | Anadarko Basin |
| | DB | Denver Basin |
| | GRB | Green River Basin |
| | GV | Great Valley |
| | MB | Michigan Basin |
| | MF | Marcellus Formation |
| | PB | Pasco Basin |
| | WB | Williston Basin |
| Tectonic Features | AB | Anadarko Basin |
| | AM | Appalachian Mountains |
| | BR | Basin and Range |
| | CoP | Colorado Plateau |
| | CP | Coastal Plains |
| | CR | Cascade Range |
| | GPI | Great Plains |
| | GPr | Greenville Province |
| | MCR | Mid-Continent Rift |
| | ME | Mississippi Embayment |
| | NEA | Northeastern Appalachians |
| | RGR | Rio Grande Rift |
| | RM | Rocky Mountains |
| | RR | Reelfoot Rift |
| | SN | Sierra Nevada |
| | SRP | Snake River Plain |
| | WC | Wyoming Craton |
| YS | Yellowstone | |
| Geographic Names | GA | Georgia |
| | IL | Illinois |
| | NE | New England |
| | OH | Oklahoma |
| | PA | Pennsylvania |
| | VA | Virginia |

Table 2. Stations with amplitude errors.

| Type of Amplitude Errors | Stations |
|---|--|
| Half amplitude error (Differential Output) | MSO, J17A, N02C, S43A, T41A, 634A, I50A |
| Other amplitude errors | VES, VMZ, SCZ2 |

Table 3. Range of perturbations to model variables.

| Model Variable | Range of perturbation |
|---|------------------------------|
| Thickness, sedimentary layer | ±100% |
| Thickness, crystalline crust | ±20% |
| V _{sv} , top of sedimentary layer | ±1 km/sec |
| V _{sv} , bottom of sedimentary layer | ±1 km/sec |
| B-spline coefficients, crust | ±20% |
| B-spline coefficients, mantle | ±20% |